Grain boundary networks in RABiTS based YBa$_2$Cu$_3$O$_{7-\delta}$ coated conductors

Dissertation

zur Erlangung des akademischen Grades
Doktor rerum naturalium
(Dr. rer. nat)

vorgelegt
der Fakultät Mathematik und Naturwissenschaften
der Technischen Universität Dresden

von

Dipl.Phys. **Laura Isabel Fernández Gómez-Recuero**

geboren am 12. 11. 1973 in Toledo (Spanien)

Gutachter: . . . .
                      . . . .
                      . . . .
Eingereicht am: . . . .
Tag der Verteidigung: . . . .

Kurzfassung

In der vorliegenden Dissertation werden Transporteigenschaften und die Limitierung der kritischen Stromdichte von $YBa_2Cu_3O_{7-\delta}$ Bandleitern untersucht. Für die Präparation wird das epitaktische Schichtwachstum auf biaxial texturierten Substraten genutzt (RABiTS-Technik). Dabei wird mittels gepulster Laserdeposition eine Pufferschicht aus CeO_2 und Yttrium-stabilisiertem Zirkonoxyd (YSZ) und anschließend eine $YBa_2Cu_3O_{7-\delta}$ Schicht epitaktisch auf ein Substrat aufgebracht. Die resultierende biaxiale Textur der $YBa_2Cu_3O_{7-\delta}$-Schicht spielt eine Hauptrolle, um möglichst hohe Stromdichten zu erreichen. Es zeigte sich, daß die granulare Struktur des Substrates in die $YBa_2Cu_3O_{7-\delta}$-Schicht übertragen wird und zur Ausbildung eines Korngrenzennetzwerkes führt, welches wiederum die zu erwartende kritische Stromdichte begrenzt. Um die Wirkung des Korngrenzennetzwerkes zu untersuchen, wurden kritische Ströme der gewachsenen Schichten in Abhängigkeit der Temperatur und des angelegten Magnetfeldes gemessen. Es stellte sich heraus, daß die Limitierung des Stroms bei schwachen Magnetfeldern zwischen den einzelnen Körnern bestimmend ist, die dann bei größeren Feldern einer Strombegrenzung innerhalb der Körner weicht. Das beide Bereiche trennende Magnetfeld wird als Übergangsfeld bezeichnet. Daraus kann geschlußfolgert werden, daß das Korngrenzennetzwerk von $YBa_2Cu_3O_{7-\delta}$ Bandleitern den Strom nur für magnetische Felder unterhalb des Übergangsfeldes begrenzt.

Abstract

This thesis deals with the transport properties and critical current limitations found in $YBa_2Cu_3O_{7-\delta}$ coated conductors prepared by the "rolling assisted biaxially textured substrate" (RABiTS) approach. For this purpose a buffer layer system composed of CeO_2 and yttria-stabilised zirconia, and subsequently a $YBa_2Cu_3O_{7-\delta}$ film were epitaxially grown by pulsed laser deposition on a biaxially textured metallic substrate. The resulting texture of the $YBa_2Cu_3O_{7-\delta}$ film is crucial for the achievement of high critical current densities. A propagation of the granular structure of the metallic substrate into the $YBa_2Cu_3O_{7-\delta}$ film was detected, which leads to the formation of a $YBa_2Cu_3O_{7-\delta}$ grain boundary network and limits the critical current density of the samples. In order to study this limitation, critical current measurements were performed on the prepared samples at different temperatures and magnetic fields, detecting a transition between intergrain and intragrain current limitation that occurs at the so-called crossover magnetic field. The crossover magnetic field was found to shift to lower values as the temperature was increased. It was concluded that the grain boundary network limits the critical current density of the $YBa_2Cu_3O_{7-\delta}$ coated conductor only for magnetic fields below the crossover field.

Contents

Chapter 1

Introduction

From the discovery of superconductivity in 1911 by Heike Kamerlingh Onnes up to the present, many advances have been made in this field in both theoretical description and practical application, making superconductivity one of the most heavily investigated branches of physics. The discovery of high temperature superconductors with T_c values well above the boiling point of liquid nitrogen (77 K) opened up the way to a broader range of applications with the possibility to replace liquid helium as cooling medium with liquid nitrogen that is more economical. $YBa_2Cu_3O_{7-\delta}$ is the most promising material of the high temperature superconductor family despite its relatively "low" critical temperature T_c = 93 K in comparison to $HgBa_2Ca_2Cu_3O_9$ with T_c = 134 K. The most remarkable properties of $YBa_2Cu_3O_{7-\delta}$ are high pinning energy and irreversibility field as a result of its reduced anisotropy, yielding higher critical current densities in magnetic fields at 77 K than other high temperature superconductors.

Current challenges are the development and production of long $YBa_2Cu_3O_{7-\delta}$ tapes known as coated conductors, with high critical current density values J_c exceeding 1 MA/cm^2 (at 77 K and self-field), and their implementation in power devices. A $YBa_2Cu_3O_{7-\delta}$ coated conductor consists of a long metallic substrate coated by a buffer layer architecture and a biaxially textured $YBa_2Cu_3O_{7-\delta}$ film on top. One crucial requirement for the preparation of $YBa_2Cu_3O_{7-\delta}$ coated conductors with high critical current densities is the elimination of weak links between the $YBa_2Cu_3O_{7-\delta}$ grains. Weak links in the high temperature superconductors are produced by grain boundaries that lead to a weak coupling between the superconducting grains and consequently to a reduction in the critical current density. One way to avoid the formation of weak links is to induce a biaxial texture in the $YBa_2Cu_3O_{7-\delta}$ film. For this, both the c axis and the $a(b)$ axis of all the $YBa_2Cu_3O_{7-\delta}$ grains must be aligned. Presently, there are three main techniques for the production of $YBa_2Cu_3O_{7-\delta}$ coated conductors that vary in the way the biaxial texture is

introduced into the system: (*i*) rolling assisted biaxially textured substrate (RA-BiTS), (*ii*) ion beam assisted deposition (IBAD), and (*iii*) inclined substrate deposition (ISD). The IBAD and ISD techniques use a polycrystalline metallic substrate where the biaxial texture is induced into the buffer layer during growth, whereas the RABiTS technique uses a biaxially textured metallic substrate on which buffer and $YBa_2Cu_3O_{7-\delta}$ films are grown epitaxially. All these techniques will be discussed in detail in chapter 4, in particular the RABiTS technique that was used in this work.

The biaxially textured metallic substrate of the RABiTS approach is characterised by a granular structure with small misorientation between the grains. During the epitaxial growth, the grain boundaries of the substrate propagate into the $YBa_2Cu_3O_{7-\delta}$ film forming a $YBa_2Cu_3O_{7-\delta}$ grain boundary network that consists of a large number of grain boundaries with an extended distribution of misorientation angles. As a consequence, the current in the $YBa_2Cu_3O_{7-\delta}$ coated conductor is found to flow percolatively through the sample, crossing only those grain boundaries with the lowest misorientation angles. Magneto-optical measurements on $YBa_2Cu_3O_{7-\delta}$ coated conductors have shown that the misorientation angle should be below $4°$ to prevent the percolative current flow and a resulting reduction in J_c [Fel00]. Often in the $YBa_2Cu_3O_{7-\delta}$ coated conductors, the majority of the grain boundary angles are around $5°$ or even higher. Consequently, $YBa_2Cu_3O_{7-\delta}$ coated conductors have reduced critical current values compared to $YBa_2Cu_3O_{7-\delta}$ films grown on a single crystal substrate.

The aim of this work is the analysis of grain boundary networks of $YBa_2Cu_3O_{7-\delta}$ coated conductors prepared by pulsed laser deposition, and the study of the effects of the granular structure of the samples on the critical current and transport properties. Two critical current limitations are expected to occur in the $YBa_2Cu_3O_{7-\delta}$ coated conductors: (*i*) *intergrain* current limitation by the grain boundaries, and (*ii*) *intragrain* current limitation by flux creep within the YBCO grains, which can be distinguished by a different dependence of the critical current density on the applied magnetic field. Critical current density measurements in magnetic fields on $YBa_2Cu_3O_{7-\delta}$ coated conductors should help to clarify the mechanism for current limitation by the grain boundary network. Moreover for a complete understanding, it is important to consider some interesting properties of low-angle grain boundaries in magnetic fields, such as grain boundary pinning [Día98a], viscous flux flow of flux lines along the grain boundary [Día98a], and a grain boundary angle dependent crossover behaviour from intergrain to intragrain limited critical current density with increasing magnetic field [Ver00].

The present work is divided into seven chapters. The properties of the high temperature superconductors and especially of $YBa_2Cu_3O_{7-\delta}$ are reviewed in chap-

ter 2, including phenomena like flux line pinning, thermal activation processes and the irreversibility field in this material. Chapter 3 deals with the nature of low-angle grain boundaries in $YBa_2Cu_3O_{7-\delta}$ and the transport properties found in these systems. Chapter 4 gives an overview of the preparation techniques for $YBa_2Cu_3O_{7-\delta}$ coated conductors, the technical requirements for power applications, and actual values of critical current density and lengths of the prepared $YBa_2Cu_3O_{7-\delta}$ coated conductors. The experimental description with the different steps and parameters that are required for the preparation of $YBa_2Cu_3O_{7-\delta}$ coated conductors samples by pulsed laser deposition, and the structural and microstructural characterisation of the grain boundary network of the samples are presented in chapter 5. Chapter 6 deals with transport current measurements carried out on the $YBa_2Cu_3O_{7-\delta}$ coated conductors, in particular the magnetic field dependence of the critical current density and voltage-current characteristics. Furthermore, the anisotropy of the critical current density is also analysed in this chapter. Finally, in chapter 7 the results are discussed and conclusions drawn.

Chapter 2

The high-temperature superconductor $YBa_2Cu_3O_{7-\delta}$

2.1 Structural properties

High-temperature superconductors (HTS) have a perovskite structure with CuO_2 planes lying normal to the crystallographic c-direction. This is a common feature of these materials, therefore they are often referred to as cuprates. In the case of $YBa_2Cu_3O_{7-\delta}$ (YBCO), three perovskite units $BaCuO_3$, $YCuO_2$, and $BaCuO_2$ stack vertically forming the superconducting unit cell with some oxygen atoms missing. Similar stacking occurs in other cuprates such as LaSrCuO, BiSrCaCuO, and TlBaCaCuO.

YBCO exists in either a tetragonal or orthorhombic crystal structure (see Fig. 2.1), being only superconducting in the orthorhombic phase. The tetragonal phase is observed at high temperatures in a range between 750 and 900 °C. On decreasing the temperature and increasing the oxygen content of the sample, by oxygen uptake and diffusion, a second-order phase transition occurs at about 700 °C from the tetragonal to the orthorhombic phase.

Both structures have three planes containing Cu and O atoms that are intercalated with two planes containing Ba and O and one plane containing Y. The two median CuO_2 planes show a puckered appearance due to the different positions of the Cu and O atoms in c-direction. The third CuO_2 plane is the basal plane and is flat. In the tetragonal phase the oxygen sites in the basal plane are about half occupied in a random manner, while in the orthorhombic phase they are ordered into Cu-O chains along the b direction (see Fig. 2.1). The oxygen vacancies along the a direction in the orthorhombic phase cause the unit cell to compress slightly so that $a < b$. In the orthorhombic phase, both the CuO_2 planes and the Cu-O chains contribute to the superconductivity; the CuO_2 planes contain mobile charge
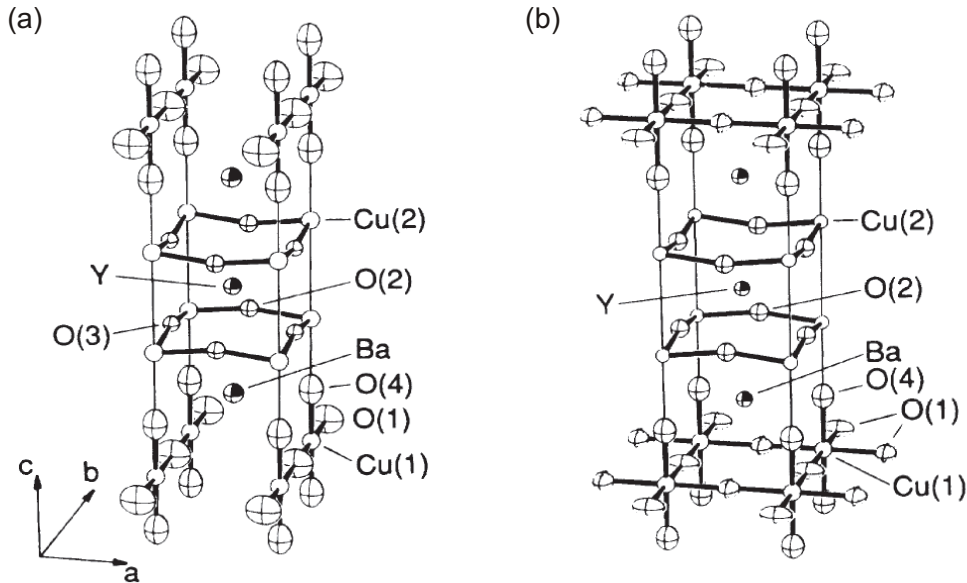
Fig. 2.1: Sketches of the unit cell of the orthorhombic (a) and tetragonal (b) phases of YBCO [Jor87]. Representative lattice parameters for the orthorhombic phase of YBCO are a = 3.827 Å, b = 3.882 Å, and c =11.682 Å.

carriers (holes), and the Cu-O chains act as charge reservoirs that transfer holes to the planes.

The oxygen content in YBCO determines its crystallographic structure [Fig. 2.2 (a)] and the hole concentration in the CuO$_2$ plane [RM91, Tal95, Bre95]. For an oxygen content $x = 6$ the compound YBa$_2$Cu$_3$O$_6$ is in the tetragonal phase and is an insulator. Increasing the oxygen content up to $x = 6.6$, the compound undergoes a phase transition from tetragonal to orthorhombic. Finally, raising x to 6.94, T_c approaches its maximum value (93 K). Above $x = 6.94$, T_c drops by about 4 K [see Fig. 2.2 (b)]. The maximum T_c value found for $x = 6.94$ is due to an optimum hole doping of the CuO$_2$ planes. The drop in T_c for x above 6.94 can be explained as an overdoping, where the holes in the CuO$_2$ planes exceed the optimum concentration.

2.2 YBa$_2$Cu$_3$O$_{7-\delta}$ as an anisotropic type II superconductor

Superconductors are classified as type I and type II, depending on whether the Ginzburg-Landau parameter κ is smaller or larger than $1/\sqrt{2}$, respectively. The
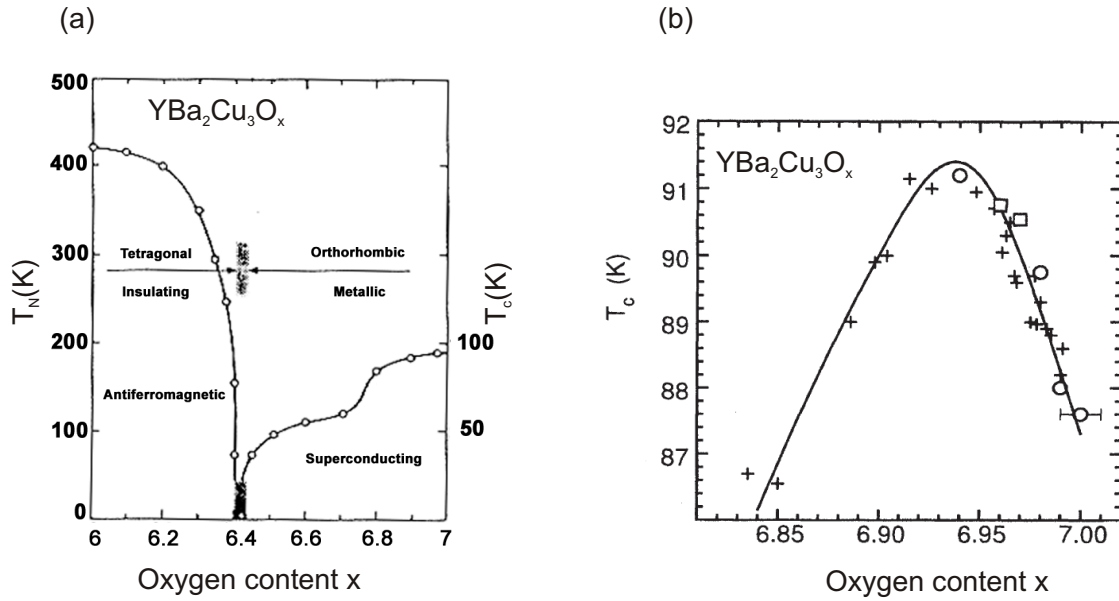
Fig. 2.2: (a) Phase diagram of the YBa2Cu3O$_{7-\delta}$ system as a function of the oxygen content. T_N represents the Néel temperature of the antiferromagnetic phase, and T_c the critical temperature of the superconducting phase [RM91]; (b) Variation of T_c with oxygen content [Bre95].

Ginzburg-Landau parameter κ is defined as

$$\kappa = \frac{\lambda}{\zeta_{GL}} \tag{2.1}$$

where λ describes the penetration depth of a magnetic field into the superconductor, and ζ_{GL} is a characteristic length over which the Cooper-pair density increases from 0 to its maximum value $n_c(T)$. Nearly, all the elemental superconductors except Nb, V, and Tc are type I, while most superconducting compounds are type II.

Type I superconductors possess only one critical magnetic field B_c, below which the superconductor produces shielding currents that flow on the surface of the material expelling the magnetic field from inside. In this situation, the superconductor is in the Meissner phase. Above B_c, the applied magnetic field penetrates completely into the interior of the material, disrupting the superconductivity.

Type II superconductors have two critical fields, a lower critical field B_{c1} and an upper critical field B_{c2}. Figure 2.3 (a) shows the typical $B - T$ phase diagram of a type II superconductor. Below B_{c1}, the superconductor behaves like a type I superconductor and remains in the Meissner phase. When the applied magnetic field
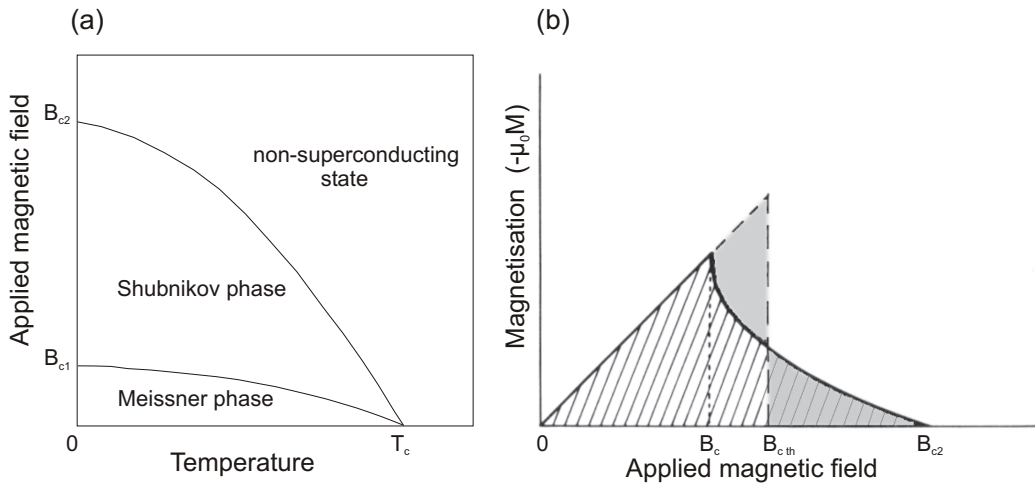
Fig. 2.3: (a) Typical $B - T$ phase diagram of a type II superconductor; (b) Magnetisation curve of a type II superconductor[Buc91].

exceeds B_{c1}, it penetrates into the material in the form of flux lines called vortices [1]. For applied fields close to B_{c2}, the vortices begin to overlap and the field inside the superconductor becomes strong everywhere. When the applied field reaches B_{c2}, the material becomes non-superconducting. The magnetisation curve of a type II superconductor is schematically illustrated in Fig. 2.3 (b), showing the same situation as described above. For magnetic fields below B_{c1}, the magnetisation increases equal to the applied magnetic field but in opposite direction (the values of $\mu_0 M$ are negative). When the applied magnetic field reaches B_{c1}, the magnetic field penetrates the superconductor and the magnetisation of the superconductor decreases monotonically with increasing magnetic field. At B_{c2}, there is a discontinuous change in the slope of the magnetisation curve, and above B_{c2} the material is in the normal state. $B_{c\ th}$ represents the thermodynamic critical field that is a measure of the free energy difference between the superconducting and normal state at a constant temperature. The ratio between B_{c2} and $B_{c\ th}$ is such that the area enclosed by the dashed lines equals the area enclosed by the magnetisation curve of the type II superconductors.

The superconducting state between B_{c1} and B_{c2} is known as the mixed state or the Shubnikov phase, and is shown schematically in Fig. 2.4. In this phase the vortices are arranged forming an hexagonal lattice with a lattice parameter a_0 that depends

---

[1]Each vortex has a core that is encompassed by shielding currents. The magnetic field has its maximum value at the axis of the vortex and decreases exponentially over the characteristic length λ.
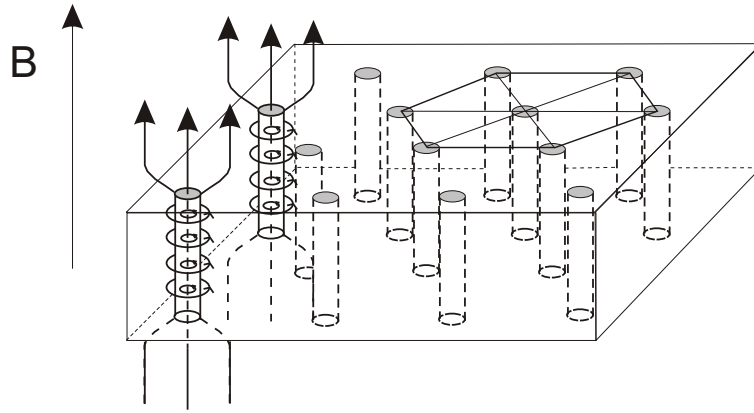
Fig. 2.4: Representation of the Shubnikov phase, where each vortex is surrounded by shielding currents[Buc91].

on B in the form

$$a_0 = 1.075\sqrt{\frac{\Phi_0}{B}}. \tag{2.2}$$

Φ_0 represents the flux quantum that each individual vortex is carrying, and has a value of $\Phi_0 = h/2e \approx 2 \times 10^{-15}$ T m^2 [Tin96, Abr98]. This hexagonal flux line lattice is known as an Abrikosov lattice, because it was Abrikosov who predicted theoretically the mixed state for type II superconductors and the regular arrangement of the flux line lattice in the Shubnikov phase. He deduced that the mixed state is a result of a negative surface energy between the normal and the superconducting phase. Under these circumstances, the total free energy can be lowered by subdivision of the superconductor into superconducting and normal regions. The Abrikosov lattice was first observed experimentally by Essmann and Träuble [Ess67] using a magnetic decoration technique coupled with electron microscopy.

HTS compounds are extreme type II superconductors with large κ values on the order of 100. This is related to their very small ξ_{GL} and large λ values. These materials are also characterised by a strong anisotropy as a consequence of their crystalline structure that is reflected in the directional dependence of λ, ξ_{GL} and B_{c2}. The anisotropy of these parameters is remarkable between the c-direction and the a or b direction, while the anisotropy between the a and b directions is small and can be neglected in most cases. The anisotropy of the HTS compounds can be described using the Ginzburg-Landau theory that introduces a different effective mass of the hole carriers in different directions. The effective mass in the ab plane is denoted by m_{ab}, and along the c axis by m_c. The anisotropy is described by the parameter γ, defined as $\gamma = (m_c/m_{ab})^{1/2} = \lambda_c/\lambda_{ab} = \xi_{ab}/\xi_c = B_{c2}^{ab} / B_{c2}^c$ [Tin96,
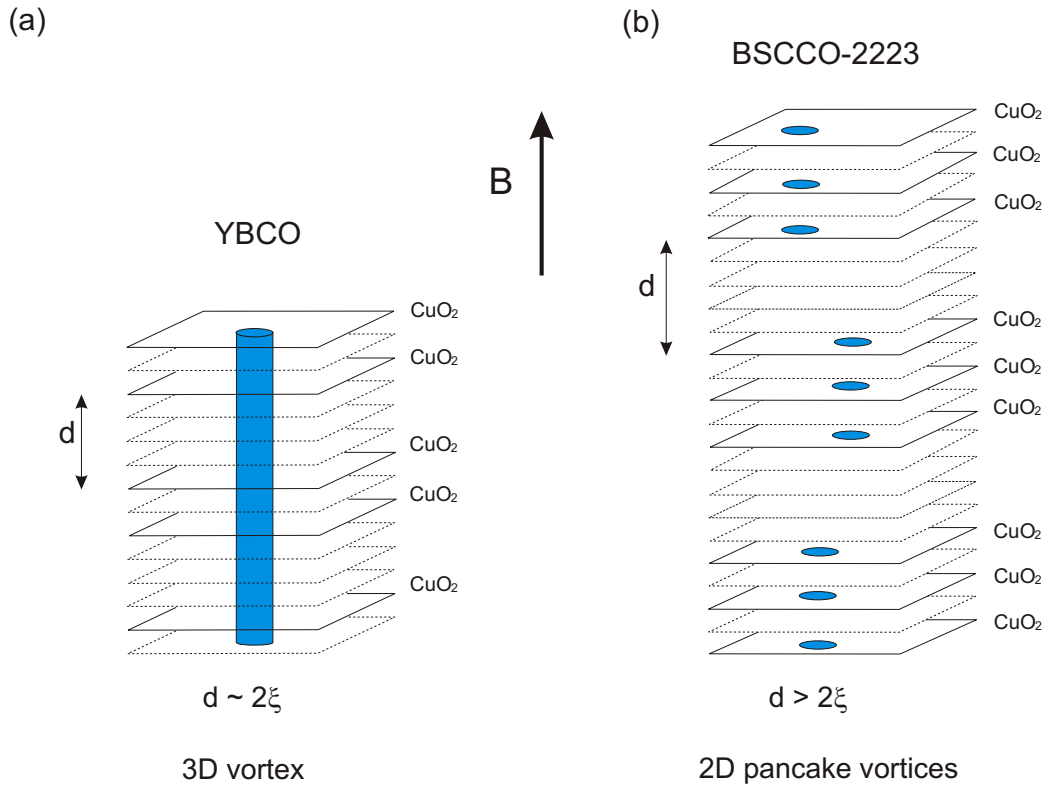
Fig. 2.5: (a) Representation of a three-dimensional flux line in YBCO; (b) Representation of two-dimensional pancake vortices in Bi$_2$Sr$_2$Ca$_2$Cu$_3$O$_x$ (BSCCO-2223).

Cle98] with $\gamma > 1$. The value of γ for YBCO lies between 5 and 8 [Far90], while in Tl$_2$Ba$_2$CaCu$_2$O$_x$ γ is found to be 90 [Gra90] and in Bi$_2$Sr$_2$CaCu$_2$O$_x$ (BSCCO-2212) it exceeds 150 [Mar92, Cle98]. The large γ values of the Tl and especially the Bi compounds indicate a strong anisotropy. On the other hand, YBCO with a relatively small γ value is considered commonly as a nearly isotropic HTS.

The anisotropy in the HTS materials is related to their layered structure and long distances between the CuO$_2$ planes when compared to ξ_c. For YBCO the distance d between the CuO$_2$ planes ($d \approx 8$ Å) is closer to $2\xi_c$ (ξ_c=3 Å at 0 K) than in other HTS, which leads to a stronger coupling between the CuO$_2$ planes and a three dimensional (3D) vortex structure [Fig. 2.5 (a)]. In contrast, for the Bi, Tl and Hg compounds the distance d is much larger than the respective value of $2\xi_c$. This results in a weak coupling between the CuO$_2$ planes that are practically isolated. Consequently, the vortices in these high anisotropic materials dissolve in each CuO$_2$ plane into so-called pancake vortices [Fig. 2.5 (b)], which are two-dimensional (2D) and have a very weak interaction with the pancakes of the adjacent planes. For the strongly anisotropic HTS compounds, a better description than the Ginzburg-
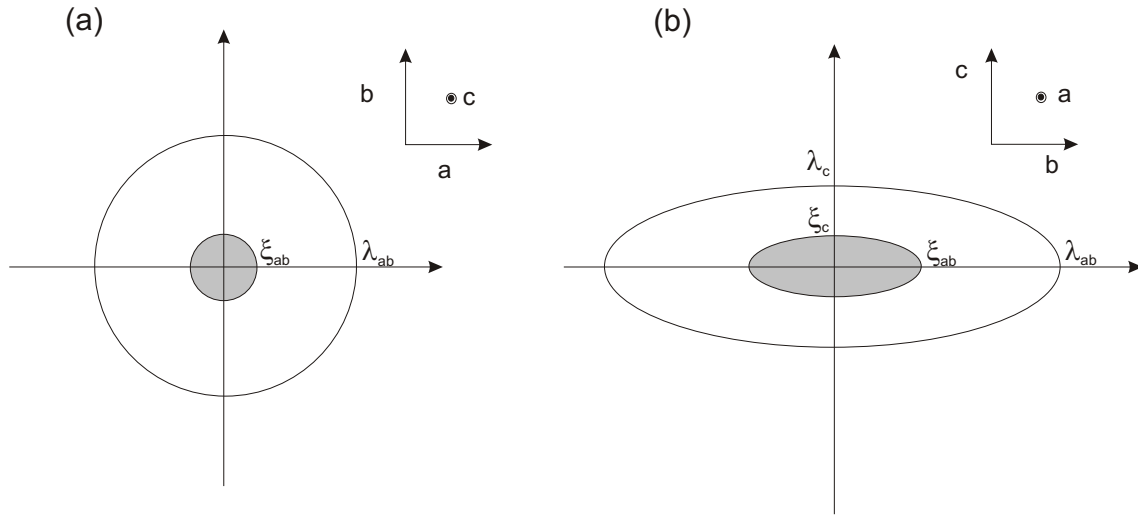
Fig. 2.6: Schematic cross-section of (a) an Abrikosov vortex along the c-axis, and (b) a Josephson vortex along the a-axis.

Landau theory is achieved by a discrete Lawrence-Doniach model, which assumes that a layered superconductor can be approximated as a stack of weakly coupled superconducting layers [Cle91, Cle98]. However, in the case of YBCO, the use of the Ginzburg-Landau theory is more precise over a large temperature regime due to its three dimensional (3D) vortex structure.

2.3   Vortex structure in YBa$_2$Cu$_3$O$_{7-\delta}$

The vortex structure of YBCO varies depending on the orientation of the applied magnetic field with respect to the CuO$_2$ planes. When the applied magnetic field is parallel to the c-axis, the vortices present an axial symmetry with the shielding currents circulating around the cores. In this case, they are named Abrikosov vortices [Fig. 2.6 (a)]. In a homogeneous material with a low number of pinning centers, the Abrikosov vortices form a hexagonal lattice, as mentioned above. In this arrangement the vortices are in the most stable positions, compensating the magnetic interactions.

When the magnetic field is applied parallel to the CuO$_2$ planes, the field penetrates in form of Josephson vortices [Fig. 2.6 (b)] that are characterised by an elliptical core with major axis ξ_{ab} along the a (or b) direction and minor axis ξ_c along the c-direction. This yields elliptical current patterns that circulate around the vortex. The Josephson vortices experience a strong pinning in the interlayer space that prevents the movement of the flux lines in c-direction. This effect is known as
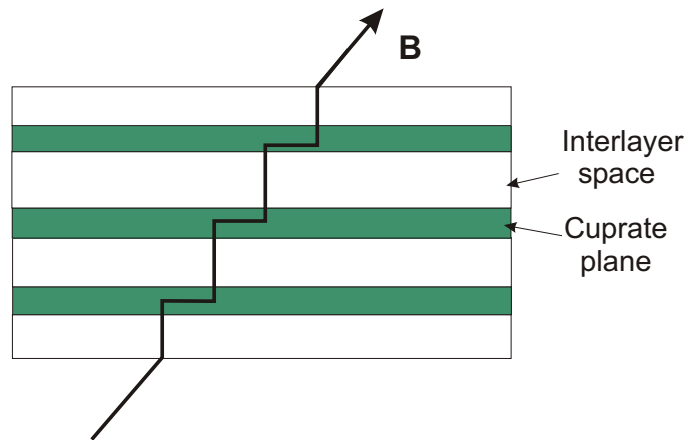
Fig. 2.7: Kinked vortex line in a layered superconductor.

intrinsic pinning and is caused by the modulation of the order parameter[2] in the *c*-direction that decreases strongly in the space between the CuO$_2$ planes. An experimental observation of intrinsic pinning in thin YBCO films was carried out by critical current measurements in applied magnetic fields. A strong enhancement of the critical current was detected when the applied magnetic field was aligned within the CuO$_2$ planes [Roa90a, Roa90b]. In the case of strongly anisotropic HTS compounds like the BSCCO family, intrinsic pinning becomes even more effective than in YBCO because, in these materials, the order parameter decreases practically to zero between the CuO$_2$ planes [Sch91].

In an inclined magnetic field the vortices in YBCO have a kinked structure as shown in Fig. 2.7 that can be described by Abrikosov vortices parallel to the *c* axis, and Josephson strings (short segments of Josephson vortices) confined in the interlayer space between the CuO$_2$ planes. In this geometry, the critical current is lower than that when critical current density is aligned parallel to the CuO$_2$ planes [Bla94, Kes90].

2.4   Flux Line Pinning

When an external current density $\vec{J}$ flows along a superconducting sample that is in the Shubnikov phase, the flux lines start to move under the action of the Lorentz force $\vec{F}_L = \vec{J} \times \vec{B}$. Within a perfectly homogeneous system the driving Lorentz force is counteracted only by the friction force $\vec{F}_\eta = -\eta \vec{v}$, where $\vec{v}$ is the steady-state velocity of the vortex system, and η represents the friction coefficient. The

---

[2]The Ginzburg-Landau theory is formulated in terms of the order parameter $\phi(\vec{r})$, whose amplitude squared $|\phi|^2$ is the supercarrier density n_s^*.

consequence of the flux motion is the appearance of a finite electric field $\vec{E} = \vec{B} \times \vec{v}$ in the superconductor. The electric field has a component with the same direction as $\vec{J}$, giving rise to the ohmic loss $\vec{J} \cdot \vec{E}$,

$$\vec{J} \cdot \vec{E} = \vec{J} \cdot (\vec{B} \times \vec{v}) \tag{2.3}$$

In this situation, the desired superconducting property of dissipation-free current flow is lost. In order to recover it, the flux lines have to be fixed to pinning centres in such a way that $\vec{v} = 0$. The force that holds the core of the flux lines at the pinning centres is called pinning force F_p, and it allows the system to sustain the Lorentz force between the flux lines and the current without flux motion and dissipation. In the case that the Lorentz force equals the pinning force the depinning critical current density J_{dp} is achieved, and the flux lines start to move producing dissipation. In conventional type II superconductors the critical current density J_c can be identified with J_{dp}. In HTS, on the other hand, dissipation processes already occur before J_{dp} is reached. Hence, J_c is lower than J_{dp} in these materials.

Pinning centres in a superconductor result from structural inhomogeneities in the material that yield a local reduction in the order parameter. Therefore, a vortex can reduce its free energy when positioned on a pinning centre. The energy saved by a pinned vortex, which is related to the intersection volume $V_{intersec}$ between the pinning centre and the flux line, is called pinning energy $U_p = (B_c^2/2\mu_0)V_{intersec}$. In HTS materials, pinning centres should be on the scale of ξ_{GL} to be effective. This kind of pinning is known as core pinning. Due to the characteristically short coherence lengths of these materials, the pinning is expected to be weak compared to that in conventional type II superconductors. The high J_c values found in HTS can be explained only by the presence of a large number of pinning centres. Typical pinning centres found in HTS are twin boundaries, stacking faults, screw dislocations, low-angle grain boundaries [Lai90, Man92, Día98b] and oxygen vacancies. All of these, except for oxygen vacancies, can be considered as strong pinning centres that act separately with individual pinning forces f_p. In this case, the elasticity of the flux line lattice is neglected [see Fig. 2.8 (a)], and the total volume pinning force density P_v may be expressed as the sum of the pinning force on each vortex,

$$P_v = nf_p \tag{2.4}$$

where n corresponds to the density of pinning centres, and f_p is the average pinning force per unit length on each vortex line.

Oxygen vacancies in the HTS are weak pinning centres that exist in large number and are randomly distributed. Here, the dynamical behaviour of the vortex system has to be studied considering a *collective pinning theory* proposed by Larkin and Ovchinnikov [Ovc91]. This theory considers flux lines as elastic objects that

(a)   (b)
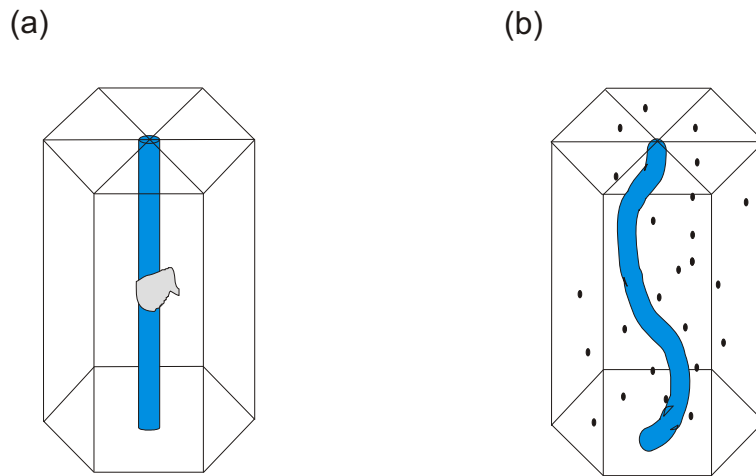
Fig. 2.8: (a) Flux line pinning by a strong pinning centre, in which case the elasticity of a flux line is not considered; (b) Deformation of a 3D flux line due to collective pinning by weak pinning centres, in which case the elasticity of the vortex plays an important role in the pinning process.

can deviate from the ideal periodic arrangement of the Abrikosov lattice to gain energy by passing through favourable pinning sites as shown in Fig. 2.8 (b). The equilibrium flux line lattice configuration will be a distorted arrangement which minimises the total pinning and the elastic energy due to deformation of the flux line lattice. The collective pinning describes the distortion of the flux line lattice in terms of correlated volumes V_c termed flux bundles, within which the flux line lattice is reasonably undistorted, but between which exist pinning-motivated shear and tilt distortions. The length of the flux bundle is denoted by L_c along the field direction, and R_c represents the radius of the bundle. An important point is the relation between L_c and the distance d between the CuO$_2$ planes in the superconductor. For $L_c > d$ the pinning has a 3D nature, while for $L_c < d$ the pinning mechanism changes to 2D behaviour. For YBCO only 3D collective pinning has to be considered.

2.5   Thermally activated flux motion

At finite temperatures, the thermal energy may allow flux lines to jump from one pinning centre to another in response to the driving Lorentz force, even if the Lorentz force is smaller than the pinning force. The resulting flux motion in type II superconductors is revealed in two ways, leading to slow changes in the trapped magnetic fields with a logarithmic time-dependence, and to measurable resistive voltages. Anderson and Kim introduced a model to study the thermally
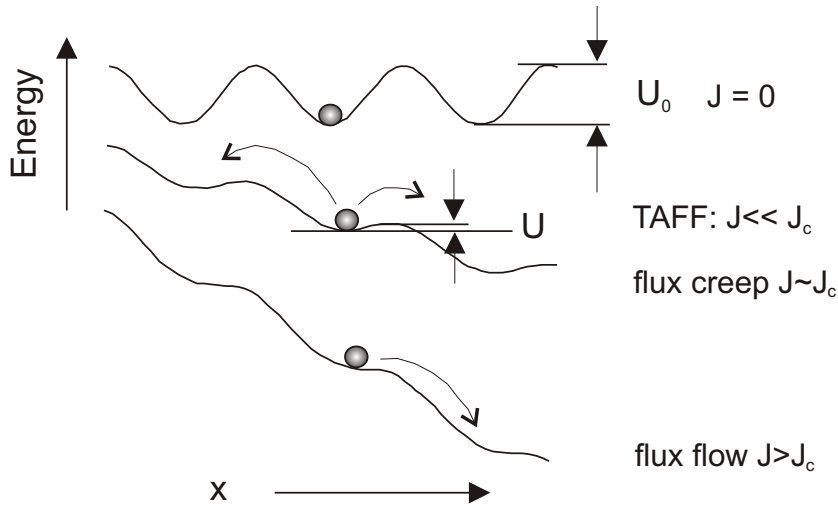
Fig. 2.9: Schematic representation of a vortex or flux bundle in an one-dimensional pinning potential well U; the upper curve shows the unperturbed potential U_0 for $J = 0$, the lower curves show the effect of depinning on the potential well, which gives rise to the different thermal activation processes: thermally activated flux flow (TAFF), and flux creep. Finally flux flow appears when the Lorentz force overcomes the pinning force.

activated processes and to describe the magnetic relaxation in type II superconductors [And62, And64].

2.5.1   Anderson-Kim model for thermal activation

Anderson and Kim assumed that activated flux motion occurs by bundles of flux lines jumping between adjacent pinning sites. In this model the elastic properties of the flux bundle are neglected, and each bundle at $T > 0$ and $J = 0$ jumps like an unit with a jump rate R to overcome the pinning potential U_0:

$$R = \omega_0 \exp\left(\frac{-U_0}{k_B T}\right) \tag{2.5}$$

where ω_0 is the vibration frequency of the flux bundle in the potential minimum, and lies in the range of 10^5 to 10^{10} s^{-1}.

If a current J is applied, a Lorentz energy U_L will perturb the pinning potential U_0, leading to a pinning potential $U = U_0 - U_L$ that depends on J (see Fig. 2.9). U_L is defined as $U_L = |\vec{J} \times \vec{B}| V r_p$, where V represents the volume of the flux bundle and r_p the interaction range of the pinning potential. If the applied current J and the magnetic field B are perpendicular, then $U_L = JBV_c r_p$. In this situation the rate

of forward (R_+) and reverse (R_-) hopping in the direction of the Lorentz force is given by,

$$R_\pm = \omega_0 \exp\left(\frac{-U_0 \mp J\,B\,V_c\,r_p}{k_B T}\right) \tag{2.6}$$

The net hopping rate $R = R_+ - R_-$ of a flux bundle leads to a drift velocity v given by $v = RL$, where L is the average jump distance of the flux bundle. The movement of the flux bundles generates an electric field E. If the electric field is in the current direction, it is defined by $E = vB$, yielding

$$E(J) = E_0 \exp\left(\frac{-U_0}{k_B T}\right) \cdot \sinh\left(\frac{U_0}{k_B T}\frac{J}{J_c}\right) \tag{2.7}$$

Depending on the proximity of J with respect to J_c, the previous relation describes two different thermal activation processes: thermally activated flux flow (TAFF) and flux creep.

1. **Thermally activated flux flow (TAFF)**

   The TAFF regime is observed for $J \ll J_c$. In the limit of small current densities, the sinh term can be approximated to a linear relation. This results in an ohmic regime of thermally activated flux flow,

   $$E(J) \approx E_0 \exp\left(\frac{-U_0}{k_B T}\right) \cdot \frac{U_0\,J}{k_B T J_c} = \rho\,J \tag{2.8}$$

   Thus, in the TAFF regime the $E - J$ curves are linear (see Fig. 2.10), and ρ represents the TAFF resistivity,

   $$\rho = \frac{E_0}{J_c} \cdot \frac{U_0}{k_B T} \cdot \exp\left(\frac{-U_0}{k_B T}\right) \tag{2.9}$$

2. **Flux creep**

   For large currents approaching the critical current density ($J \approx J_c$), the activation energy U becomes small, and hence the jump rate of reverse hopping R_- of the flux bundles is negligible (see Fig. 2.9 for flux creep). This leads to

   $$E(J) = E_0 \exp\left[\frac{U_0}{k_B T} \cdot \left(\frac{J}{J_c} - 1\right)\right] = E_0(-U(J)/k_B T) \tag{2.10}$$

   In the flux-creep regime, the $E - J$ curves are expected to be exponential and the electric field increases strongly with the current (see Fig. 2.10).
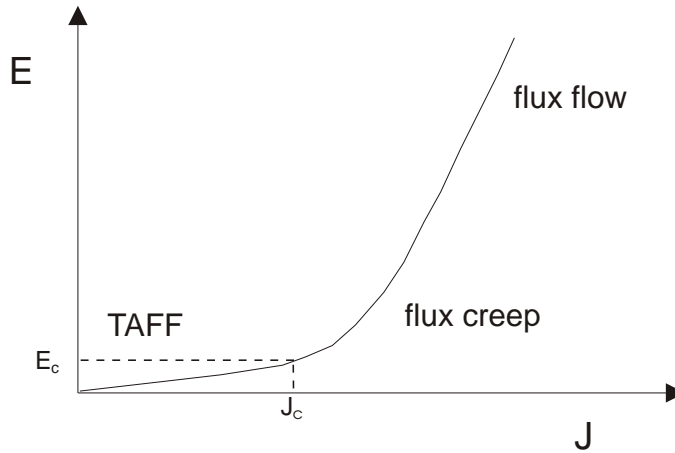
Fig. 2.10: Schematic representation of the $E - J$ curves in type II superconductors.

In HTS compounds, both thermally activated processes (TAFF and flux creep) are very important and dominate the dissipation process. In contrast, in conventional type II superconductors thermally activated processes occur only at temperatures close to T_c or for current densities close to J_c.

For $J \gg J_c$ flux pinning becomes negligible or zero, and the Lorentz force is counteracted only by the friction force $\vec{F}_\eta = -\eta\vec{v}$. This is the *flux flow* regime, where a differential flux flow resistivity ρ_{flow} appears, which is independent of current [Bar65]:

$$\rho_{flow} \simeq \rho_n \frac{B}{B_{c2}} \tag{2.11}$$

where ρ_n represents the resistivity in the normal state. In the flux flow regime the $E - J$ curves are linear, showing an ohmic behaviour. Figure 2.10 summaries the $E - J$ characteristics in the three different regimes: TAFF, flux creep and flux flow.

2.5.2 Thermal activation in high-T_c materials

As previously mentioned, in HTS materials the thermal activation processes are considerably stronger than in conventional type II superconductors. This is a consequence of: (*i*) the short coherence length ξ_{GL}, (*ii*) the layered structure with high structural anisotropy, and (*iii*) the high operation temperatures that yield high thermal energies ($k_B T$) also for $T \ll T_c$ or $J \ll J_c$. $U(B, T, J)$ represents the activation energy, and can be used to describe the interaction that the flux lines have with the pinning centres. Taking into account that for currents approaching J_c the activation energy becomes zero, $U(J)$ is relevant for the study of the dynamic

of flux lines in the superconductor. Several models propose different expressions for $U(J)$ depending on the pinning mechanism that is considered. In the *Anderson-Kim model*, where the flux lines or bundles are treated as a unit, the pinning energy $U(J)$ is assumed to be:

$$U(J) = U_0 \left| 1 - \frac{J}{J_c} \right| \tag{2.12}$$

which implies that $U(J)$ has a triangular shape, with a linear dependence of U on J. As a refinement of this model, a more realistic shape of $U(J)$ has been suggested by several authors [Bea69, Gri91],

$$U(J) = U_0 \left| 1 - \frac{J}{J_c} \right|^n \tag{2.13}$$

where the exponent varies between 1.5 and 2, determining the curvature of the pinning potential.

Zeldov *et al.* [Zel89, Zel90] have proposed a phenomenological activation barrier to account for $E - J$ characteristics in the presence of high magnetic fields. In this *phenomenological model* $U(J)$ is given by

$$U(J) = U_0 \, ln \left(\frac{J}{J_c} \right) \tag{2.14}$$

The logarithmic dependence of $U(J)$ is based on experimental measurements carried out on YBCO thin films and other HTS materials. Considering the expression 2.10 of the electric field due to flux creep, the $E - J$ characteristics in this model are obtained as

$$E(J) = E_0 \exp\left[\frac{-U(J)}{k_B T} \right] = E_0 \left(\frac{J}{J_c} \right)^{p(T,B)} \tag{2.15}$$

Thus, the electric field depends on the current density as a power law with a power

$$p(T, B) = \frac{U_0(T, B)}{k_B T} \tag{2.16}$$

that introduces the dependency on temperature and magnetic field.

Such assumptions for $U(J)$ are valid for strong pinning centres, but not for collective pinning by many weak pinning sites, as is the case for the oxygen vacancies in the HTS materials. For this case, the *collective pinning theory* introduces a new $U(J)$ dependence,

$$U(J) \approx U_0 \left(\frac{J_c}{J} \right)^{\mu} \tag{2.17}$$

with a characteristic exponent $\mu > 0$. Such a relation has been found experimentally in flux creep measurements by Maley *et al.* [Mal90]. The exponent μ defines the size of the flux bundles and the dimensionality of the flux line lattice. In the case of 3D pinning, as in YBCO, the theoretically expected values for the exponent μ are 1/7 for single-vortex collective pinning ($R_c < a_0$), 3/2 for small vortex bundles ($R_c \approx a_0$), and 7/9 for large bundles. It is expected that the regime changes from the single-vortex regime at high J towards the large-bundle regime at low J, passing through the small-bundle regime at intermediate J.

The relation 2.17 reveals that for J going to zero the activation energy approaches infinity. Consequently, flux motion and linear resistance vanish, even if the voltage remains finite at finite current densities. This contrasts to the Anderson-Kim model that shows a $U(J)$, having a finite activation energy when J approaches zero: $U(J \to 0) = U_0$.

In this model, the $E - J$ characteristics are given by,

$$E(J) = E_0 \exp\left[\frac{-U(J)}{k_B T}\right] = E_0 \exp\left[\frac{-U_0}{k_B T} \cdot \left(\frac{J_c}{J}\right)^{\mu}\right] \qquad \mu > 0 \tag{2.18}$$

2.6 The flux vortex phase diagram in YBa$_2$Cu$_3$O$_{7-\delta}$

Vortex matter exists in different phases depending on temperature and magnetic field: the Bragg glass, vortex glass, and vortex liquid (Fig. 2.11). The Bragg glass is an partially ordered "solid" phase, where the vortices are arranged in a non-perfect Abrikosov lattice, while the vortex glass is a completely disordered "solid" phase, where the flux line lattice shows a glassy structure caused by disordered pinning centres. The so-called vortex liquid is found at higher temperatures and magnetic fields. In this phase the vortex lattice has no long-range order; the vortices do not present coupling and move independently. Consequently, in the vortex liquid phase an electrical resistance is detected. The transition from the Bragg glass into the vortex liquid takes place at the melting temperature $T_m(B)$, and is a first order transition. Commonly, this transition is not detected in HTS thin films or bulk materials that have a high density of pinning centres. The Bragg glass phase is only observed in very homogeneous materials with low density of pinning centres, such as the case of the YBCO single crystal that was needed to obtain the phase diagram of Fig. 2.11. The transition from the vortex glass to the vortex liquid occurs at the glass temperature $T_g(B)$. This transition is defined as the dividing point between temperatures where the resistance is zero (vortex glass), and those for which it is non-zero (vortex liquid). This definition is equal to the one for the irreversibility field line (see section 2.7), therefore both irreversibility field and $T_g(B)$ represent nearly the same transition in the flux line lattice (see
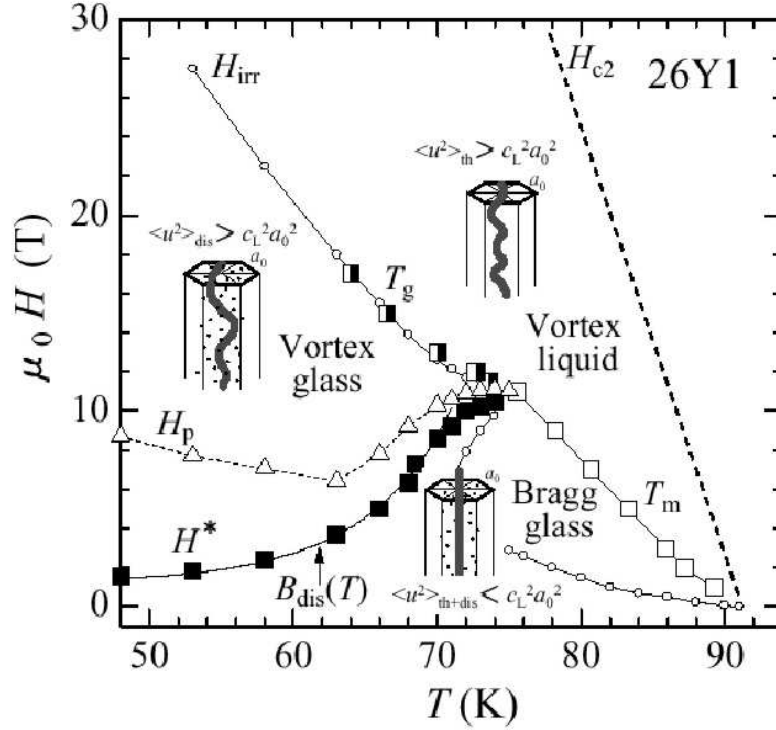
Fig. 2.11: The vortex matter phase diagram in untwinned YBCO [Nis00].

Fig. 2.11). In samples with a high pinning centre density, the transition between vortex glass and vortex liquid has been observed in the analysis of the $E - J$ characteristics [Koc89]. The authors analysed the $E - J$ curves measured on a YBCO thin film, considering the vortex glass theory formulated by Fisher [Fis89] that takes into account the effects of thermal activation and disorder induced by weak pinning centres. In this theory, the $E - J$ characteristics in the field-temperature region are obtained by a scaling approach. For temperatures below the transition, the $E - J$ characteristics can be expressed as

$$E(J) \propto \exp\left[-\left(\frac{J_c}{J}\right)^{\mu} \right] \qquad 0 < \mu \leq 1. \tag{2.19}$$

This implies that the resistance $\rho = E/J$ vanishes in the limit of low current densities. At the phase transition, $T = T_g(B)$, a power law behaviour $E \approx J^{\beta}$ for the $E - J$ characteristics is obtained. Above the phase transition, $T > T_g(B)$, the $E - J$ characteristics indicate a non-zero resistance at relatively low currents that changes to power law behaviour for higher currents.

2.7 Irreversibility line

The existence of an irreversibility line $B_{irr}(T)$ that lies below $B_{c2}(T)$ on a B versus T phase diagram is an important point to consider for practical applications of HTS (see Fig. 2.12). The position of $B_{irr}(T)$ is profoundly dependent on the nature and density of pinning centres in a material, and determines the range where flux line pinning is effective. Between $B_{irr}(T)$ and $B_{c2}(T)$ the superconductor is in the mixed state, but the thermal activation processes are so strong that the material presents a substantial electrical resistance due to flux motion. Therefore, above $B_{irr}(T)$ the critical current density vanishes ($J_c = 0$), while below $B_{irr}(T)$ the critical current density has a finite value ($J_c > 0$). The $B_{irr}(T)$ lines of different cuprates are shown in Fig. 2.13. YBCO reveals the highest irreversibility fields compared to the Tl or Bi compounds. This is a consequence of the relatively isotropic structure of YBCO that leads to a 3D behaviour of its flux line lattice and a stronger pinning than in other cuprates. In highly anisotropic materials (e.g. BSCCO), the 2D behaviour of the flux line lattice causes weaker pinning and strong thermally activated flux motion that moves the irreversibility line towards lower values.
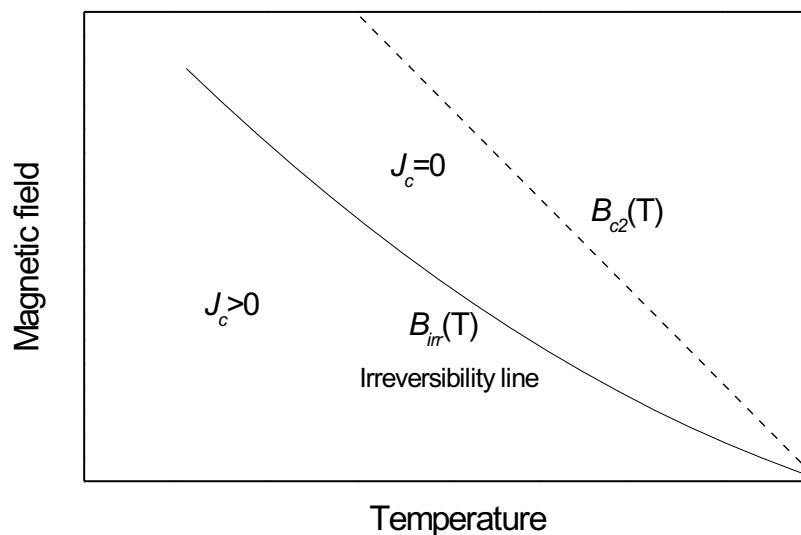

Fig. 2.12: Position of the irreversibility line $B_{irr}(T)$ in the $B(T)$ phase diagram. $B_{irr}(T)$ is found below $B_{c2}(T)$ and divides the states where the critical current density J_c of the superconductor is characterised by $J_c = 0$ and $J_c > 0$.
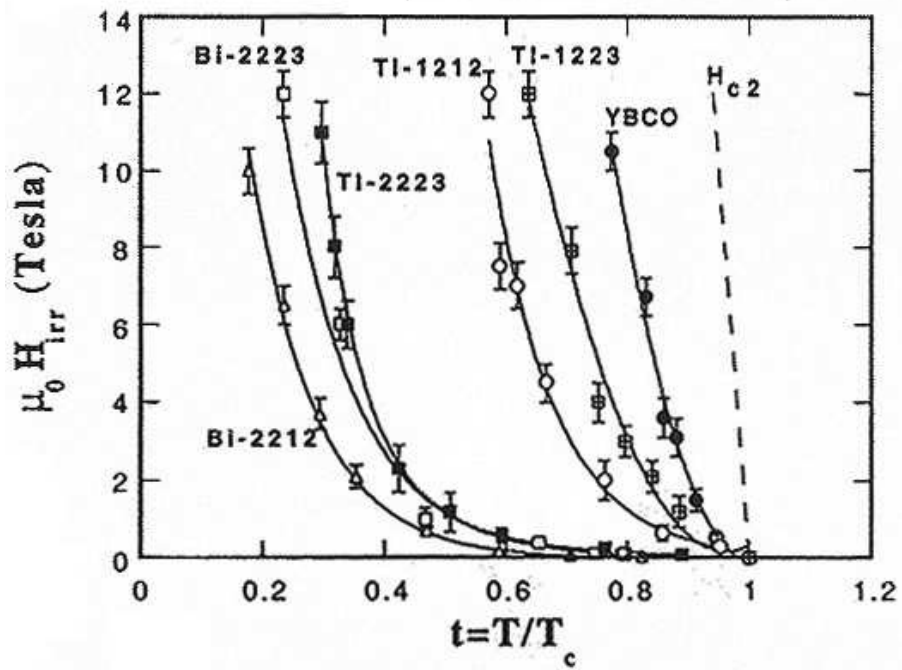
Fig. 2.13: The irreversibility line in various cuprates [Wal96].

Chapter 3

Grain boundaries in HTS materials

At present, there are numerous applications of HTS materials where the grain boundaries (GBs) play an important role, e.g., electronic circuits, sensors, superconducting quantum interference devices (SQUIDs) and power cables. Especially, the critical current density J_c is influenced by the GBs in a complex manner. Polycrystalline HTS samples have typical J_c values of a few hundred A/cm^2 at 4.2 K, while single crystalline samples have values in the range of MA/cm^2. A GB introduces structural disorder that in the case of HTS materials strongly affects the order parameter in the region of the boundary. Considering the degree of connectivity, it can be distinguished between low-angle GBs having strong coupling between the grains, and high-angle GBs with a weak coupling. Transmission electron microscopy (TEM) investigations reveal that low-angle GBs consist of an array of uniformly spaced dislocations produced to accommodate the mismatch between adjacent grains [Chi89, Chi91]. Figure 3.1 shows schematically such a low-angle grain boundary. For small misorientation angles θ, the dislocations are separated by channels of a nearly undisturbed lattice. In the standard GB theory, the distance d between the dislocation cores is given by Frank's formula,

$$d = |\vec{b}| / \sin \theta \qquad (3.1)$$

where $|\vec{b}|$ is the magnitude of the Burgers vector $\vec{b}$ [Hir82]. The distance between dislocation cores reduces with increasing GB angle, with the result that for misorientation angles of approximately $10°$ the dislocation cores overlap leading to an area with high structural disorder and a reduced order parameter [Dim90, Chi91]. These GBs are named high-angle grain boundaries and present typical Josephson junction characteristics [1].

---

[1] A Josephson junction is formed when two superconductors are separated by a thin layer of insulating material. In this situation Cooper pairs are able to tunnel through the insulator from one superconductor to the other. The supercurrent through the contact $I = I_{max} \sin(\phi_2 - \phi_1)$ is related to the phase difference $\phi_2 - \phi_1$ between the order parameters of both superconductors [Jos62].
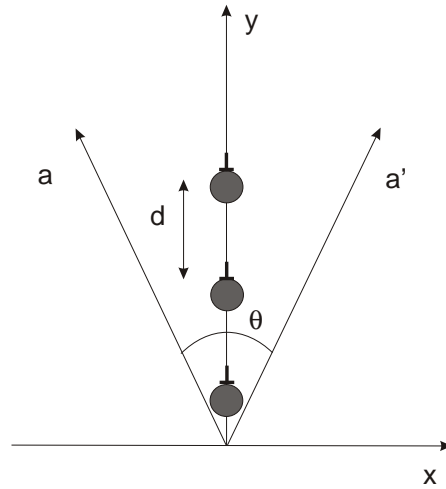
Fig. 3.1: Chain of edge dislocations which form a symmetric low-angle grain boundary in the $y - z$ plane. The non- superconducting regions are shadowed.

GBs are usually classified according to the misorientation and rotation of the adjacent grains. Figure 3.2 presents the three different types of grain boundary geometry. In the [001] tilt boundary [Fig. 3.2 (a)], the c-axes are perpendicular to the plane of the film so that the CuO_2 planes in the adjacent grains are parallel to each other. The angle θ between the principal in-plane directions defines the misorientation (tilt) angle. In Fig. 3.2 (b), the c-axes of the adjacent grains are misaligned by an angle ϕ in a plane normal to the grain boundary plane; this misorientation produces a [100] tilt boundary. In Fig. 3.2 (c), the misorientation angle γ between the c-axes is in a plane parallel to the boundary. In the latter case, the a (or b) axes are normal to the boundary plane so that a [010] twist boundary is formed. GBs with identical misorientations of the grains with respect to the boundary are called symmetric, otherwise they are asymmetric. For a detailed investigation of GBs and their transport properties, they can be produced artificially by growing epitaxially
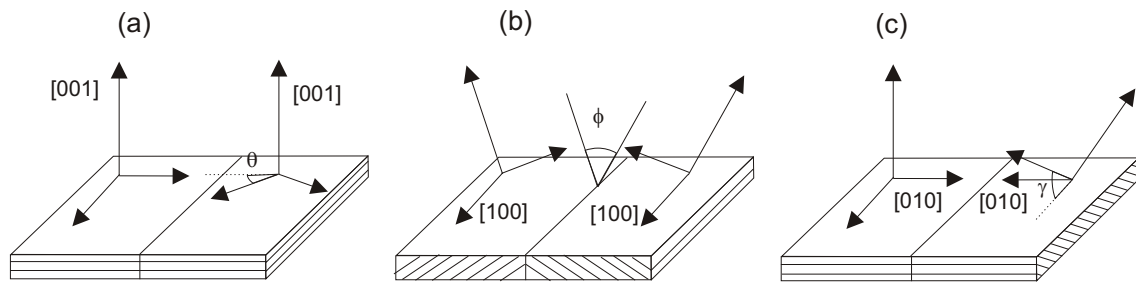
Fig. 3.2: Sketch showing the crystallography of (a) a [001] tilt boundary, (b) a [100] tilt boundary, and (c) a [010] twist boundary.

HTS films on bicrystal substrates, which consist of two crystals with different crystallographic orientations that are fused together. In the epitaxial growth process, the GB of the substrate is carried into the HTS film.

3.1 Nature of grain boundaries in HTS materials

The critical current density across a GB, J_c^{GB} (intergrain critical current density), has been reported by many authors to decrease exponentially with increasing GB misorientation angle θ [Dim90, Iva91] (see Fig. 3.3). Some other authors have suggested a plateau at low misorientation angles where J_c^{GB} is not reduced. In the literature, critical angles for this plateau (where J_c^{GB} begins to drop) between $2°$ and $5°$ have been reported [Dim88, Ver00, Hol00]. Considering the work of Holzapfel *et al.* [Hol00] that proposes a cut-off angle of $4°$, the J_c dependence on the misorientation angle for YBCO can be phenomenologically quantified as

$$\frac{J_c(\theta)}{J_c(0)} = \exp\left(-\frac{\theta}{\alpha}\right); \quad [\theta \geq 4°] \tag{3.2}$$

Fig. 3.3: Critical current density ratio in YBCO films as a function of the misorientation angle. The different symbols distinguish the different GBs [Dim90].

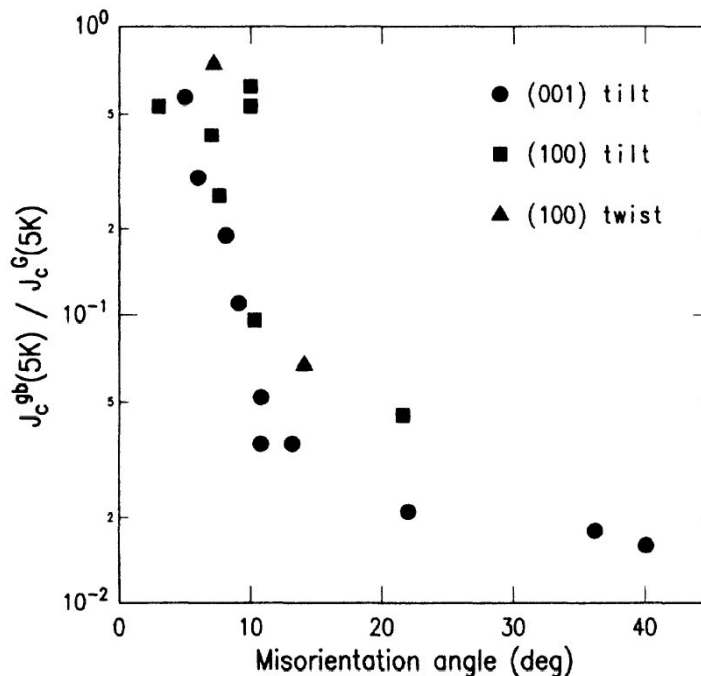with $\alpha = 3.2°$ and $J_c(0) = 3.2 \, \text{MA/cm}^2$, at 77 K and self-field. A similar exponential dependence of J_c with the misorientation angle has been reported in all three different GB geometries described in Fig. 3.2, and for many HTS materials, e.g., $NdBa_2Cu_3O_{7-\delta}$ [Rom01], $Bi_2Sr_2CaCu_2O_{8+\delta}$ [Amr95], $Bi_2Sr_2Ca_2Cu_3O_{10+\delta}$ [Hän02, Att02], $Tl_2Ba_2CaCu_2O_{8+\delta}$ [Sar94], $TlBa_2Ca_2Cu_3O_x$ [Nab94], $HgBa_2CaCu_2O_{6+\delta}$ [Tsu98] and $Nd_{2-x}Ce_xCuO_4$ [Woo99].

There are several mechanisms that can account for the observed decrease of the critical current density at the GB. Such mechanisms are connected with a reduction of the current-carrying cross-section by the insulating dislocation cores and by local suppression of the order parameter at the GB if the GB misorientation angle increases.

- **Strain field**

  Each GB dislocation has an associated strain field. The strained regions around the dislocation core produce a strong reduction in the hole carrier density and a modification of the electronic structure by introducing oxygen defects. Furthermore, it could be demonstrated that the width of the strained area increases linearly with increasing misorientation angle [Chi91, Bro98].

- **Stoichiometry deviations**

  Deviations from the ideal stoichiometry found in GBs are associated with the disorder in these regions and lead to a lower carrier density at the GBs compared to the bulk material [Bro98]. Typical stoichiometrical deviations are oxygen vacancies. As the oxygen concentration may be non-uniform, the GB may be highly inhomogeneous so that the supercurrent flows in filaments across the boundary. Increasing the concentration of oxygen vacancies, the width of the non-superconducting zones between the channels becomes larger, reducing the transport properties [Moe93]. If the oxygen concentration becomes very low in YBCO, a transformation to the tetragonal phase may occur locally at the GB.

- **Interface charging**

  HTS are characterised by a large dielectric constant and a low carrier density that lead to the formation of space charge layers at the GB. This results in a band bending of the band structure next to the interface, and a reduction of the hole carrier density [Man99, Hil99b] (see Fig. 3.4). Similar band bending occurs in GBs of dielectric or ferroelectric oxides and semiconductors. The space charge layers extend into the superconducting grains over the Thomas-Fermi electrostatic screening length λ_{TF} that is in the range of 5 - 10 Å and is comparable to the coherence length of the HTS. For a strong depletion of the
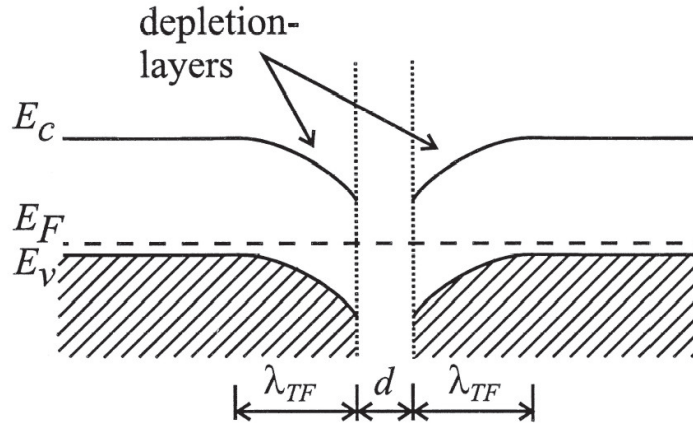
Fig. 3.4: Sketch of the band bending at a GB. E_c and E_v represent the conduction and valence bands, respectively, and E_F represents the Fermi level. λ_{TF} is the electrostatic screening length, and represents the distance over which the depletion takes place [Man99].

band structure, it is expected that the cuprate undergoes a phase transition into the antiferromagnetic insulating phase. Several experimental investigations revealed that a selective doping of the GBs by Ca is a possibility to enhance the hole carrier density at the GBs, and reduce the band bending at the interface. In this doping process, Y^{3+} is replaced by Ca^{2+} producing overdoping of the CuO_2 planes [Hil99a, Hil99b, Sch99, Man00a, Man00b]. Selective doping of the GBs is required to avoid a reduction of T_c in the bulk due to overdoping. Bilayer and trilayer samples of intercalated $YBa_2Cu_3O_{7-\delta}$ and $Y_{1-x}Ca_xBa_2Cu_3O_{7-\delta}$ layers were produced by Hammerl *et al.* [Ham00], inducing diffusion of calcium into the GBs of the pure YBCO layers by postannealing of the samples. Such heterostructures yielded critical current densities as high as 0.3 MA/cm^2 for a 24° YBCO bicrystal at 77 K. An improvement in J_c was also detected in Ca-doping experiments of low-angle grain boundaries with 4° and 8° [Gut01, Dan00], however it is found that the enhancement in J_c by Ca-doping is stronger in high-angle grain boundaries.

- *d*-**wave symmetry**

  The HTS cuprates are characterised by a mixed $s/d_{x^2-y^2}$ wave symmetry of the order parameter, although the $d_{x^2-y^2}$ symmetry is dominant. This
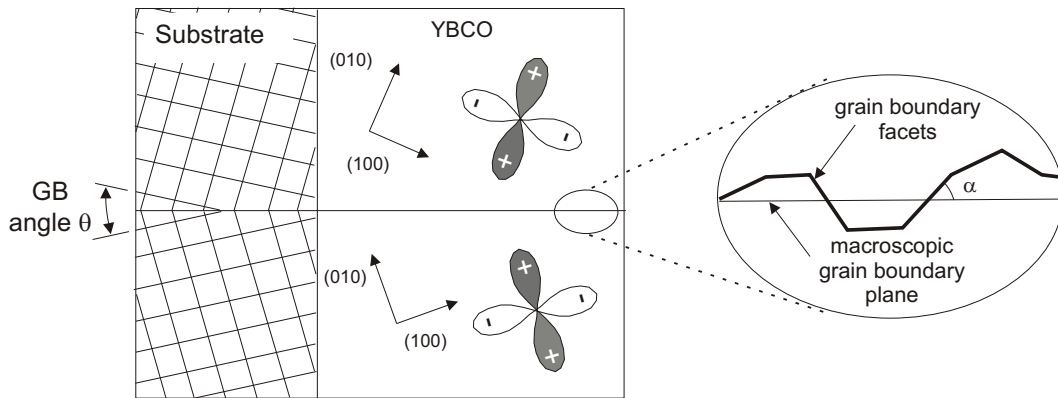
Fig. 3.5: Illustration of the mechanism by which the critical current density of a GB with misorientation angle θ is depressed by the tilting of the $d_{x^2-y^2}$-wave symmetry of the order parameter. The faceting of the GB is also illustrated [Hil96].

was shown by several experiments based on Josephson tunneling between two HTS materials with a conventional superconductor as barrier [Kou97, Wol93], and also with tricrystal junctions [Tsu94]. It is expected that a contact with a misorientation angle θ between $d_{x^2-y^2}$-wave superconductors produces a reduction of the component of the order parameter perpendicular to the grain boundary plane caused by the different crystallographic orientations on either side of the boundary (see Fig. 3.5). The strongest depression of the order parameter is produced in the case of a 45° [001] tilt boundary due to the coincidence of the maximum of the order parameter of the superconductor on one side of the interface with the node in the gap function on the other side.

Faceting of grain boundaries is a further point that has to be considered in the reduction of J_c. As a consequence of the growth modes of the cuprates, the boundaries are not well defined, but consist of several segments with different orientations (see Fig. 3.5). TEM investigations on bicrystals showed facet patterns with typical dimensions of the order of 10 to 100 nm [Cai98]. Faceting together with $d_{x^2-y^2}$ symmetry causes the critical current density to be very inhomogeneous across the boundary. Both effects account for a considerable part of the experimentally observed reduction of the critical current with misorientation angle.

- **Direct suppression of the pairing mechanism**

  The misorientation and the interruption of the periodic lattice structure at the GB depresses the pairing interaction, for example by interrupting the antiferromagnetic order of the CuO_2 planes, which directly affects J_c.

It is not possible to estimate which mechanism has the largest effect on J_c. All of them are interconnected, and the predominance of any of them depends on the kind of GB, which itself might depend on the preparation method.

3.2 Transport properties of low-angle grain boundaries

3.2.1 Voltage-current characteristics

Models of low-angle GBs propose a weaker flux pinning of vortices at the GBs compared to the flux pinning within the grains. The pinning in the GBs is due to a reduction of the order parameter in the dislocation cores, which is produced by several factors commented in section 3.1. Gurevich *et al.* found that, at the boundary, the cores of the conventional Abrikosov (A) vortices turn into Abrikosov Josephson (AJ) vortices [Gur94, Gur98, Gur02]. AJ vortices have a highly anisotropic Josephson core with a length l along the GB, and a width ξ_{GL} (coherence length) in the transverse direction, being l much larger than the size of the dislocation cores (typically on the order of ξ_{GL}) (see Fig. 3.6). This implies that in the direction along the GB plain AJ vortices are weaker pinned. Consequently, if the applied current density J perpendicular to the boundary is high enough, the line of intergrain vortices pinned at the GB will move along the boundary by *viscous flux flow* in response to the Lorentz force, while the A vortices surrounding the GB stay pinned in the YBCO grains. The situation is sketched in Fig. 3.7, and was experimentally observed by Díaz *et al.* [Día98b]. The movement of vortices along the GB generates a voltage V across the boundary over a very short distance (the intervortex distance a_0) that results in an electric field located exclusively at the boundary, which is relatively high and well above the range of fields produced by flux creep. This leads to a linear behaviour of the $V(J)$ curves measured at low-angle GBs, in contrast to the power law found in $V(J)$ curves measured in YBCO single crystals that is produced by flux creep effects when J is close to J_c. Figure 3.8 presents $V(I)$ curves measured by Díaz *et al.* [Día98b] on a YBCO bicrystal with a $4°$ GB. The authors have patterned conducting paths (bridges) on different positions of the sample: one bridge within the grain (IG bridge) and the second one crossing the GB perpendicularly (GB bridge).
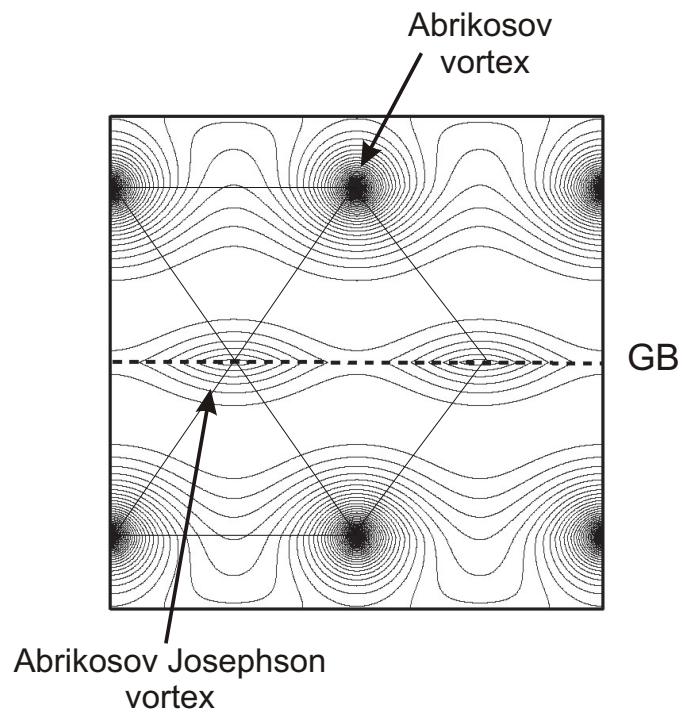
Fig. 3.6: Calculated lines of current around Abrikosov Josephson (AJ) vortices at a GB (dashed line), and the bulk Abrikosov (A) vortices in the grains [Gur02].
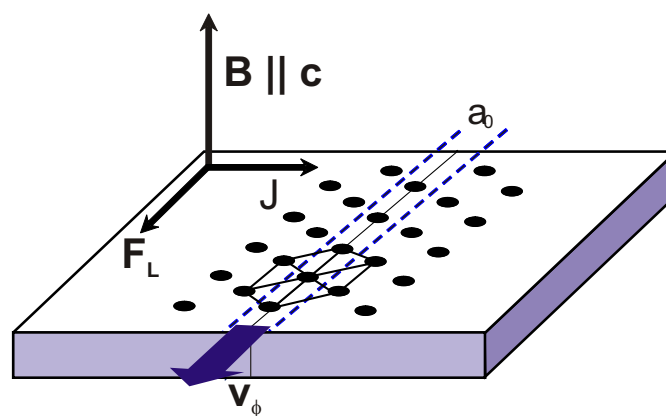
Fig. 3.7: Sketch of the hexagonal vortex lattice in the vicinity of a [100] tilt low-angle GB. For an applied field $\vec{B}$ within the plane of the GB, parallel to the c-axis of the film, vortices are pinned by dislocation cores in the boundary. For $J > J_c^{GB}$, however, vortices in the grain boundary start to move due to the Lorentz force $\vec{F}_L$ directed along the GB [Día98b].
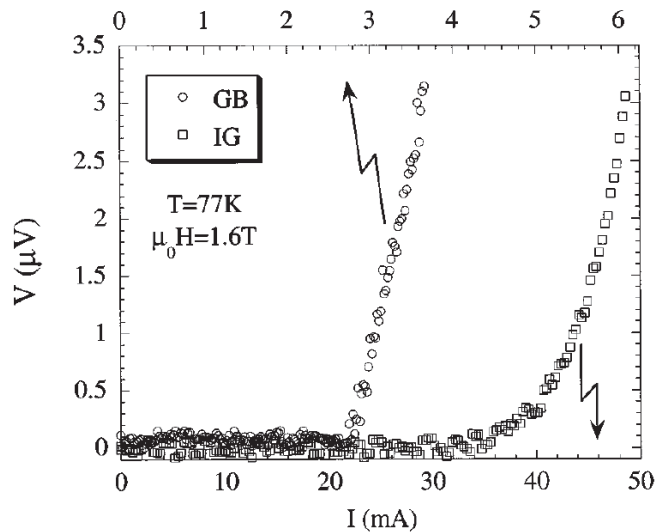
Fig. 3.8: Measured voltage-current density $V(I)$ characteristics for a $4°$ GB and the intragrain bridge. The IG curve shows a power law behaviour due to flux creep, while the GB trace is clearly linear, being characteristic of flux flow [Día98b].

Additionally, another phenomenon called *vortex channelling* is observed in the $V - J$ measurements of low-angle GBs, directly related to viscous flux flow of flux lines, but with a change in the number of vortex rows flowing at the low-angle GB. This results in a variation of the dissipation width at the GB that yields a J_c profile across the interface: J_c increases from a minimum value within the GB to a maximum value given by the intragrain J_c [Fig. 3.9 (a)]. Vortex channelling is detected as a kinking of the $V(J)$ curves into several linear segments with different gradients dV/dJ [Hog01] [Fig. 3.9 (b)]. The channelling of flux lines along the GB is directly connected to the vortex spacing and vortex size, i.e., it depends on the magnetic field and temperature.

3.2.2 Critical current density

Usually, J_c in a single crystalline HTS film decreases strongly under applied magnetic field due to thermally activated flux creep, yielding an exponential $J_c(B)$ dependence. Several experimental investigations, however, found a different $J_c(B)$ dependence for low-angle grain boundaries [Ver00]. This is thought to be a result of pinning in the dislocation cores of the GB that configure a planar distribution of pinning centres with a characteristic low-field dependence $J_c(B) \propto B^{-1/2}$ [Cam72, Gur94]. Such a behaviour has been observed in both conventional superconductors and HTS materials [Cam72, Gur93, Yam93].
Results of $J_c(B)$ measurements reveal that at high magnetic fields the dependence
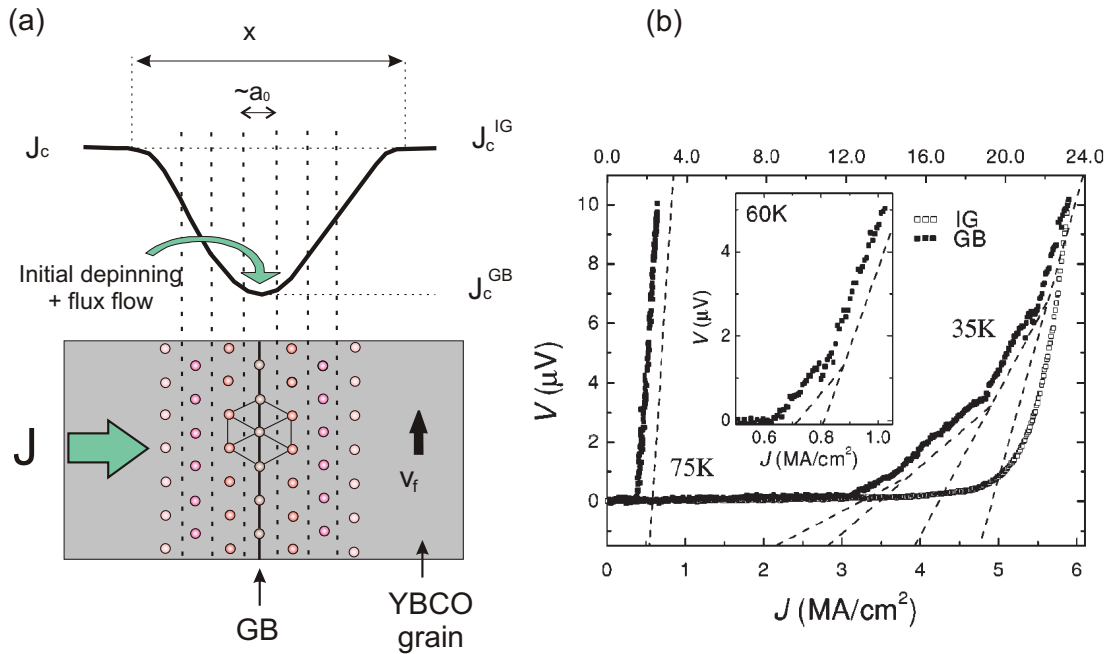
Fig. 3.9: (a) Proposed effective J_c profile across a low-angle GB. Vortices will initially be depinned at the low-angle GB, and as J increases, the surrounding intragrain vortex rows will move progressively; (b) $V(J)$ measurement taken at 1 T for a 4° low-angle GB. A kinking between the different linear segments with different gradients dV/dJ is observed [Hog01].

$J_c(B) \propto B^{-1/2}$ is no longer valid, and a crossover to the normal flux creep mechanism discussed above occurs (Fig. 3.10). This crossover behaviour is caused by the dominance of flux creep effects of the intragrain vortices pinned in the grains, which become especially important when the applied magnetic field increases. The crossover between the power law $J_c(B) \propto B^{-1/2}$ and the exponential dependence of $J_c(B)$ occurs at a crossover magnetic field B^{cr}, which is found to depend on the misorientation angle of the GB [Hol00]. The crossover behaviour between GB and flux creep limitation of $J_c(B)$ is demonstrated in Fig. 3.10 for bicrystals with misorientation angles of 4.5° and 7° [Ver00]. The 4.5° and 7° bicrystals present a crossover field of 3 and 5 T, respectively. In the case of the 2° bicrystal, there is a perfect coincidence of the $J_c(B)$ measurements for the bridges crossing the GB and the one patterned onto a single grain, which is in accordance with the phenomenologically quantified behaviour found for $J_c(B)$, where J_c^{GB} equals the intragrain critical current density J_c^{IG} for small misorientation angles [Hei99] (see section 3.1).

Vortex pinning by dislocation cores in a low-angle GB becomes evident in J_c mea-
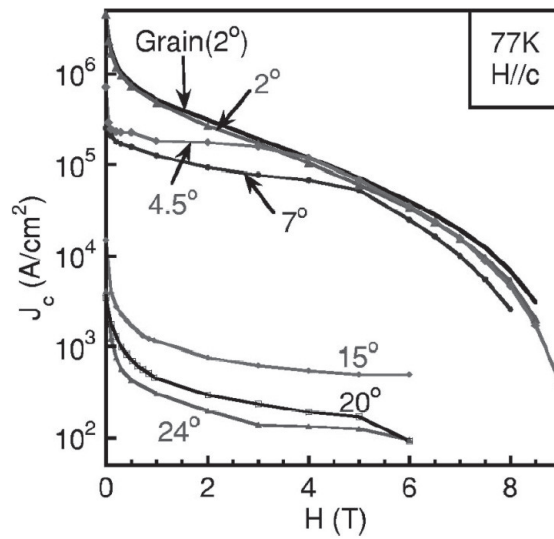
Fig. 3.10: Magnetic field dependence of bicrystal samples with different GB misorientation angles. Above $4°$, the GBs show a reduced J_c. At high magnetic fields and low θ, J_c is dominated by flux creep within the grains and not longer by flux flow in the GBs [Ver00].
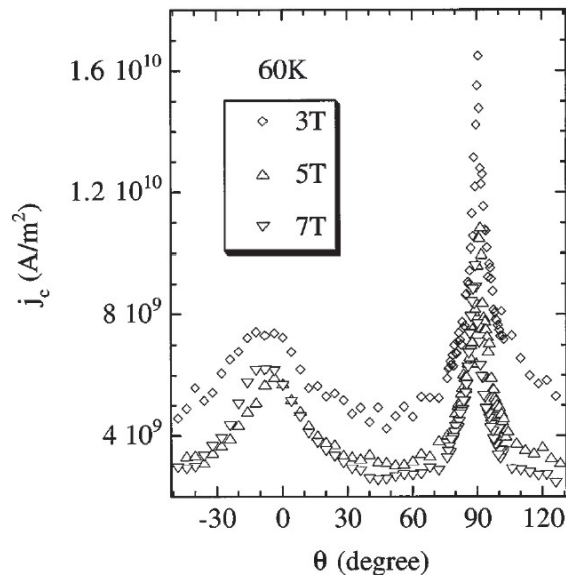
Fig. 3.11: $J_c(\theta)$ curves measured at T = 60 K by Díaz *et al.* on a $4°$ GB. At $\theta = 0°$, the applied magnetic field is aligned parallel to the dislocation cores, detecting a local maximum. For $\theta = 90°$, the applied magnetic is parallel to the CuO_2 planes, and a further maximum in $J_c(B)$ is detected, caused by intrinsic pinning [Día98a].

surements carried out by varying the direction of the applied magnetic field [Día98a, Gur94]. When the magnetic field is aligned parallel to the dislocation cores in the c-direction, a maximum J_c value is detected (see Fig. 3.11), independent of the maximum J_c caused by intrinsic pinning.

Chapter 4

YBa$_2$Cu$_3$O$_{7-\delta}$ coated conductors

YBa$_2$Cu$_3$O$_{7-\delta}$ coated conductors (YBCO CCs) are the so-called "second genera-tion" of high-temperature superconducting tapes and represent an attractive alter-native to the "first generation" Bi$_2$Sr$_2$Ca$_2$Cu$_3$O$_{10+\delta}$ (BSCCO-2223) conductors. At present, several manufacturers in Europe, Japan and the USA are able to fabricate kilometer lengths of BSCCO-2223 tapes using the oxide powder in tube (OPIT) technique. In this technique, oxide powders of the superconductor are loaded into silver or silver alloy tubes, which are sealed, and then drawn into round wires. The round wire is then further rolled to produce a flat tape which is then thermally processed generating a HTS conductor [Hei89, Fis98]. The BSCCO-2223 tapes have disadvantages like the extremely strong reduction of the critical current density J_c in substantial magnetic fields (exceeding 0.2 T) at liquid nitrogen temperature (77 K), and the relatively high raw material and production costs. The comparison between $J_c(B)$ of BSCCO-2223 tapes and that of YBCO CCs at 75 K is shown in Fig. 4.1. BSCCO compounds are characterised by an intrinsically weak flux pin-ning that results in a strong reduction in J_c as the magnetic field increases. YBCO however, has better flux pinning properties and higher irreversibility fields that make it suitable for applications in magnetic fields at 77 K. Moreover, it is expected that the manufacturing costs of YBCO CCs will be two to five times lower than in the case of BSCCO conductors, reaching values of 10 $ per kA m.

Currently, industry and the scientific community are working in close cooperation to improve and develop techniques for the production of high quality YBCO CC tapes and their implementation in power application devices (transmission cables, motors, generators, transformers and fault current limiters) where high magnetic fields are present. The use of YBCO CCs might save energy in power generation and distribution resulting in economic and environmental gains. Furthermore, a substantial reduction in size and weight of all these devices by about 50% is expected.
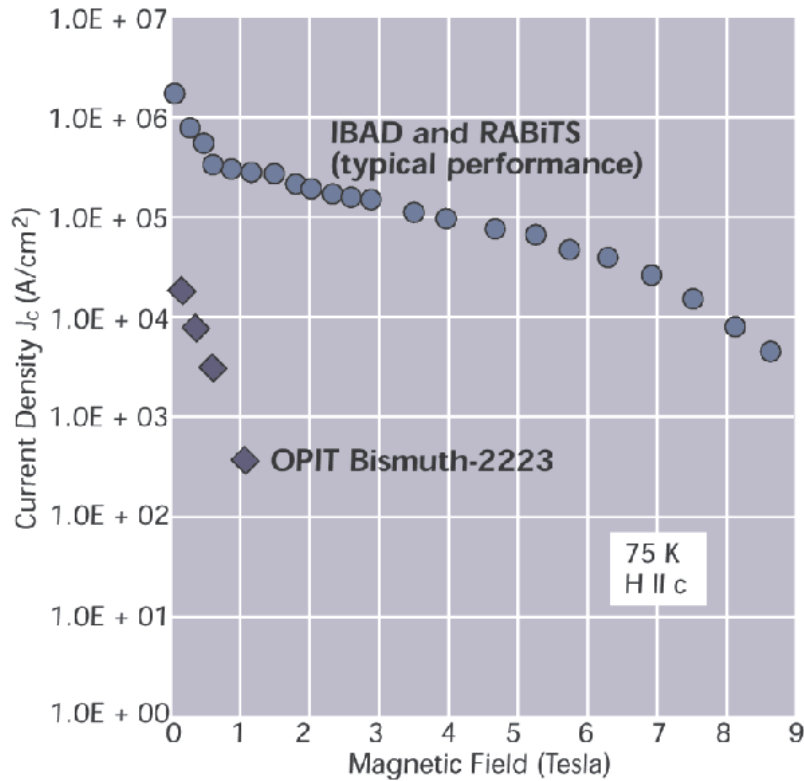
Fig. 4.1: $J_c(B)$ for OPIT BSCCO-2223 and YBCO CCs at 75 K [USD98].

4.1 Technical requirements for YBa$_2$Cu$_3$O$_{7-\delta}$ coated conductors

YBCO CCs have some technical requirements that have to be fulfilled to enable their implementation in power applications. One of the most challenging problems is the production of long YBCO CCs, which means the scaling of the production from a short to a longer sample fabrication by a continuous preparation process. This requires significant modification of the equipment and the necessary incorporation of reel-to-reel handling, as indicated in Fig. 4.2, for all the processing steps: substrate preparation, and buffer layers and YBCO film deposition. The achievement of long CCs is a technical problem due to the necessity of a homogeneous heating and oxygenation of the long substrate during YBCO deposition to obtain a YBCO CC with constant T_c and J_c values along the tape.

In addition to the length problem, there are other tasks in the optimisation of the YBCO CCs that have to be solved: the substrate has to be flexible, non-magnetic and thin with the necessary mechanical strength to allow the production of cables
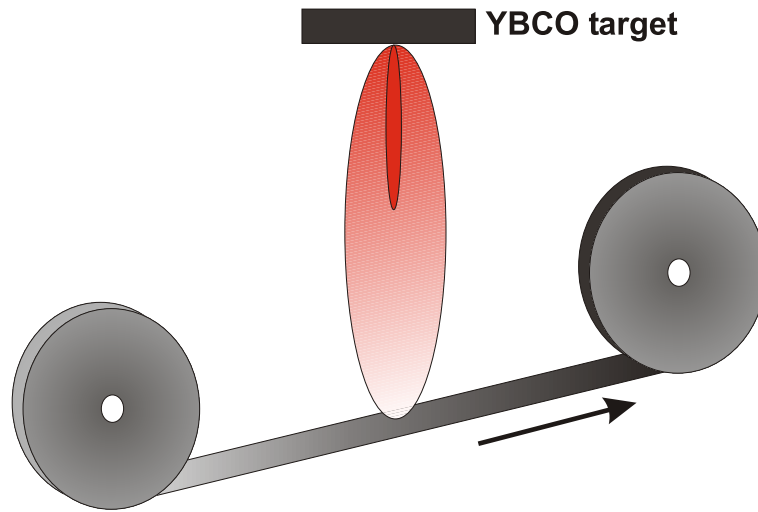
Fig. 4.2: Reel-to-reel handling during pulsed laser deposition of long lengths of YBCO CC

or coils and, on the other hand, the YBCO film has to be thick enough to improve the current capability of the YBCO CC.

4.1.1 Metallic substrates

The substrate plays a crucial role in the YBCO CC. It should be flexible and possess good mechanical strength. Metals are the ideal candidates with obvious benefits for the preparation of long and flexible tapes at relatively low cost. The thickness of the substrate is an important point for the engineering critical current density (J_e), which takes into account the complete cross-sectional area of the CC. Hence, the substrate should be as thin as possible, and the YBCO film relatively thick. The second point is the ferromagnetism of the substrate that leads to magnetisation losses and increases the total alternating current losses of the YBCO CC [Tho02]. Alternating current losses are important when power-engineering applications are considered; they must be low enough to justify the extra investment in the YBCO CCs. A possible solution is the use of metallic substrates with Curie temperatures well below 77 K.

4.1.2 YBa$_2$Cu$_3$O$_{7-\delta}$ film thickness

It could be expected that the total critical current I_c of the film increases with the thickness d of the YBCO film, yielding a constant J_c. However, it was observed that J_c is a function of film thickness and decreases exponentially when the thickness exceeds 0.5 μm. This J_c reduction was found to be correlated with a transition from

c-axis to *a*-axis orientation for YBCO films grown onto biaxially textured metallic substrates [Leo03]. Foltyn *et al.* investigated the transport capability in dependence of the YBCO film thickness [Fol99]. They prepared 4.7 *μ*m thick YBCO films and found that the current flows only in an approximately 1.25 *μ*m thick layer located in the interior of the thick film. The superconducting properties of the films exceeding a thickness of 1.5 *μ*m were poor due to a low temperature during the growth process. On the other hand, the first 0.25 *μ*m of the 4.7 *μ*m films were equally damaged by a too high substrate temperature. To overcome the problem and obtain thicker YBCO films Jia *et al.* proposed a multilayer architecture consisting of two intercalated layers of 1.1 *μ*m thick YBCO with a 50 nm thick CeO$_2$ layers [Jia01]. The aim of this approach was the reduction of defects like voids, porosity and *a*-axis oriented grains in the YBCO film. The authors observed that both YBCO layers exhibited a similar critical current density of 1.4 to 1.5 MA/cm^2 at 75.2 K . The ability to maintain a constant and high J_c as the total YBCO thickness is increased suggests that even higher total J_c can be reached by adding more layers.

4.2   Preparation routes

The main routes to produce YBCO CCs are ion beam assisted deposition (IBAD), inclined substrate deposition (IBAD) and rolling assisted biaxially textured substrate (RABiTS), as already commented in chapter 1. All of these techniques have achieved critical currents densities J_c higher than 1 MA/cm^2 in short samples [Mat98, Nor98, Bet98, Hol01a, Bau99].

The IBAD and ISD techniques use polycrystalline substrates that in most cases are commercially available low magnetic Ni alloys like Hastelloy, Inconel, or stainless steel. The IBAD technique uses an ion beam that bombards the growing film at a fixed angle during deposition. In this way, it is possible to control the orientation of the film by producing a selective grain growth mechanism and so to develop a biaxial texture in the buffer layer [Fig. 4.3 (a)]. Optimal textures for buffer materials like yttria-stabilized zirconia (YSZ) or MgO have been achieved providing high critical current densities in the subsequently YBCO film [Bet98, Bet97c, Bet97a, Bet97b, Hüh01, Hol01a]. A limitation for this technique is the difficulty of scaling up the ion beam assisted deposition into an industrially viable production process. In the ISD technique, an in-plane textured film is obtained just by inclining the substrate at an angle *α* during deposition [see Fig. 4.3 (b)]. The <110> axis of deposited material is favoured to align towards the direction of the evaporated material. This technique is characterised by very high deposition rates (approximately 300 nm/min.). For MgO buffer layers good results were obtained evaporating the
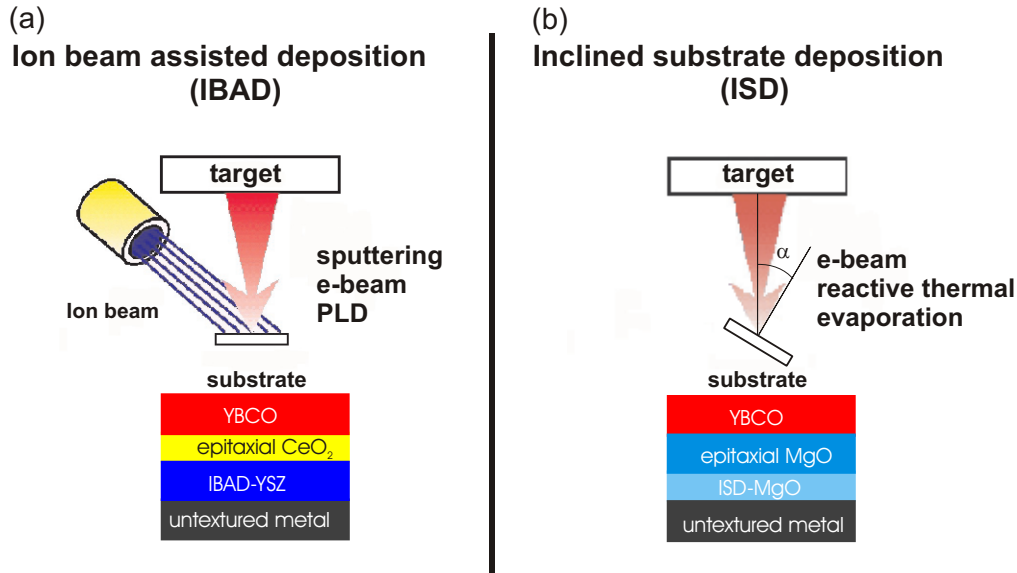
Fig. 4.3: Sketch of the two techniques that use complete polycrystalline substrates for the production of YBCO CCs: (a) IBAD approach with IBAD-YSZ and epitaxial CeO_2 as buffer layers; (b) ISD approach with ISD-MgO and epitaxial MgO as buffer layer.

layers by e-beam or reactive thermal evaporation of magnesium. Usually, a second MgO film is epitaxially grown on the ISD-MgO to achieve a smoother buffer layer in order to improve the growth of the YBCO film [Bau99, Met01].

In contrast to the former techniques, RABiTS is characterised by the use of a bi-axially textured metallic substrate, on which the buffer layers and YBCO film are epitaxially grown (Fig. 4.4). The RABiTS approach offers a high flexibility, and promises possibilities for the production of long YBCO CCs.

In all three approaches YBCO can be grown using many different deposition techniques, either vacuum techniques [pulsed laser deposition (PLD), sputtering, thermal evaporation, metalorganic epitaxial chemical vapor deposition (MOCVD)] or non-vacuum techniques like chemical solution deposition (CSD) that have been proposed as flexible and low-cost alternative for long tape coating with high critical current densities [Oku01, Fal02, Sie02, Cas03].

Presently, companies and institutions have achieved the production of long YBCO CCs by IBAD, ISD and RABiTS techniques. In Japan, Fujikura Ltd. and Sumitomo Ltd. have produced a 100 m (J_c = 0.8 MA/cm^2) [Iij03] and 50 m (J_c = 0.15 MA/cm^2) [Fuj03] long YBCO CC using IBAD and ISD, respectively. American Superconductor Corporation obtained a length of 10 m with a critical current density of 1.5 MA/cm^2 using the RABiTS technique [Mas03].
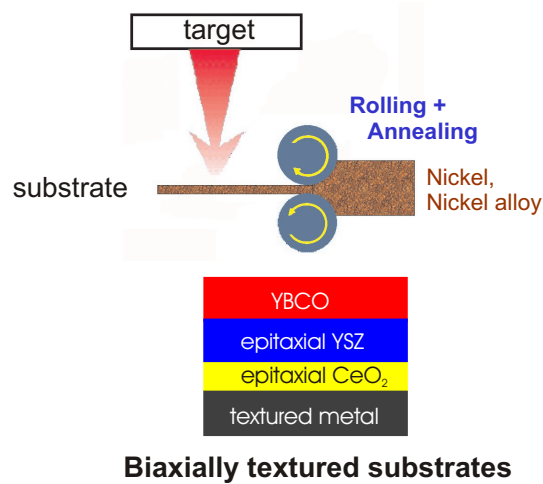
Fig. 4.4: Sketch of the RABiTS technique using epitaxial CeO$_2$ and YSZ as buffer layers.

4.3 The RABiTS approach

The RABiTS approach was first proposed by Norton *et al.* [Nor96], utilising the ability of face-centered cubic (fcc) metals like Cu, Ni or Ag to achieve a strong {100} <100> cube texture by heavy cold rolling and successive recrystallisation. This texture is then transferred to subsequent layers by epitaxial growth.

4.3.1 Biaxially textured metallic substrate

In spite of its ferromagnetism, pure Ni and Ni-based alloys are preferred as substrate materials thanks to their good oxidation resistance compared to Cu or Al. The preparation method used for the production of long tapes of Ni or Ni alloys consists of several steps. First, the elements are melted and alloyed in an induction furnace and cooled to room temperature. The resulting square-shaped rods are heavily cold rolled with several passes down to the final thickness (typically between 40 and 80μm), and finally the samples are annealed at temperatures between 300°C and 1100°C either in a mixed atmosphere of 10% H$_2$ in N$_2$ or in pure H$_2$. In the annealing process a recrystallisation of the substrate material occurs, providing a strong {100} <100> cube texture.

The purity of the elements is an important factor contributing to a sharp texture in the tapes. It can heavily influence the recrystallisation process and abnormal

grain growth may occur and destroy the cube texture. In the case of pure Ni, the abnormal growth can be prevented by alloying with 0.1 at.% of Mo, Mn or W [Eic01, dB01a]. These microalloying additions do not change the properties of the substrate material in comparison to Ni. Both pure and microalloyed Ni are characterised by a low tensile strength that can be improved by a factor of 3 with additions of V and Cr ($\geq$ 10 at.%) [dB01a, dB01b, Sar02]. A higher tensile strength allows thinner tapes, which is desirable to increase the engineering critical current density of the YBCO CC. Additionally, these highly alloyed Ni tapes show Curie temperatures below 77 K, lower than that of pure or microalloyed Ni tapes, which eliminates magnetisation losses in alternating current applications. However, the additions of V and Cr result in an easy V or Cr oxide formation on the substrate surface during buffer deposition, that difficults the epitaxial growth. The problem can be solved by using composite substrates with a non-oxidising outer layer and a highly alloyed inner core. An example is the 80 μm tape prepared by Sarma *et al*. [Sar03a] with a 30 μm core consisting of a Ni-Cr-Al alloy (Ni-10 at.% Cr-1.5 at.% Al) and outer layers of Ni-3 at.% W.

4.3.2 Buffer layer architecture

The buffer layer architecture consists typically of two or three oxide layers, although the development of an effective single layer is desirable. Two principal functions of these buffer layers are to protect the substrate from oxidation, and to act as a chemical barrier avoiding the diffusion of Ni atoms from the substrate into the superconducting film, since a contamination of the YBCO film by Ni diffusion leads to a reduction of T_c [How89, Tar88]. As a diffusion barrier the buffer layer has to be a closed crack-free layer and it must not itself react with the YBCO film. In addition to the barrier function, the buffer layer constitute the template for the epitaxial YBCO film growth and propagate the biaxial texture from the metal substrate to the YBCO film.

Several oxide materials are suitable as layers for coated conductors, since they have a good lattice matching with both YBCO and Ni. The first proposed buffer layer architecture that achieved high J_c values over 1 MA/cm^2 was a combination of CeO$_2$ and YSZ [Nor96, Nor98, Fer02]. This standard buffer layer system consists of a thin layer of CeO$_2$ (50 - 100 nm) followed by a thicker YSZ film that acts as the real diffusion barrier. A variation of this architecture is the addition of a second thin CeO$_2$ buffer layer onto the YSZ layer [Par99a].

Buffer layers of Y$_2$O$_3$, Yb$_2$O$_3$ and Gd$_2$O$_3$ were deposited on RABiTS substrates by reactive e-beam evaporation. A novel buffer layer consisting of a combination of Y$_2$O$_3$ and Yb$_2$O$_3$ was developed, achieving J_c values exceeding 1 MA/cm^2

[Par99b, Ich99]. New potential buffer layers are LaNiO$_3$ and SrRuO$_3$, which have a perovskite structure and conducting properties. The advantage of a conducting buffer is the electrical and thermal stabilisation of the CC against transient conditions in which the current may exceed I_c of the YBCO film generating a very high dissipation power. In the case that the YBCO film is electrically connected to a conducting substrate, the current could be transferred to this reducing the risk of damage. Both layers were prepared by sputtering and PLD on Ni substrates with subsequent YBCO deposition, achieving $J_c = 1.2$ MA/cm^2 [Can01a].

It was found that also NiO can grow biaxially textured on the RABiTS tape under optimised conditions, and therefore, it can be also used as buffer layer. This procedure is known as surface oxidation epitaxy (SOE) [Mat99, Kur03], and its principal problem is the roughness of the grown NiO layer that has to be covered by other oxides like YSZ , Y$_2$O$_3$, SrZrO$_3$ or BaZrO$_3$ to improve the epitaxial growth of the YBa$_2$Cu$_3$O$_{7-\delta}$ film [Don02, Eve03].

Presently, the preparation of buffer layers by CSD techniques is in development. Candidates like La$_2$Zr$_2$O$_7$, Nd$_2$CuO$_4$, CeO$_2$, BaZrO$_3$ and SrTiO$_3$ are being investigated [Oku01, Cas02, Dem03, Hos03].

4.3.3 YBa$_2$Cu$_3$O$_{7-\delta}$ film

The YBCO film deposition can be carried out by any of the techniques already mentioned. A critical point is that the YBCO has to grow biaxially textured, as previously commented in chapter 1. Such a biaxial texture is the only way to eliminate intergranular weak links and achieve high critical current densities ($J_c > 1$ MA/cm^2 at 77 K and B = 0 T). In general, it is found that with the proper buffer layer architecture and deposition parameters, YBCO grows biaxially textured on RABiTS substrates. However, very often J_c is lower than expected (below 1 MA/cm^2). Overlooking Ni diffusion problem into the YBCO film, the principal reason for the low J_c value is the grain boundary network (GBN) propagated from the substrate into the YBCO film by the epitaxial growth. The GBN consist of many GBs with various misorientation angles, which limit the critical current density in a different manner: GBs with misorientation angles below the cut-off angle (3°-5°) do not limit J_c, while misorientation angles above the cut-off angle reduce J_c exponentially (see section 3.1). Such a situation leads to a percolative current flow along the GBN, i.e., the current selects the easiest way to flow in the granular coated conductor. Most often, the GBs that strongly limit J_c are isolated obstacles, around which the current can easily flow. However, it is possible that these randomly located GBs form a barrier that significantly restricts the current flow. This fact points out the importance of the development of well-textured RABiTS
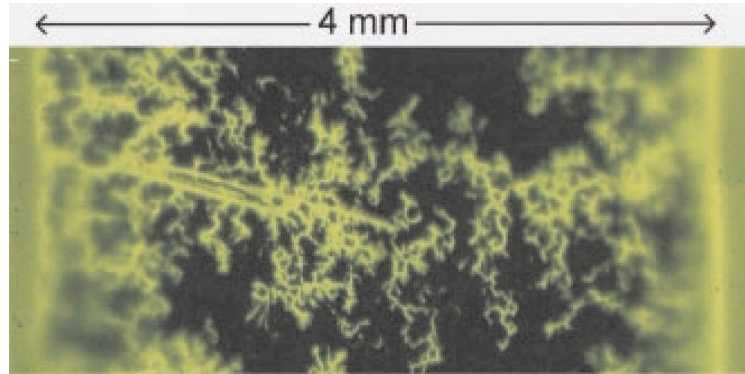
Fig. 4.5: Magneto-optical image taken across the full width of a 4×10 mm YBCO CC at 15 K and 60 mT applied fields. Bright areas indicate magnetic flux penetration, dark areas flux shielding [Fel00].

substrates to obtain J_c values in YBCO CCs that are similar to the ones obtained in single crystalline YBCO films. Fig. 4.5 shows magneto-optical measurements carried out on a YBCO CC sample grown on a RABiTS tape, where the initial penetration of the magnetic field along some high misoriented grain boundaries of the grain boundary network is detected.

As previously commented in section 3.1, Ca doping of grain boundaries increases the effective critical current density of the grain boundary, J_c^{GB}, both for high-angle and for low-angle grain boundaries. Investigations on YBCO CCs also revealed an enhancement of the critical current density at 77 K after Ca doping [Man01, Web03].

Chapter 5

Preparation and characterisation of $YBa_2Cu_3O_{7-\delta}$ coated conductors

In this chapter, the preparation of the YBCO CC samples and the results of the structural and microstructural characterisation are described. YBCO CCs were prepared using the RABiTS approach, depositing the buffer layer system and the YBCO films by pulsed laser deposition. For comparison, YBCO films were prepared in a similar way on single crystalline Ni substrates as reference for the critical current measurements performed on the YBCO CC.

5.1 $YBa_2Cu_3O_{7-\delta}$ coated conductor preparation

5.1.1 RABiTS tapes

Pure Ni (99.98%), Ni-0.1 at.% Mn microalloy, Ni-12 at.% Cr, and Ni-5 at.% W alloys were used as substrates. For the coating process the tapes were cut into pieces of about 1 cm $\times$ 1 cm, and each piece was carefully cleaned in an ultrasonic bath with acetone and isopropanol to remove contaminations of the rolling process. The substrate annealing was carried out *in situ* in a high vacuum (HV) chamber before buffer layer deposition, except for the Ni-Cr and Ni-W alloys that were annealed separately in a tubular furnace at 900°C and 1000°C, respectively. The other substrates (Pure Ni and Ni-Mn) were recrystallised in the HV chamber in forming gas (7% H_2 in Ar) at a partial pressure of 10^{-2} mbar for 30 minutes at temperatures of 700°C and 850°C, respectively. The different annealing temperatures of the tapes are related to the concentration of substitutional elements present in the alloy. Highly alloyed tapes require higher recrystallisation temperatures due to the reduced mobility of the atoms.

The NiCr tape was coated with a 200 nm thick Ni film grown epitaxially by e-beam

evaporation at 500°C, in order to avoid formation of Cr oxides at the surface of the tape during the subsequent buffer layers and film deposition.

5.1.2   Pulsed laser deposition of buffer and YBa$_2$Cu$_3$O$_{7-\delta}$ layers

Buffer and YBCO layers were prepared by pulsed laser deposition, utilising a KrF excimer laser (Lambda-Physik LPX305i) that operates in the ultraviolet spectral region at a wavelength of λ = 248 nm. The maximum pulse energy of this laser is 1.3 J, which corresponds to a mean power per pulse of approximately 30 MW. The maximum repetition frequency is 50 Hz and the pulse duration is approximately 50 ns.

In order to obtain high quality films, a constant deposition rate is required. This can be obtained by imaging the laser beam onto a small area of the target material (approx. 0.1 cm^2) via a quartz lens. A homogeneous energy density distribution across the laser spot is achieved by the use of a quadratic aperture placed before the lens. During the pulse, a high energy is transferred to this small area of the target which heats up in a very short time to high temperatures and evaporates forming a plasma plume. The plasma, which contains thermally emitted ions, electrons, neutral atoms and molecules in a vapour phase, propagates in a direction perpendicular to the target surface. The typical plasma temperature during initial expansion measured by emission spectroscopy is approximately 10000 K [Auc88]. The interaction of the laser beam with the target material is affected by a number of parameters like the absorption coefficient and the reflectivity of the target material, the pulse duration, and the energy of the laser beam.

The chamber was equipped with a turbo molecular pump, a gas-flow system with two different gas channels, and a butterfly valve that was connected to a vacuum gauge to control the gas flow into the chamber. For the preparation of the buffer and YBCO films, three ceramic targets were used: CeO$_2$, yttria-stabilized zirconia (YSZ), and YBCO. In order to obtain an uniform target erosion and consumption, the targets were rotated and wobbled simultaneously during the deposition process. PLD deposition was carried out in on-axis geometry, i.e., the substrate surface is positioned parallel to the target surface (see Fig. 5.1). The quality of the growing film is controlled by several parameters: laser energy density on the target, frequency of the laser pulses, substrate temperature, and gas pressure in the chamber during deposition.

Buffer layer deposition

The buffer layer system of the YBCO CC was composed of a thin layer of CeO$_2$ (50 nm) grown directly onto the RABiTS tape, and a thick layer of YSZ (600 nm). For
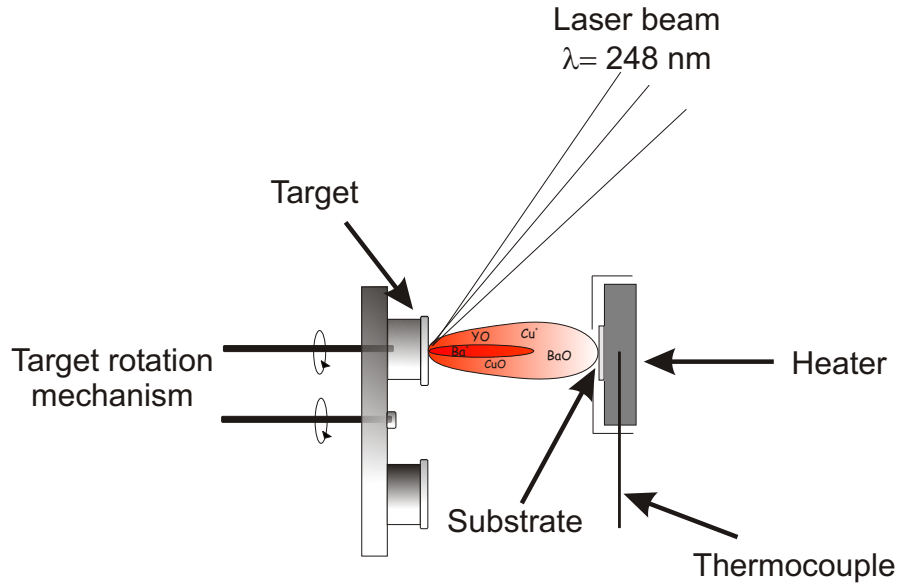
Fig. 5.1: Pulsed laser deposition geometry in on-axis configuration.

the growth of CeO$_2$ and YSZ the energy density of the laser was set to 1.3 J/cm^2 with a pulse frequency of 3 Hz, while the substrate was held at 700°C. The distance between target and substrate was 6.5 cm. The CeO$_2$ layer was grown in a forming gas atmosphere of 2×10^{-2} mbar at a deposition rate of 1 nm/pulse. CeO$_2$ was deposited directly onto the RABiTS tape taking advantage of its ability to grow without the requirement of oxygen gas flow into the chamber, which could oxidise the surface of the RABiTS tape. YSZ was deposited at a rate of 0.7 nm /pulse under a controlled oxygen partial pressure. In order to avoid a strong oxygen diffusion through the buffer layers when the YSZ was not thick enough to prevent it, the oxygen partial pressure was slowly increased during deposition from 1×10^{-4} mbar to 5×10^{-3} mbar.

YBCO film deposition

The pulsed laser deposition of the YBCO film was carried out in an oxygen atmosphere at a pressure of 0.3 mbar and a substrate temperature of 770°C, positioning the target and substrate at a distance of 6.9 cm. The laser pulse frequency was 5 Hz and the energy density 2 J/cm^2. These parameters produced a YBCO deposition rate of 1 nm/pulse, being the YBCO film thickness of 200 nm. After the

Tab. 5.1: Structure and lattice parameters of Ni, CeO$_2$, YSZ, and YBCO.

Material	Structure	lattice parameter (Å)
Ni	cubic, fcc	3.50
CeO$_2$	cubic, CaF$_2$ structure	5.41
YSZ	cubic, CaF$_2$ structure	5.14
YBCO	orthorhombic	a = 3.82, b = 3.88, c = 11.68

deposition, the sample was cooled to room temperature at a rate of 15 K/min in an oxygen partial pressure of 400 mbar. The cooling process at high oxygen partial pressure is crucial for obtaining superconducting YBCO films. Immediately after the deposition, YBCO possesses a tetragonal structure, which is the stable phase at high temperature. The cooling process in a high oxygen partial pressure ensures the transition from the tetragonal to the orthorhombic phase that takes place at 700°C. At this temperature the Cu-O chains are formed.

One of the most critical parameters for the YBCO deposition is the substrate temperature, which may affect the orientation of the YBCO film. For YBCO a *c*-axis orientation is required, which means that the CuO$_2$ planes of the different YBCO grains are parallel to the substrate, and hence parallel to each other. Frequently, if the deposition temperature is too low, YBCO shows an *a*-axis growth with the *c*-axis parallel to the substrate surface. Such an *a*-axis growth strongly affects the superconducting properties, especially the critical current density. The optimal substrate temperature for YBCO deposition was found here to be 770°C, leading to a T_c of approximately 90 K and a transition width of about 1 K.

Epitaxial growth of the films

Table 5.1 compares the structure and lattice parameters of the materials used in the YBCO CC. The difference in the lattice parameter between Ni and CeO$_2$ is evident but does not affect the epitaxial growth, since CeO$_2$ grows rotated by 45° with respect to Ni to adjust the lattices [see Fig. 5.2 (a)]. In this situation the lattice parameter of CeO$_2$ matches to the diagonal of the unit cell of Ni (4.94 Å), achieving a lattice mismatch of 9% [1]. YSZ grows cube-on-cube on CeO$_2$, due to the similarity of the lattice parameters, and YBCO grows rotated by 45° on YSZ, as shown in Fig. 5.2 (b).

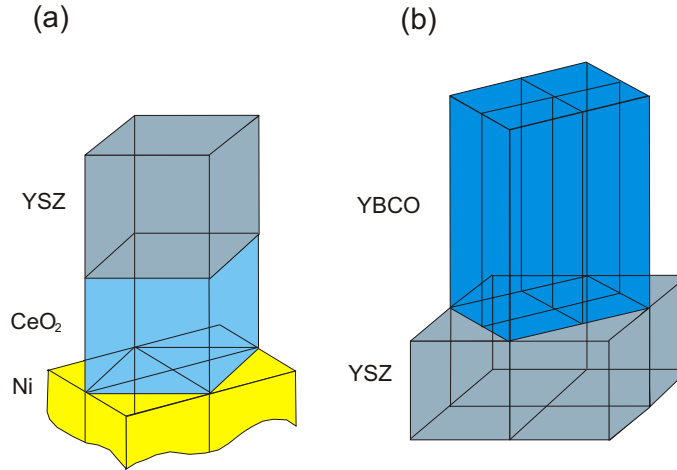[1]The lattice mismatch between substrate and film was calculated as $(a_{substrate} - a_{film})/a_{film}$.

(a) (b)

Fig. 5.2: Schematic representation of the epitaxial growth of (a) CeO$_2$ and YSZ on Ni, and (b) YBCO on YSZ. The unit cell of CeO$_2$ is rotated by 45° with respect to Ni, while YSZ grows cube-on-cube on CeO$_2$. YBCO grows rotated by 45° with respect to YSZ.

5.2 Preparation of YBa$_2$Cu$_3$O$_{7-\delta}$ films on single crystalline Ni substrates

Single crystalline Ni films were grown epitaxially onto SrTiO$_3$ (100) single crystals using e-beam evaporation at a substrate temperature of 500°C under vacuum (10^{-5} mbar) conditions. The Ni films were 200 nm thick and revealed a perfect epitaxial growth with (100) orientation. The buffer and the YBCO layers on the single crystalline Ni films were prepared exactly as in the case of RABiTS tapes. The critical currents obtained for these samples were used as a reference to estimate the limitation of the critical current by the grain boundary network in the coated conductors.

5.3 Structural characterisation techniques

5.3.1 Texture measurements

The texture of the films were analysed using x-ray diffraction (XRD) and electron back scatter diffraction (EBSD). XRD techniques were used to investigate the macrotexture, i.e., the averaged orientation data from the bulk of the sample. On the other hand, EBSD was used to study the microtexture (local orientation) of the samples.
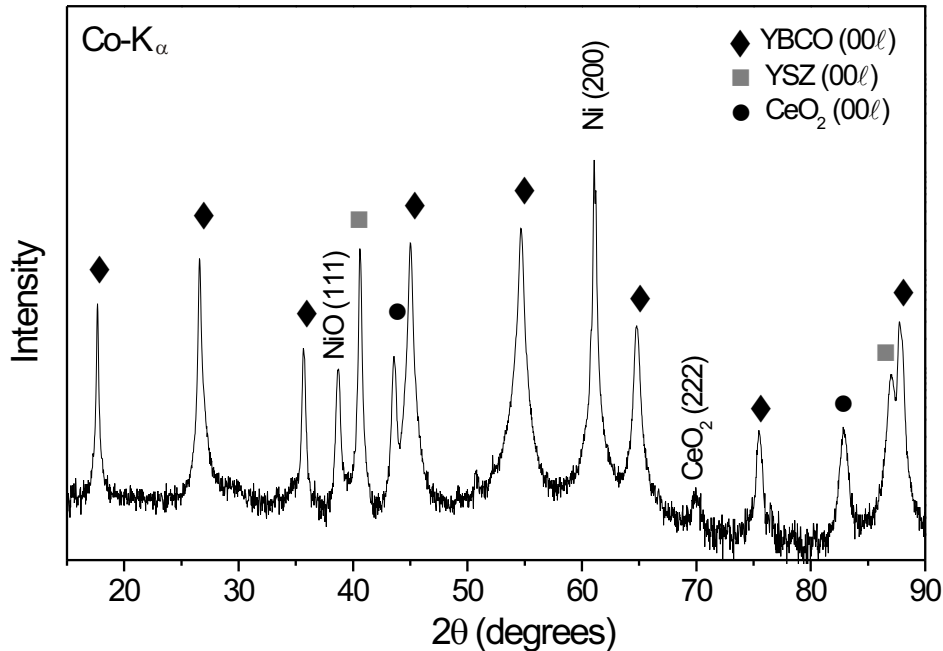
Fig. 5.3: XRD pattern in Bragg-Brentano geometry of the YBCO CC grown on a RABiTS tape. (00*l*) diffraction peaks corresponding to the buffer layer (CeO$_2$ and YSZ) and to the YBCO film are visible. Additionally, the (200) diffraction peak of the RABiTS tape, the (111) diffraction peak of NiO and a small contribution of CeO$_2$(222) are present.

Figure 5.3 shows a typical θ-2θ XRD pattern in Bragg-Brentano geometry for a YBCO coated conductor grown on a RABiTS tape. The 2θ angle of each diffraction peak of the XRD pattern is characteristic of the interplanar distance *d* in the material, and can be used to determine the layer and orientation. The metal substrate and the oxide layers, including YBCO, show diffraction peaks corresponding to (00*l*) planes. This demonstrates the predominant *c*-axis orientation of the layers in the CC. Additionally, small fractions of CeO$_2$(222) and NiO(111) diffraction peaks are observed. The growth of NiO (111) was not found to affect the orientation of the buffer layers and YBCO film. XRD measurements of RABiTS tapes coated only with buffer layers did not show NiO(111) diffraction peak. Therefore, NiO formation is thought to be a result of oxygen diffusion through the buffer layers to the Ni tape during YBCO deposition caused by the high temperature and oxygen pressure.

Pole figures were measured to examine the texture of the YBCO CCs. With this
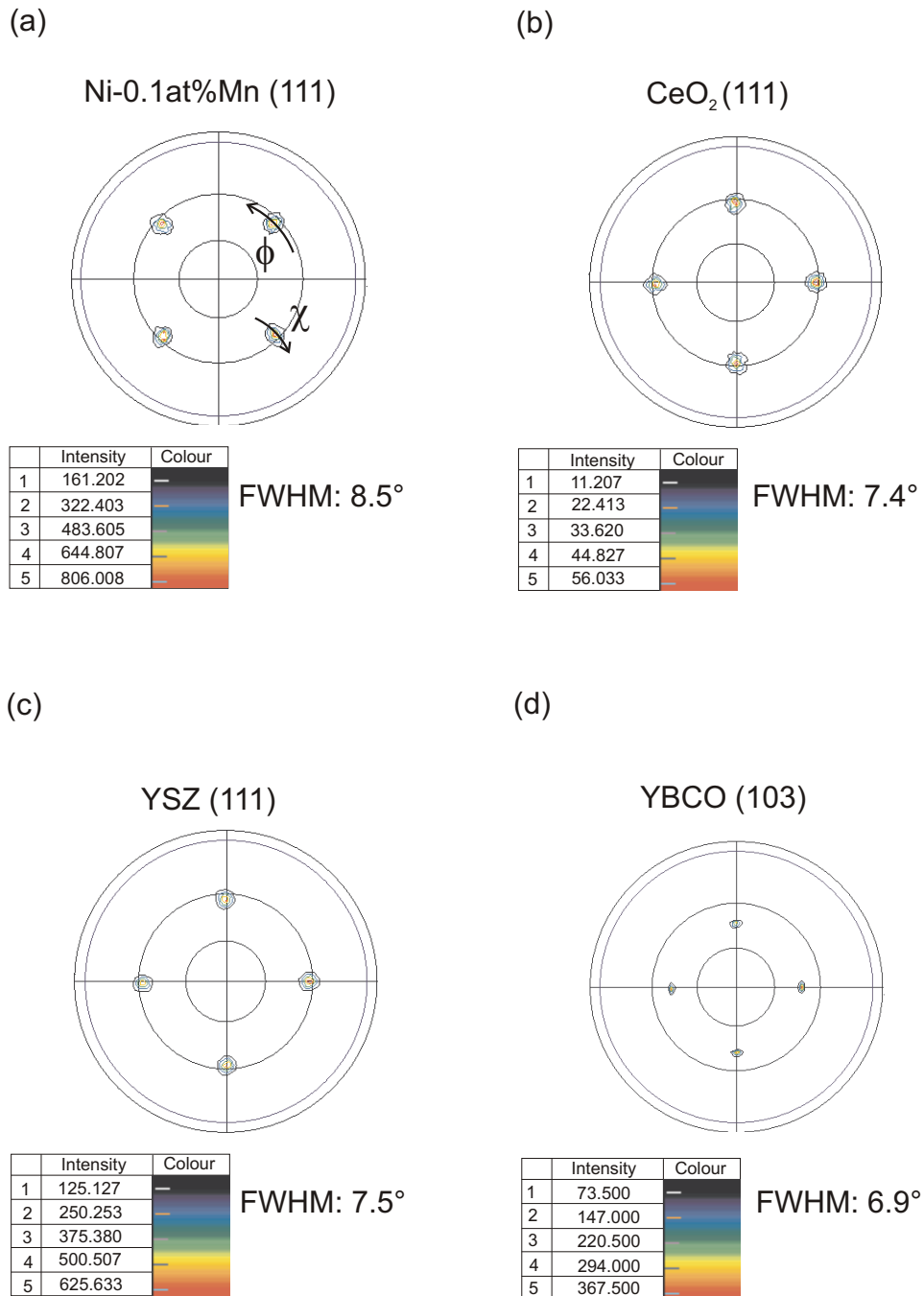
(a)

(b)

Ni-0.1at%Mn (111)

CeO$_2$ (111)

	Intensity	Colour
1	161.202	
2	322.403	
3	483.605	
4	644.807	
5	806.008	

FWHM: 8.5°

	Intensity	Colour
1	11.207	
2	22.413	
3	33.620	
4	44.827	
5	56.033	

FWHM: 7.4°

(c)

(d)

YSZ (111)

YBCO (103)

	Intensity	Colour
1	125.127	
2	250.253	
3	375.380	
4	500.507	
5	625.633	

FWHM: 7.5°

	Intensity	Colour
1	73.500	
2	147.000	
3	220.500	
4	294.000	
5	367.500	

FWHM: 6.9°

Fig. 5.4: (a) (111) pole figure of the RABiTS tape; (b) (111) pole figure of the CeO$_2$ layer; (c) (111) pole figure of the YSZ layer and (d) (103) pole figure of the YBCO film. The FWHM values of the ϕ-scans corresponding to the in-plane texture of each layer are also given.
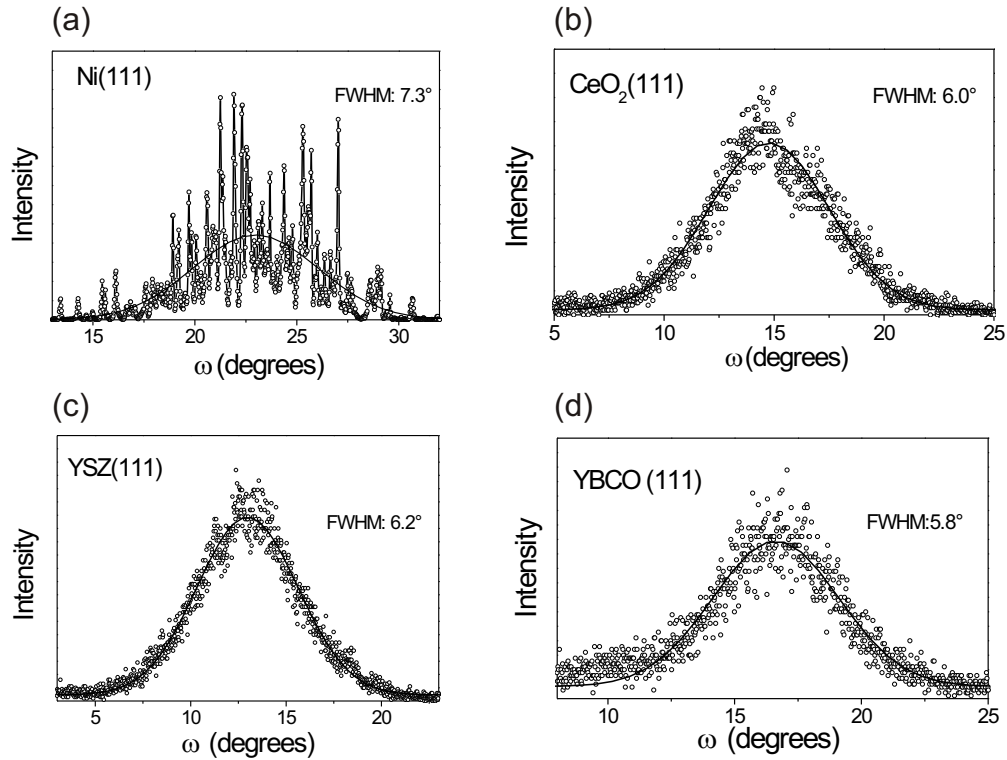
Fig. 5.5: Rocking curves of the different layers present in the YBCO CC: (a) RABiTS tape (Ni-0.1%Mn), (b) CeO$_2$ buffer layer, (c) YSZ buffer layer, and (d) YBCO film.

aim, the detector was set at the appropriate Bragg angle 2θ with respect to the primary beam for diffraction of the desired lattice planes *(hkl)*. The measurement is carried out by rotating and tilting the sample, leading to diffraction if the Bragg law is satisfied. The obtained pole figure gives information about the arrangement of the lattice planes inside the crystal. In the experiment, monochromatic Cu-K$_\alpha$ x-rays with a wavelength $\lambda = 1.5$ Å were used. Figure 5.4 shows the pole figures measured for a Ni-0.1at.%Mn RABiTS tape, the CeO$_2$ and YSZ buffer layers, and the YBCO film. The pole figures of Ni-0.1at.%Mn, CeO$_2$ and YSZ were measured for the (111) planes, and in the case of the YBCO film for the (103) planes. The intensity distribution corresponding to the diffraction at the (111) planes of the Ni, CeO$_2$ and YSZ comprises four maxima that are found in symmetrical positions. In contrast to the substrate, the maxima of the buffer layers are rotated by 45° caused by the epitaxial growth process. The (103) pole figure of YBCO shows also four symmetrical maxima reflections for 45° tilt and 45° rotation angle, due to a rotation by 45° of the (103) planes of YBCO with respect to the expected positions for the (103) planes of YSZ. The full width at half maximum (FWHM) values of
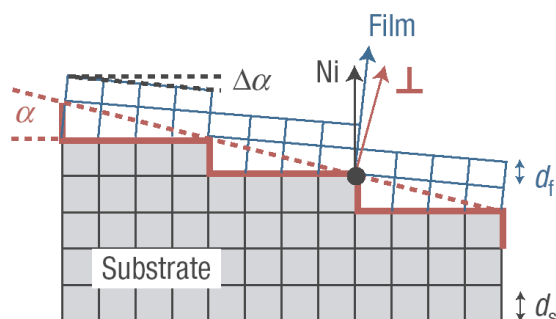
Fig. 5.6: Heteroepitaxial growth mode for CeO_2 on textured RABiTS substrates with crystallographic tilt. α is the local substrate surface miscut angle; $\Delta\alpha$ is the out-of plane tilt angle; d_s is the out-of-plane substrate lattice spacing, d_f is the relaxed film lattice spacing [Bud03].

the maxima in the ϕ direction (direction of rotation) provide information about the quality of the *in-plane* texture of the films. A clear improvement in the *in-plane* texture from the RABiTS tape to the YBCO film is observed (Fig. 5.4).

Rocking curves were measured to detect the degree of *c*-axis misorientation of each layer and to quantify the *out-of-plane* texture. The information obtained measuring rocking curves is equivalent to that obtained from the polefigures in χ direction (direction of tilt). For better comparison between the layers, rocking curves were measured for the (111) planes of all layers (see Fig. 5.5). An improvement in the out-of-plane texture is observed from the Ni substrate with a FWHM of 7.3° to the CeO_2 layer with a FWHM of 6.0°, while for YSZ the value of FWHM is slightly larger (FWHM: 6.2°) than for CeO_2. The YBCO film reveals also an enhancement in the *out-of-plane* texture respect to the YSZ layer, showing a FWHM value of 5.8°. X-ray ϕ and ω scans reveal a strong improvement in both in-plane and out-of-plane texture in the CeO_2 film with respect to the RABiTS tape, which is in agreement with an EBSD analysis recently published [Sar03b]. Budai *et al.* [Bud03] explained the improvement in the out-of-plane texture of the CeO_2 film as a result of the heteroepitaxial growth of CeO_2 on out-of-plane misoriented RABiTS grains. Such RABiTS grains show a vicinal surface with steps that CeO_2 tries to adjust. During the initial stages, CeO_2 is strained in the direction perpendicular to the surface to adjust the out-of-plane substrate lattice spacing, but is free to relax in the surface direction (see Fig. 5.6). This results in a tilt of the *c*-axis of the CeO_2 film toward the surface normal, leading to an improvement of the out-of plane texture in comparison to the substrate. The improvement in the out-of-plane texture of YBCO, however, could be explained considering that YBCO has a layered structure with a preferential lateral growth, i.e, the rapid growth direction is per-
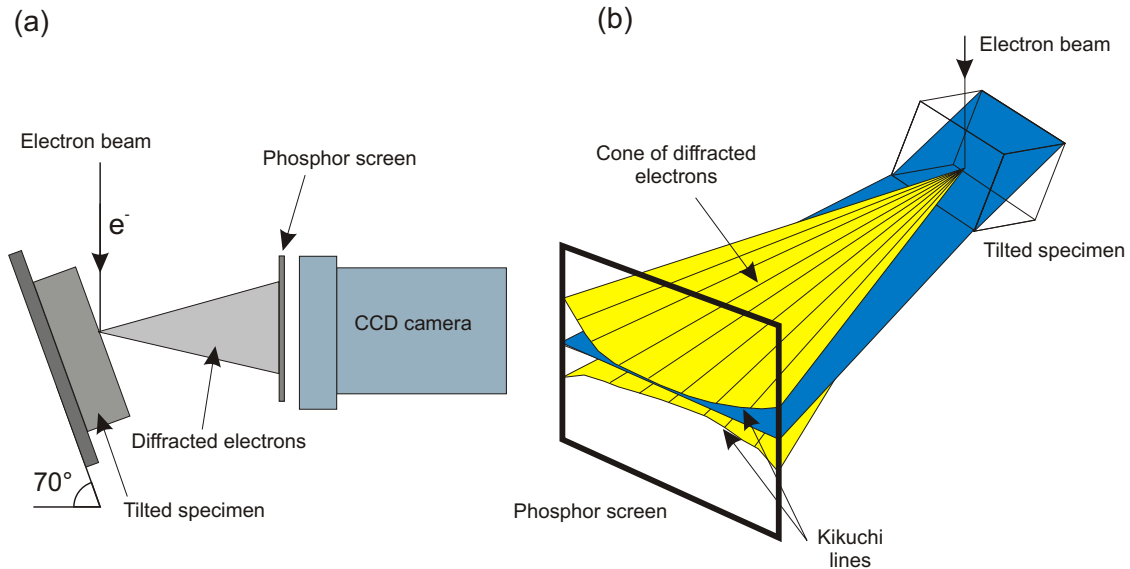
Fig. 5.7: (a) Geometry of an EBSD measurement; (b) schematic representation for Kikuchi lines determination.

pendicular to the c-axis [Cha94, Low97]. If a cluster with the $a - b$ planes lying parallel to the substrate surface nucleates, numerous sites for further lateral growth at the edges of the cluster exist. On the other hand, clusters that grow with the $a - b$ planes out-of-plane misoriented have parallel to the substrate surface a slower growth. This results in a dominant growth of YBCO with the $a - b$ planes parallel to the substrate surface, which consequently improves the out-of-plane texture of the YBCO film.

EBSD was used to investigate the local texture of the YBCO CC. The measured EBSD pattern is composed of many Kikuchi bands that result from electron diffraction in the first 10 - 50 nm of the sample. For this analysis the specimen must be tilted to a relatively large angle (typically 70°) inside a scanning electron microscope (SEM) [see Fig. 5.7 (a)]. This geometry enhances the yield of backscattered electrons. During EBSD measurements, initial inelastic scattering of the incident beam causes the electrons to diverge from an area below the specimen surface and to impinge upon the crystal planes in all directions, producing cones of diffracted electrons when the Bragg condition for diffraction is satisfied by a family of atomic lattice planes [see Fig. 5.7 (b)]. These cones can be imaged using a phosphor screen and a CCD camera. When the cones of electrons intersect with the phosphor screen, they appear as Kikuchi bands, that correspond to a family of crystal lattice planes. EBSD software automatically locates the positions of individual Kikuchi bands and compares them to theoretical data about the specimen. This informa-
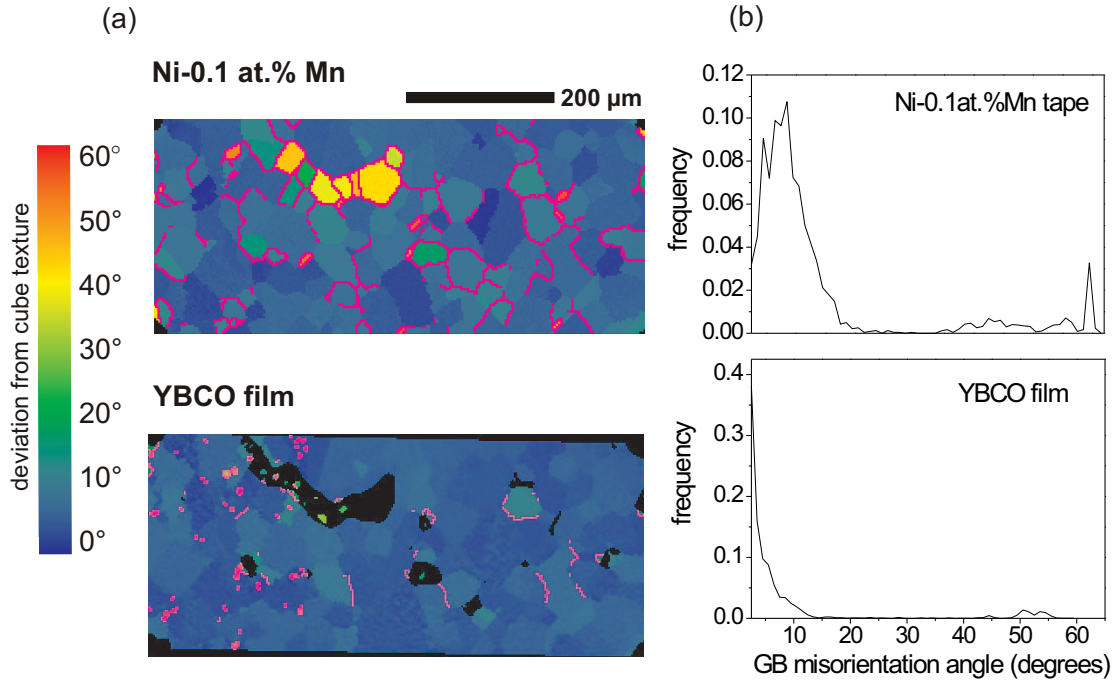
Fig. 5.8: (a) EBSD measurements of a RABiTS tape and a YBCO film carried out for a CC before and after coating [Sch00]. Grain boundaries with misorientation angles larger than 10° are represented as pink lines. (b) Frequency of the grain boundary misorientation angles found in the RABiTS tapes and the YBCO film.

tion can be used to reconstruct the local texture, creating a texture map.

The Kikuchi lines measured for the RABiTS tape are typically sharp and easy to identify compared to those measured on the YBCO films, which are weaker and not so well defined due to various reasons: (i) YBCO is a ceramic material with low conductivity that produces charging effects, leading to a reduction of the number of backscattered electrons, (ii) YBCO films have internal stresses due to the epitaxial growth, and (iii) the small grain size of YBCO is close to the resolution limit of the microscope (200 - 500 nm). All these features make difficult the determination of the orientation mapping of the YBCO film.

Figure 5.8 (a) shows EBSD measurements corresponding to a Ni-0.1%Mn tape and to the YBCO film grown on this substrate. Both EBSD measurements were carried out on the same area of the sample, before and after coating [Sch00, Hol01b]. The EBSD patterns are represented with a colour scale that indicates the three-dimensional misorientation of each grain with respect to the ideal cube texture. The EBSD measurements on YBCO were carried out with the approximation that the YBCO structure is a perovskite composed of 3 cubes, so that $c = 3a$. Under

this assumption, it is found that YBCO does not grow epitaxially on Ni grains with misorientations above 15° [Sch00, Hol01b]. This is reflected in the black areas that are unindexed regions. Moreover, it is expected that only the out-of-plane texture component of the RABiTS grains affects the epitaxial growth of YBCO on each grain. Therefore, 15° out-of-plane misorientation of the RABiTS substrate is thought to be the limit for the epitaxial growth of YBCO [see Fig. 5.8 (a)].

The pink lines in the EBSD patterns are grain boundaries with misorientation angles higher than 10°. Figure 5.8 (b) shows the frequency of grain boundary misorientation angles in the RABiTS tape and in the YBCO film. The misorientation of the grain boundaries are calculated as the misorientation between neighbouring grains. In the RABiTS tape the grain boundary angles are found to vary between 5° and 20°, with a further presence of twin boundaries at 60°. The grain boundary angles in the YBCO film have only values below 12°. This indicates a clear improvement of the texture in the YBCO film compared to the RABiTS tape that is in agreement with the results obtained by XRD measurements.

5.3.2   Microstructure investigations

Scanning electron microscopy

Scanning electron microscopy (SEM) was used to analyse the surface morphology of the buffer layers before YBCO coating, and of the deposited YBCO films. Figure 5.9 shows SEM pictures corresponding to buffer layers of CeO$_2$ 50 nm thick, and of YSZ 600 nm thick. They disclose a smooth and crack-free appearance, which avoids Ni diffusion into the superconducting film. SEM micrographs of YBCO CCs grown on the former buffer layer of YSZ and CeO$_2$ are shown in

(a)   (b)
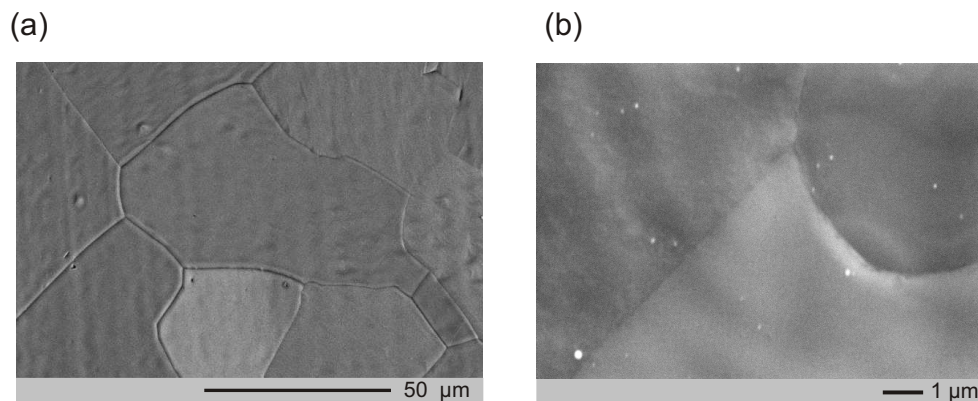

Fig. 5.9: SEM micrographs of epitaxially grown crack-free buffer layer: (a) 50 nm CeO$_2$ layer, (b) 600 nm YSZ buffer layer grown onto the CeO$_2$ layer.
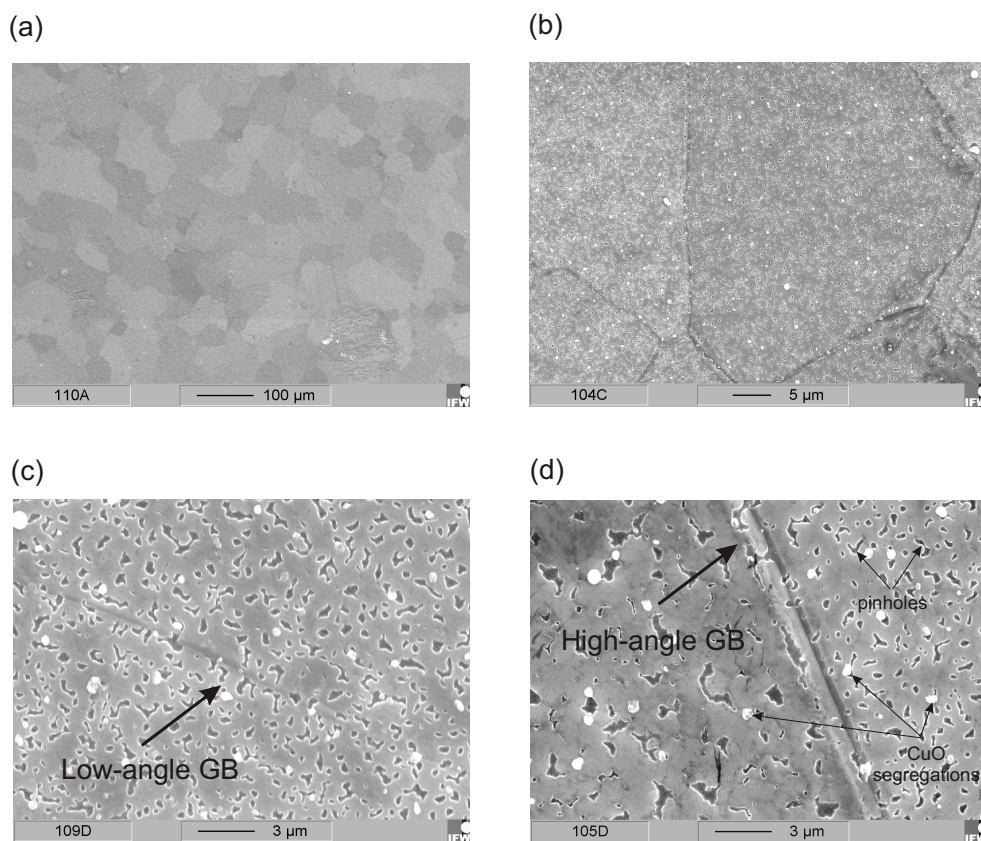
Fig. 5.10: SEM micrographs of a YBCO CC surface in (a) low , and (b) high magnification. The typical grain size of the nickel grains is around 20 - 50 μm; (c) pinholes and CuO segregations around a low-angle grain boundary; (d) High-angle grain boundary with characteristic grooving.

Fig. 5.10, revealing the typical grain structure of the YBCO CC propagated from the RABiTS substrate, with grain sizes on the scale of 20 - 50 μm. However, the small YBCO grains with sizes below 1 μm within the large grains are not observed in these micrographs.

Figures 5.10 (c) and (d) exhibit the surface morphology of the YBCO CCs that reveals the presence of defects like pinholes and CuO segregations with sizes of around 0.5 μm. The pinhole formation in the YBCO films is a result of the three-dimensional island growth mechanism of YBCO (Volmer-Weber mode) [Haw91], and indicates that the small YBCO grains contained within the large grains propagated from the RABiTS substrate are not completely connected. To achieve a smooth surface without pinholes, it would need a layer by layer growth mode that is unlikely in a four-component compound with a very anisotropic unit cell. Figure 5.10 (d) shows a high-angle grain boundary with a strong grooving that

is transferred from the RABiTS tape. The grain on the left is highly misoriented and has much larger pinholes. This is thought to be related to a different nucleation process and growth of buffer and YBCO layers on highly-misoriented RABiTS grains.

Atomic force microscopy

The microstructure of the YBCO CCs was also studied by atomic force microscopy (AFM), which gives further information about the topography of the surface. Figure 5.11 shows AFM micrographs of the YBCO CC that reveal the small size of the YBCO grains (0.2 - 0.3 μm), well below the grain size of the RABiTS tape (20 - 50 μm). The pinholes are found to have an irregular size that varies between 1 and 2 μm. From the AFM analysis across the pinholes it may be concluded that they are as deep as the thickness of the YBCO film. The size of the pinholes detected in Fig. 5.11 (a) corresponds to an optimised YBCO CC with high J$_c$ (above 1 MA/cm^2). If pinholes were not present a clear degradation of the superconducting properties was detected. Due to the relatively large size of the pinholes, pinning is not considered as a possible reason for this improvement. However, it is thought that pinholes can lead to a better oxidation of the YBCO film during deposition and cooling. On the other hand, excessively large pinholes were found to affect negatively the superconducting properties of the film. The CuO segregations on the surface of YBCO have a size of 0.5 - 1 μm, and a height of 200 nm. Figure 5.11
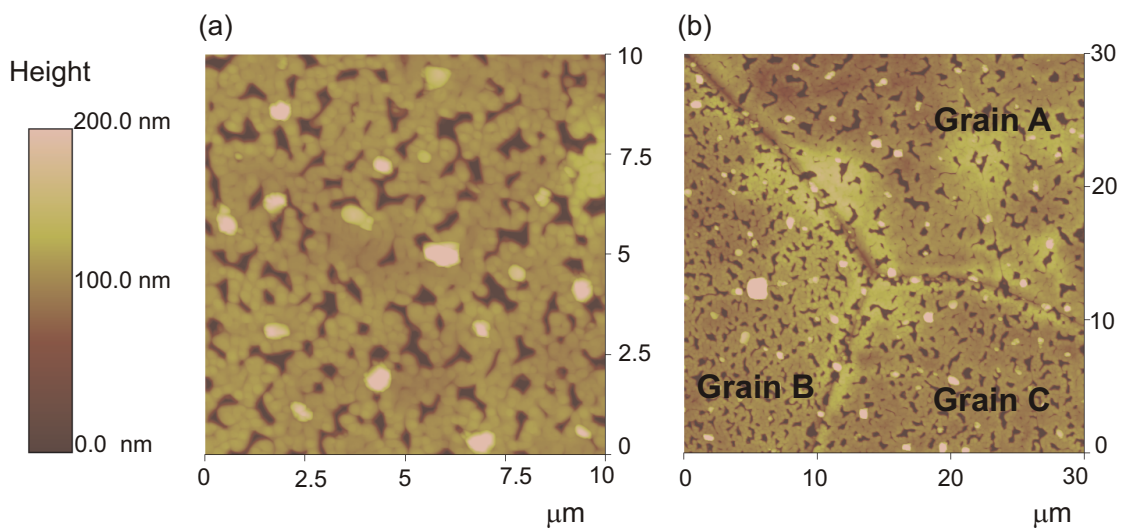

Fig. 5.11: AFM micrographs of a YBCO CC surface: (a) YBCO grains, pinholes, and CuO$_2$ segregations are visible, (b) Grain boundaries of the YBCO CC. Grain A is highly misoriented.

(b) is an AFM micrograph of three different grains propagated from the RABiTS tape. Grain A is identified as a highly-misoriented grain, due to the grooving of the boundaries, exhibiting small YBCO grains and defects (pinholes and CuO segregations) that are slightly larger than in the grains B and C.

Transmission electron microscopy

Transmission electron microscopy (TEM) analysis was carried out on the YBCO CC in order to study its microstructure. The specimen was prepared by the so called "T-Tool" technique, cutting the sample in thin slices with a wire saw, and pasting two of these slices face-to-face (YBCO surface in contact with YBCO surface). The resulting specimen was lapped, and finally polished by ion beam bombardment at an energy of 3.5 keV, and an incident angle between $3°$ - $5°$.

Microstructural characterisation was performed using conventional TEM (JEOL 2000 FX) and high-resolution TEM (HRTEM) (Tecnai F30). Only substrate and buffer layers were analysed, the YBCO film could not be investigated due to technical problems in the specimen preparation. TEM micrographs of the buffer layers and the RABiTS tape evidence the formation of a thin NiO layer at the interface between the RABiTS tape and the CeO_2 film (Fig. 5.12). The thickness of the NiO layer is found to vary from 15 to 28 nm. However, in the case of the CeO_2 film an uniform thickness of around 50 nm is disclosed. Moreover, the columnar grain
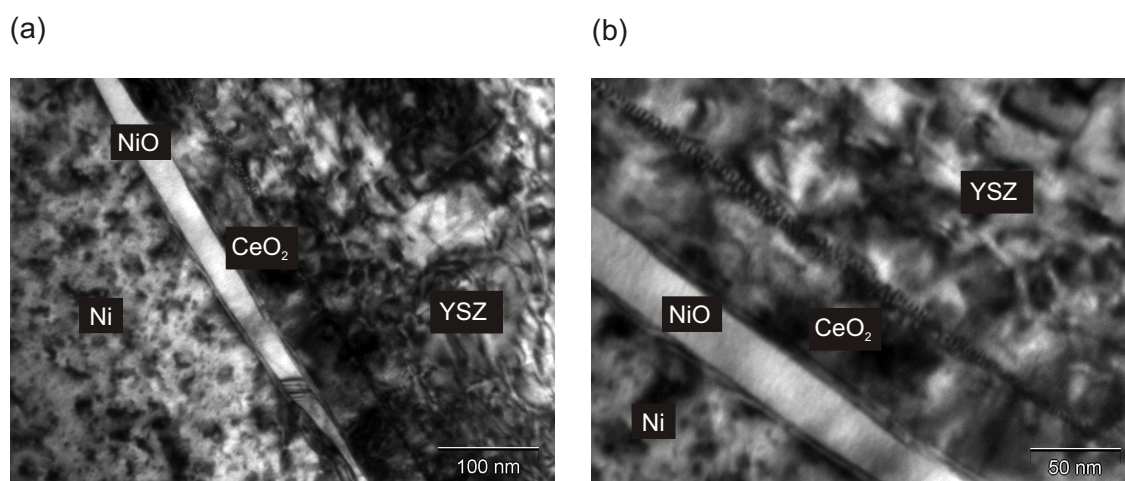
(a) (b)

Fig. 5.12: (a) Cross-section of the YBCO coated conductor. The TEM micrograph shows the inhomogeneously grown NiO layer and the columnar YSZ grains; (b) TEM micrograph with higher magnification showing the Moiré fringes observed at the interface between CeO_2 and YSZ. (TEM preparation and micrographs by C. Mickel, IFW Dresden)
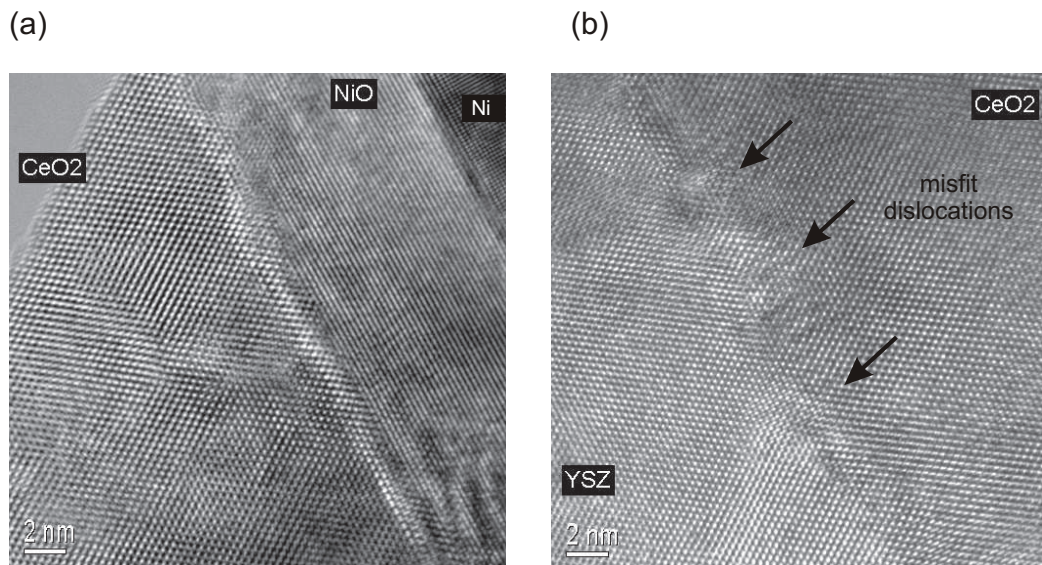
(a)   (b)

Fig. 5.13: HRTEM micrograph of the buffer layers grown on RABiTS. (a) Interface between RABiTS tape and CeO$_2$ layer; (b) Interface between CeO$_2$ and YSZ. Misfit dislocations due to the epitaxial grow are also visible at the interface. (HRTEM micrographs by J. Thomas, IFW Dresden)

structure of YSZ is detected, with a typical grain width of 50 - 100 nm. The interface between CeO$_2$ and YSZ layers is easily distinguished at increased magnifications by the presence of Moiré fringes [Fig. 5.12 (b)], which are an interference effect at the interface of both materials that have a very similar structure, but with slightly different lattice constants.

Detailed examinations of the films with HRTEM revealed the perfectly epitaxial growth of YSZ on CeO$_2$ and the thin layer of NiO formed at the interface between RABiTS tape and CeO$_2$ film (Fig. 5.13). At the interfaces between YSZ and CeO$_2$, misfit dislocations are formed to accommodate the lattice mismatch between the materials [Fig. 5.13 (b)]. Furthermore, the (111) orientation of the NiO layer detected by XRD was confirmed.

Focused ion beam analysis

In order to prepare and analyse a cross-section of the YBCO CC, a focused ion beam (FIB) system working with Ga$^+$ ions was used. With this technique it is possible to remove very precisely the material in the areas of interest, in this case the grain boundaries. The Ga$^+$ ions were accelerated to energies of 30 keV to perform the cross sectioning of the sample. Besides sample preparation, the ion beam can
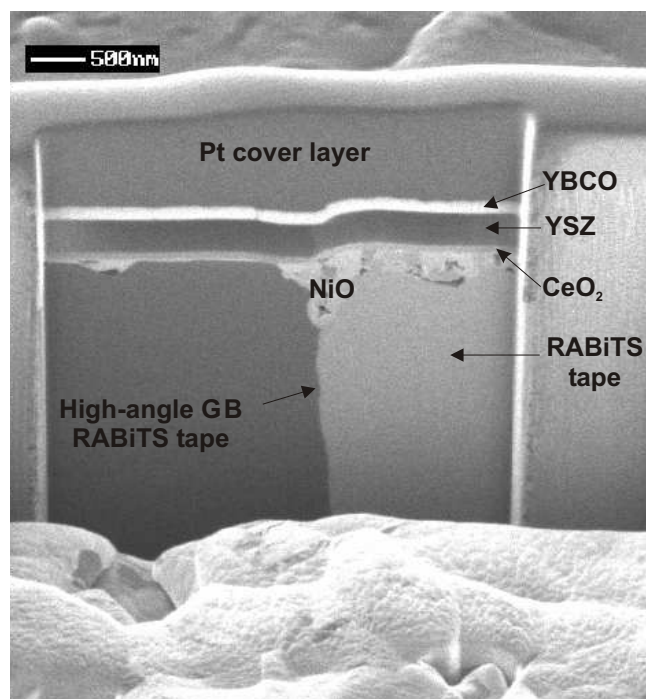
Fig. 5.14: Micrograph of a cross-section of the YBCO CC prepared by FIB. The cut crosses a high-angle grain boundary that is clearly visible in the RABiTS tape. (FIB micrographs by S. Menzel, IFW Dresden)

also be used to image the prepared cross-section with high magnification. The advantage of this technique in comparison to TEM is the possibility to easily select the area for analysis. A FIB micrograph of a cross-section, 4 μm deep, prepared across a high-angle grain boundary of the YBCO CC is shown in Fig. 5.14. The architecture of the YBCO CC is clearly seen: RABiTS substrate, buffer layers, YBCO film and a thick Pt layer that was deposited on the area of analysis to protect the YBCO film during cross section preparation. The high-angle grain boundary of the RABiTS tape is detected in the FIB micrograph due to the different contrast of the RABiTS grains on the left and on the right hand side. FIB reveals the preferred formation of NiO in the high-angle grain boundary due to the easy solid-state diffusion of oxygen through the buffer layers at this area. This explains the relatively strong diffraction peaks of NiO (111) in the XRD measurements (see section 5.3.1) without further effects on the rest of the layers.

Figure 5.15 shows microstructural inhomogeneities found at the surface of the YBCO film prepared on tungsten alloyed Ni substrates (Ni-5at.%W). Such inhomogeneities exhibit the form of "bubbles" with a size between 1 and 10 μm [Fig. 5.15 (a)]. FIB analysis allowed the preparation of a cross-section on one of these "bubbles" to study its structure [Fig. 5.15 (b)]. Inside the "bubbles" there is an empty
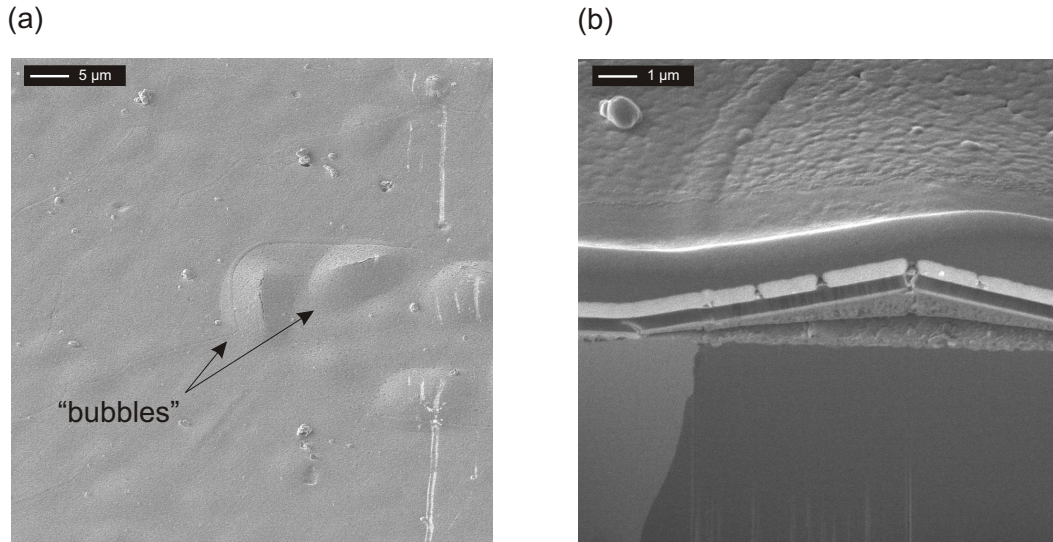
(a)

(b)

Fig. 5.15: (a) FIB micrograph revealing inhomogeneities in the form of "bubbles" formed at the surface of the YBCO CC. (b) Cross-section of the YBCO CC prepared by FIB across a "bubble". The "bubble" is empty; buffer and YBCO films are deformed. (FIB micrographs by S. Menzel, IFW Dresden)

space where the buffer layer system is completely deformed, and without contact to the metal substrate. These defects are formed only during the YBCO deposition, but their mechanism of formation is still unclear. A possible origin for such "bubble" formation could be excess of C and S impurities, which are present in different concentrations in the RABiTS tapes. It is known that C and S segregate to the surface of the RABiTS tape during heating, and that S produces a c(2×2) superstructure, which is found to be necessary for the epitaxial growth of the buffer layers [Can01b]. However, if the concentration of S or C is too high, a reaction with the oxygen that diffuses through the buffer layers (see section 5.3.1) could be expected forming different gases (e.g., SO_2, CO, CO_2). If the partial pressure of the gas becomes very high, a local deformation of the layers would occur. For a definitive conclusion, a deeper analysis of the impurities present in the RABiTS tape has to be performed.

Chapter 6

Electrical transport properties of YBa$_2$Cu$_3$O$_{7-\delta}$ coated conductors

6.1   The superconducting transition

The superconducting transition of the prepared YBCO CCs in zero magnetic field was typically measured by an inductive method, for the determination of the critical temperature T_c of the samples. The principle of the inductive method is based on the generation of an alternating magnetic field by a primary coil and the detection of the response in a secondary coil by a lock-in amplifier. Locating the sample between these two coils, two main scenarios should be distinguished. If the sample is in the superconducting state, producing shielding currents in response to the generated alternating magnetic field, the secondary coil is screened by the superconducting sample and the lock-in amplifier does not detect any signal. If however, the sample is in the non-superconducting state, the alternating magnetic field generated by the primary coil induces an alternating voltage in the secondary coil that is detected by the lock-in amplifier. Figure 6.1 shows the result of an inductive T_c measurement of a YBCO CC. The temperature dependence of the voltage induced in the secondary coil, and its phase with respect to the primary voltage are presented. T_c can be determined at 10%, 50% and 90% of the superconducting transition and is termed T_c^{10}, T_c^{50} and T_c^{90}, respectively. Here, T_c^{90} will be used together with $\Delta T = T_c^{90}$-T_c^{10} as representative values for the superconducting transition.

Typical T_c values measured on the YBCO CCs were between 88.0 K and 90.0 K with a transition width ΔT of approximately 1.0 K. The obtained value of $\Delta T = 1.0$ K indicates a sharp phase transition that is a measure of the quality of the YBCO film. In the case of conventional type II superconductors the superconducting transition width is usually sharper than the ones presented here. This is a consequence of
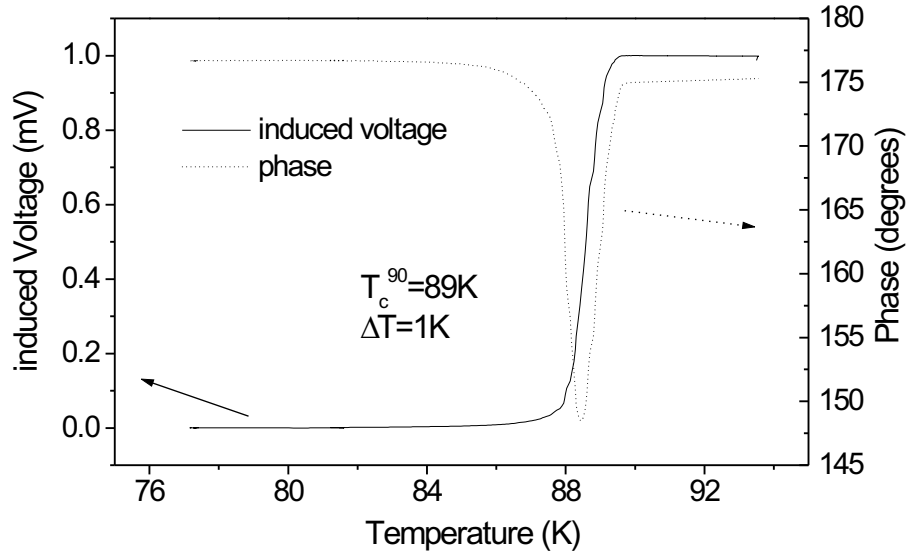
Fig. 6.1: Inductive measurement of T_c of a YBCO CC.

the strong thermally activated flux creep phenomena that occur in HTS materials, becoming especially important at temperatures close to T_c (see section 2.5.2).

Resistive transition measurements were performed in a four-probe geometry at different magnetic fields, which were varied between 0 and 9 T in a Quantum Design "Physical Property Measurement System" (PPMS). During the measurement the applied field was aligned to the c-axis of YBCO and perpendicular to the direction of current flow. The results of such measurements are shown in Fig. 6.2. The $R(T)$ curves of the YBCO CC reveal a broadening of the resistive transition from $\Delta T = 0.7$ K to $\Delta T = 4.5$ K, and a successive reduction of T_c from 89.0 K in zero field to 79.6 K when the applied magnetic field is increased to 9 T. The reduction in T_c and increase of the transition width ΔT is directly related to flux creep effects that become even more important in the presence of applied magnetic fields. Nevertheless, the broadening in the resistive transition of YBCO is not very pronounced compared to that in highly anisotropic HTS compounds like the BSCCO family. As a consequence of their large anisotropy these materials have much lower pinning energies than the "isotropic" YBCO, showing stronger flux creep effects and consequently broader resistive transitions [Pal91].

YBCO CC samples were coated with silver immediately after deposition to protect the YBCO film from humidity and to avoid degradation of the superconducting properties. Therefore, the silver film was present during all the resistance measurements, hindering the determination of the resistivity of the YBCO film in the non-superconducting state between 89 K and 300 K, where the measured resistance is mainly determined by the Ag film.
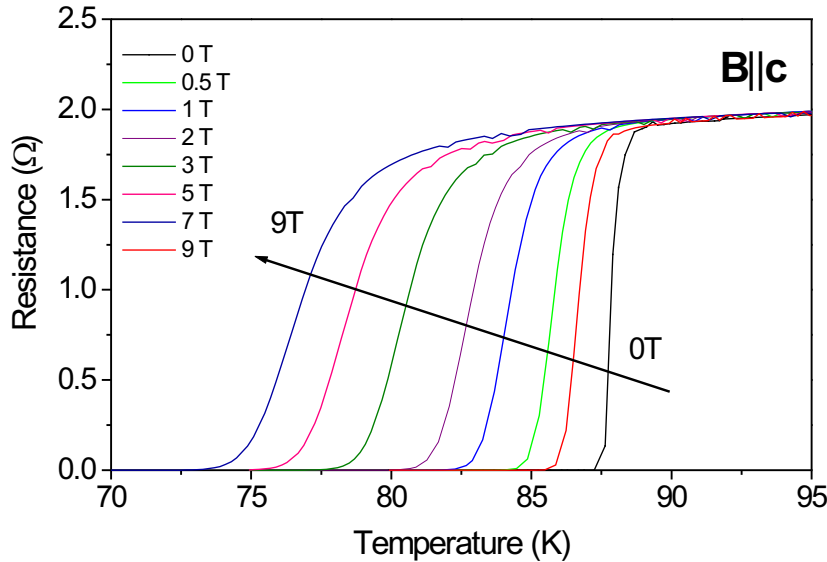
Fig. 6.2: Resistive superconducting transition measured at different applied magnetic fields between 0 and 9 T.

Bridges with lengths of 800 μm and widths of 300 μm were patterned on the samples. The width of the bridges is an important point that has to be taken into account due to the relatively large grain size of the RABiTS tapes that varies between 20 - 50 μm. The bridge must be wide enough to include several grains in order to obtain a result that is representative of the whole YBCO CC. Moreover, using wider bridges reduces the likelihood that some high-angle grain boundaries block the current in the bridge.

The bridges on the YBCO CCs were patterned by photolithography. For this purpose, the YBCO film was covered with a thin film of photoresist and subsequently exposed to UV light illuminating the sample through a negative mask of the contact pad pattern, obtaining in this way the positive structure of the mask on the sample. The final etching process that is necessary to remove the unmasked YBCO film was carried out utilising different techniques: wet chemical etching or ion etching. The wet chemical etching consists of removing the unmasked YBCO film by dilute H_3PO_4, while the covered YBCO film is protected by the photoresist mask. A disadvantage of this method is that the dilute acid can undercut the photoresist leading to a patterned bridge with unknown dimensions. Especially, the GBs of the YBCO CC can be etched more strongly than the grains, since GBs are more sensitive to the etchant. This problem is solved by ion etching, where the uncovered YBCO film is removed by Ar^+ ion bombardment, while the photoresist protects the covered YBCO film.

6.2   Voltage-current characteristics

Voltage-current density $(V - J)$ measurements were carried out on patterned samples using a four-probe geometry. The $V - J$ measurements were performed in a 9 T PPMS at different temperatures and applied magnetic fields. The aim of these measurements was the determination of the critical current density J_c, and of the
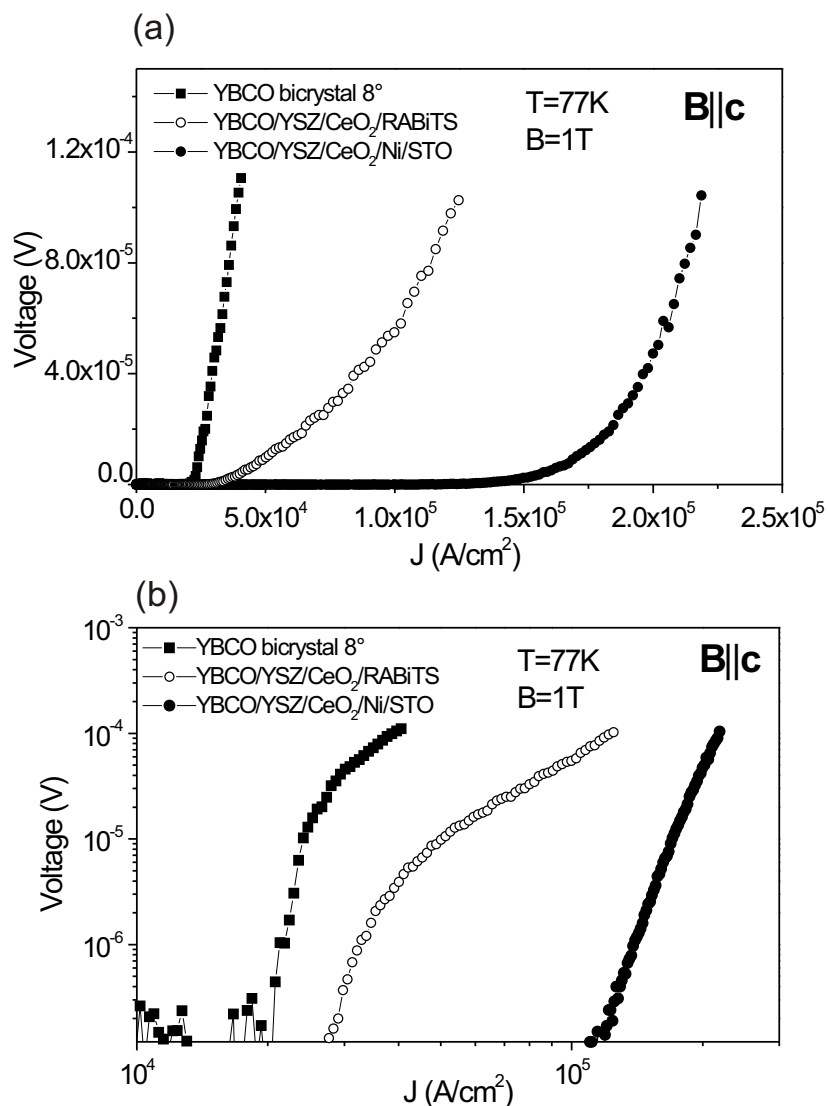

Fig. 6.3: $V - J$ characteristics of a YBCO CC, a YBCO bicrystal with an 8° [001] tilt grain boundary, and a YBCO film grown on a single-crystalline Ni film on SrTiO$_3$ (100) (STO), all of them measured at 77 K and 1 T applied magnetic field. (a) Linear representation of the $V - J$ characteristics; (b) double logarithmic representation of the $V - J$ characteristics.
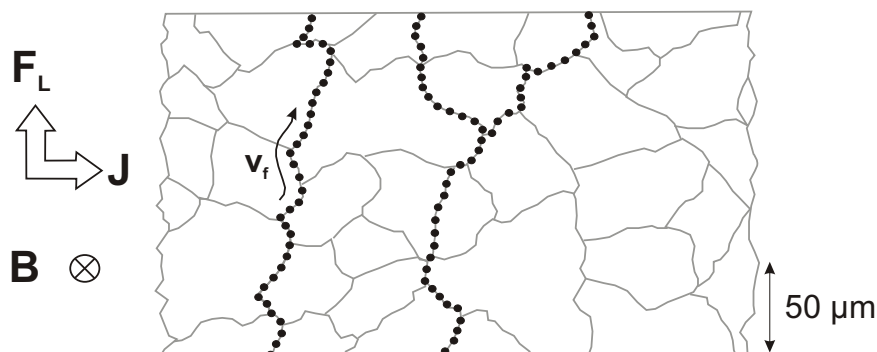
Fig. 6.4: Schematic representation of a YBCO CC. Vortex flow channels are made up of low-angle grain boundary segments with different J_c values. The applied magnetic field is normal to the conductor plane [Eve99].

effects that the sample granularity has on the transport current.

Figure 6.3 shows the $V - J$ curves of a YBCO CC, a YBCO bicrystal with an $8°$ [001] tilt grain boundary and a YBCO film grown on a single crystalline Ni film on SrTiO$_3$ (100), measured at 77 K and 1 T applied magnetic field.

The results for the bicrystal indicate a linear $V - J$ characteristic typical for low-angle grain boundaries. The linearity is produced by a viscous flow of the flux lines along the grain boundary (see section 3.2.1), and is termed non-ohmic linear differential (NOLD) behaviour [Ver00]. This contrasts to the $V - J$ curves of the YBCO film grown on a single crystalline Ni substrate that present a different behaviour. The YBCO CC reveals a $V - J$ characteristic that can not be described by a perfect NOLD behaviour. This is caused by the contribution of a large number of grain boundaries that are present in the YBCO grain boundary network (GBN) with many different misorientation angles. Similar to the bicrystal, viscous flux flow takes place along the grain boundaries of the YBCO GBN, but in a more complex form due to the percolative current flow and viscous flux flow through multiple channels of the GBN [Eve99] (see Fig. 6.4). The nearly NOLD behaviour of the $V - J$ characteristic in the YBCO CC is more evident in the double logarithmic representation [see Fig. 6.3 (b)]. Such a characteristic of both the YBCO bicrystal and YBCO CC is a sign that the limitation of the transport current is caused by grain boundaries in contrast to the single-crystalline YBCO film.

6.2.1 $V - J$ characteristics with $\vec{B}||\vec{c}$

The $V - J$ characteristics of the YBCO CCs were measured at different temperatures and magnetic fields varied from 0 to 9 T. The same layer system (YBCO/YSZ/ CeO$_2$) grown on a single-crystalline Ni film (without grain boundaries) was taken

as a reference system. The $V - J$ curves measured on this sample at different temperatures are shown in Fig. 6.5. They reveal a slight curvature change between low and high applied magnetic fields and voltages. This behaviour is similar to the $V - J$ curves measured by Koch *et al.* [Koc89], who identified this as a glass-liquid transition (see section 2.6). The measured $V - J$ curves show that at high magnetic fields and low currents (or voltages) a linear (ohmic) behaviour is detected, indicating that the irreversibility field of the YBCO film is reached, while for higher currents, the $V - J$ curves disclose a positive curvature. At lower magnetic fields, a power law behaviour is found at high voltages, while for low voltages a slight negative curvature is detected. Between high and low magnetic fields, the $V - J$ characteristics reveal a pure power law behaviour at low and high voltages without any sign of ohmic resistance. Considering the vortex glass model, the pure power law behaviour should indicate the transition from vortex glass (at low magnetic fields) to vortex liquid phase (at high magnetic fields).
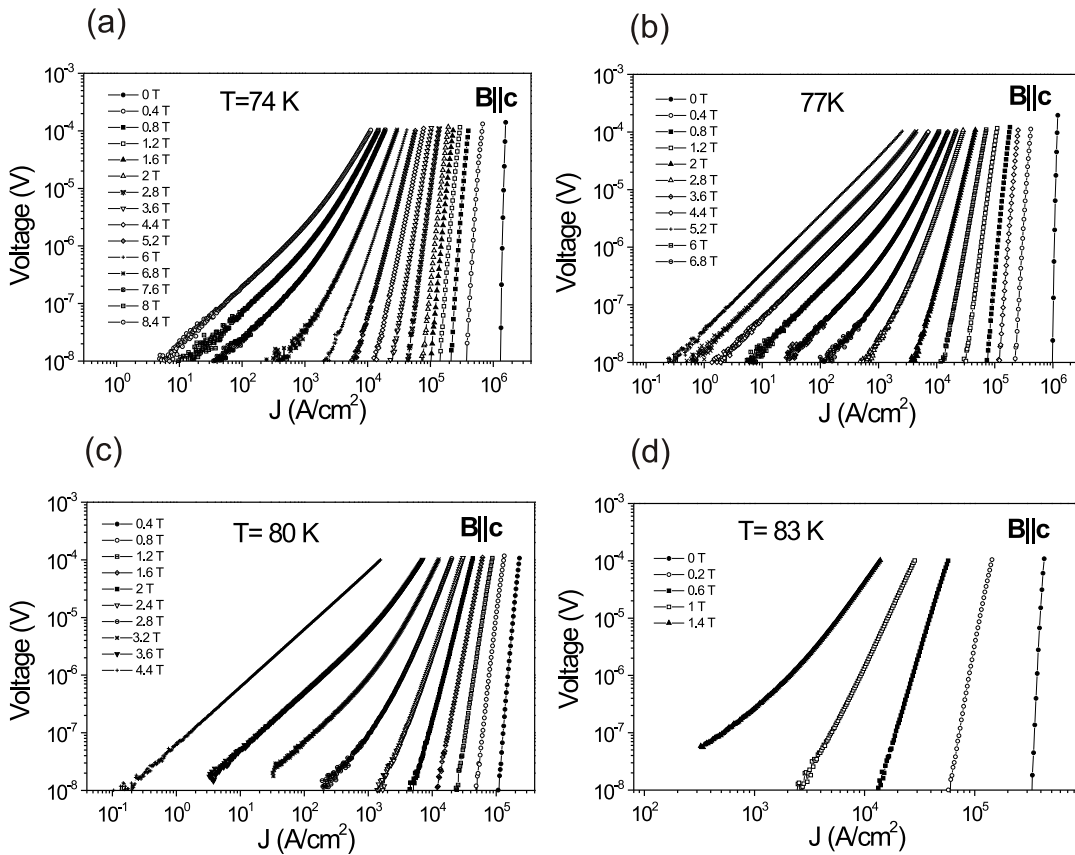

Fig. 6.5: Magnetic field dependence of $V - J$ curves for the YBCO film grown on YSZ/CeO$_2$/Ni/SrTiO$_3$ at (a) 74 K, (b) 77 K, (c) 80 K, and (d) 83 K.

Alternatively, the phenomenological model of Zeldov introduced in section 2.5.2 can be used to explain the pure power law behaviour found in the $V - J$ characteristics as an indication of flux creep limitation, however the model can not explain the behaviour found at low and high applied magnetic fields.

The $V - J$ curves measured for the YBCO CC are presented in Fig. 6.6. At low temperatures (20 K and 60 K) the curves present a NOLD behaviour over the full range of accessible fields, resulting from viscous flux flow along low-angle grain boundaries [Día98b]. At higher temperatures (77 K and 83 K) the $V - J$ characteristics reveal a change in curvature as the magnetic field increases. This change takes place at a field known as the crossover magnetic field B^{cr} already introduced in section 3.2.2, that indicates a transition from J_c limitation by grain boundaries to J_c limitation by flux creep mechanism. Consequently, for applied magnetic fields below B^{cr} the $V - J$ curves present the expected NOLD-like signature, and for applied magnetic fields above B^{cr} a power law behaviour is observed. The irreversibility field is reached at higher magnetic fields.
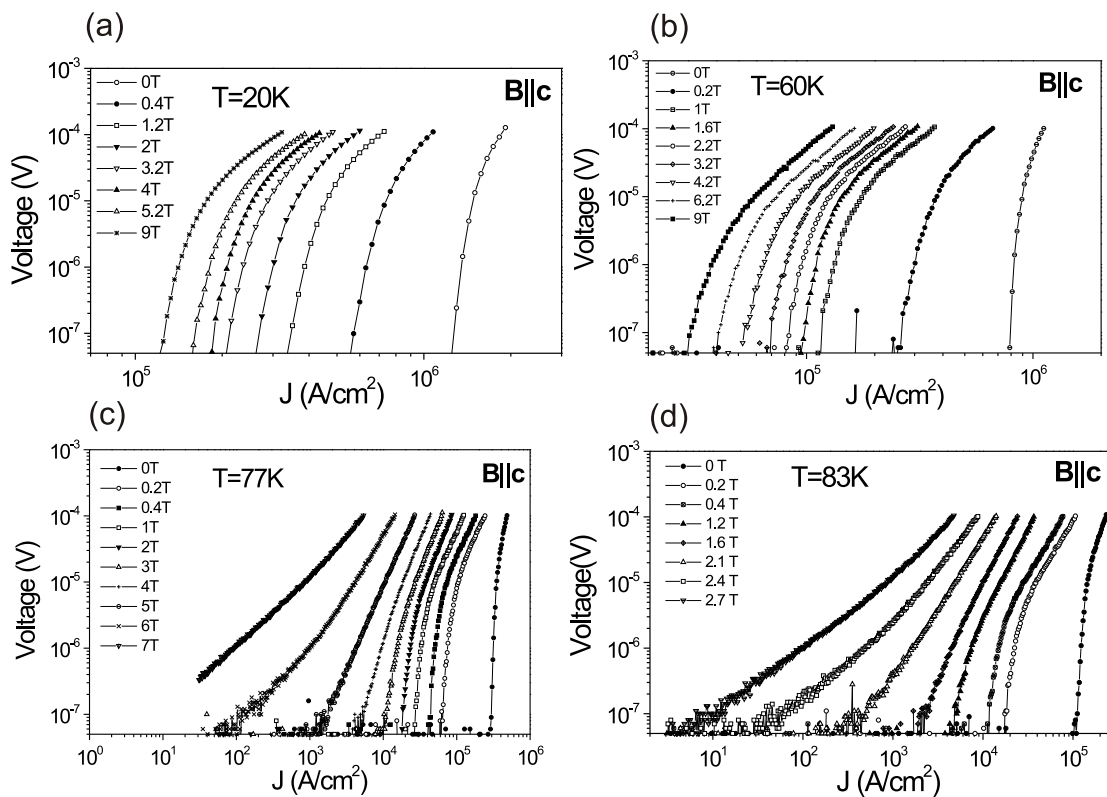

Fig. 6.6: Magnetic field dependence of $V - J$ curves for a YBCO CC, at (a) 20 K, (b) 60 K, (c) 77 K, and (d) 83 K.

6.2.2 $V - J$ **characteristics with** $\vec{B}||\vec{ab}$

In the case that the magnetic field is applied parallel to the $a - b$ plane of YBCO, much higher J_c values are obtained as a result of the intrinsic vortex pinning between the CuO$_2$ planes (see section 2.3). $V - J$ curves measured on YBCO CCs with $\vec{B}||\vec{ab}$ reveal a NOLD-like behaviour, which is a sign for current limitation by grain boundaries (see Fig. 6.7). The complex grain boundary network of the YBCO CC with multiple misorientation angles in the $a - b$ plane and in the c-direction makes it difficult to conclude which kind of current limitation mechanism is active in this geometry. The out-of-plane misorientation of the grains in the RABiTS tape, measured by EBSD (see section 5.3.1) are thought to affect the transport current leading to a kinking of the vortex lattice in Josephson strings and Abrikosov vortices (see section 2.3) that reduces J_c. Investigations on YBCO bicrystals with well-defined c-axis misorientations are required to clarify the effects of such grain boundaries on the transport current of the YBCO CC when B is parallel to the $a - b$ plane.
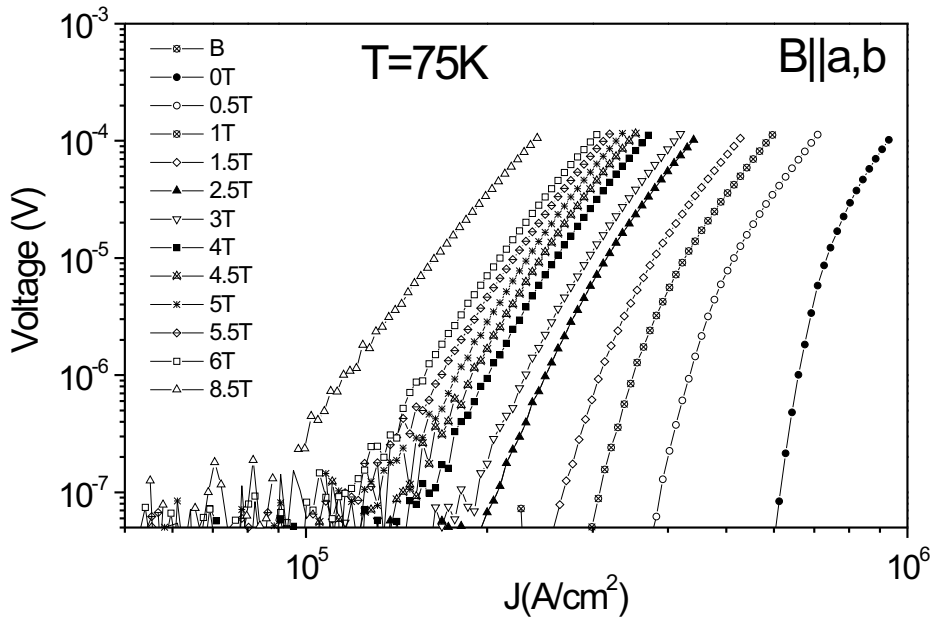

Fig. 6.7: $V - J$ characteristics of a YBCO CC measured for different magnetic fields at 75 K. The magnetic field has been applied parallel to the $a - b$ planes of YBCO.

6.3 Determination of the irreversibility field

The irreversibility field B_{irr} is an important parameter for practical applications of superconducting materials. For magnetic fields above B_{irr} pinning is no longer effective and consequently, J_c drops to zero. B_{irr} of the YBCO CC was obtained from the $V - J$ characteristics as the applied magnetic field for which the $V - J$ curves start to show an ohmic behaviour. In order to determine the first $V - J$ curve showing ohmic behaviour, a quadratic fit of the $V - J$ curves in the logarithmic representation is used: $\ln(V)=C+B\ln(J)+A[\ln(J)]^2$, where the coefficients A, B and C are fitting parameters (see Fig. 6.8). This is the so-called curvature method that has been frequently applied in the literature for the determination of B_{irr} in different superconducting systems like BSCCO tapes [And97, Par96] and YBCO bicrystals [Hei99]. Usually, for applied magnetic fields below B_{irr}, the $\ln V$-$\ln J$ diagrams can be described by a polynomial fit where the coefficient A of the quadratic term is larger than 0. The irreversibility field B_{irr} is reached when $\ln V$-$\ln J$ describes a linear correspondence with slope 1. The fit of the $\ln V$-$\ln J$ diagrams was carried out for voltages below 0.5 μV. Applying this procedure, B_{irr} of the YBCO CC was
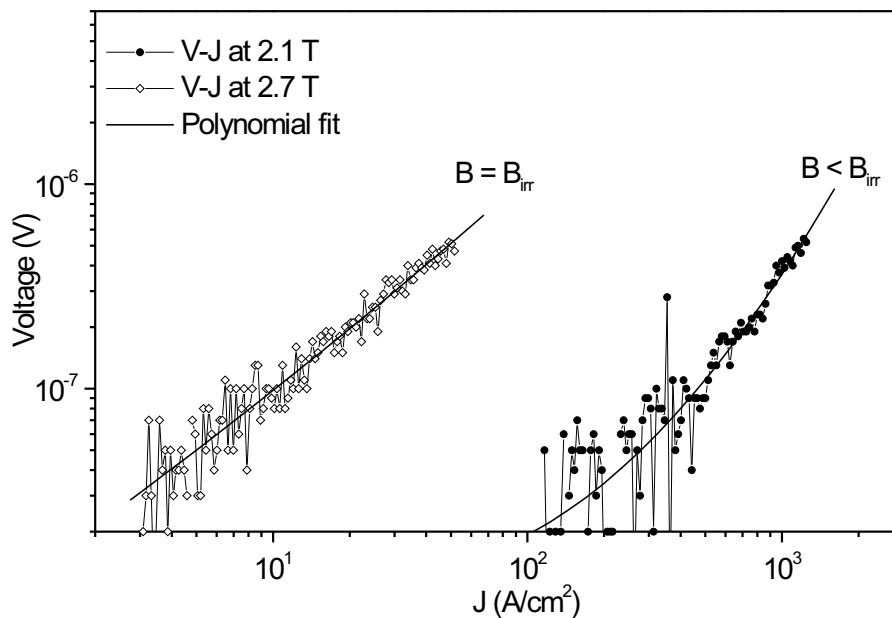

Fig. 6.8: Determination of B_{irr} using the curvature method. The $V - J$ curves measured at applied magnetic fields below B_{irr} reveal a quadratic dependence $\ln(V)=C+B\ln(J)+A[\ln(J)]^2$ with the coefficient A larger than 0. Increasing the applied field, B_{irr} is defined as the magnetic field where the $\ln V$-$\ln J$ diagrams reveal a linear dependence with a slope 1, which corresponds to an ohmic behaviour.
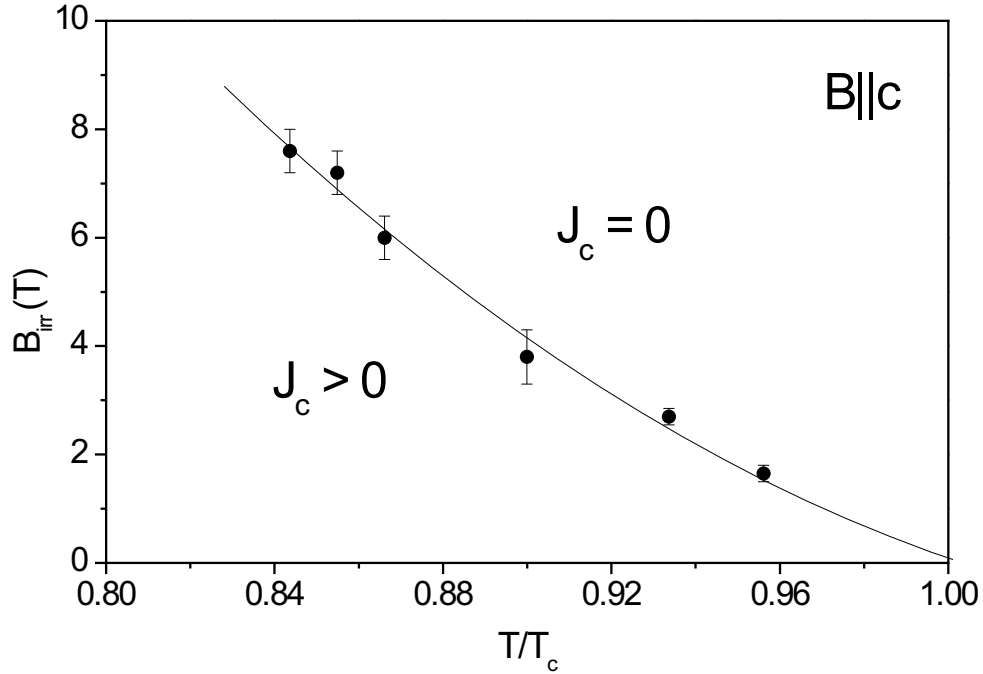
Fig. 6.9: Irreversibility line for the YBCO CC obtained from the measured $V - J$ characteristics.

determined as a function of temperature. The obtained irreversibility line is shown in Fig. 6.9. Here, the relation between B$_{irr}$ and the reduced temperature $t = T/T_c$ can be described by,

$$B_{irr} = B_0 \left(1 - \frac{T}{T_c} \right)^n \tag{6.1}$$

where B_0 is a constant, and n is found to equal 1.3 in this case.

6.4 J_c measurements on coated conductors

The critical current density J_c of the YBCO CC was also obtained from the $V - J$ characteristics, defining J_c as $V(J_c) = 8 \times 10^{-8}$ V. This voltage criterion corresponds to an electric field criterion of $E = 1$ μV/cm over the bridge of 800 μm length. Figure 6.10 shows results of J_c measurements at different magnetic fields and temperatures for the YBCO CC, where it is seen that J_c decreases with increasing applied magnetic fields. The drop in J_c becomes more pronounced at temperatures close to T_c, where stronger thermally activated flux creep mechanisms occur.
The J_c of YBCO CCs is found to be strongly reduced by the GBN propagated from the RABiTS tape, producing a clear enhancement in J_c when the biaxial texture of
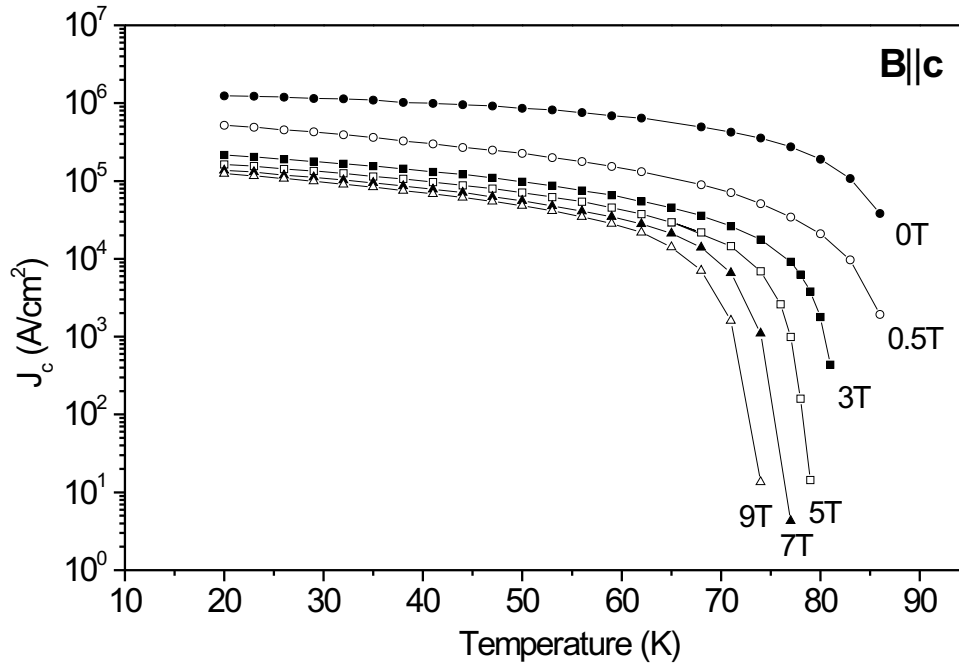
Fig. 6.10: $J_c(T)$ dependence at different magnetic fields for a YBCO CC.

the RABiTS tape is improved. Before coating with buffer and YBCO layers, the texture of different RABiTS tapes was measured using EBSD, determining which is the maximum value of the grain boundary distribution function of the different RABiTS tapes (see Fig. 6.11). This value was found to be 8.5° for the Ni-0.1at.%Mn RABiTS tape and 5.5° for the pure Ni RABiTS tape. Figure 6.12 shows the results for $J_c(T)$ measurements carried out at 77 K and in self-field for YBCO CCs grown on these RABiTS substrates, revealing an improvement in J_c from 0.3 MA/cm^2 for the Ni-0.1at.%Mn tape to 1.3 MA/cm^2 for the pure Ni tape.

The improvement in J_c with the reduction of the maximum of the grain boundary distribution function of the GBN may be explained considering that the transport current is affected only by grain boundaries with misorientation angles exceeding a cut-off angle (see section 3.1). Therefore, reducing the misorientation angles of the GBN, i.e., improving the biaxial texture, the percolation of the current flow becomes less significant and consequently J_c is not so strongly reduced.

6.5 Magnetic field dependence of J_c

J_c measurements in magnetic fields should help to clarify the limitation of the critical current induced by the GBN and provide information on the pinning mechanisms in the YBCO CC. The magnetic field dependence of J_c for the YBCO CC and
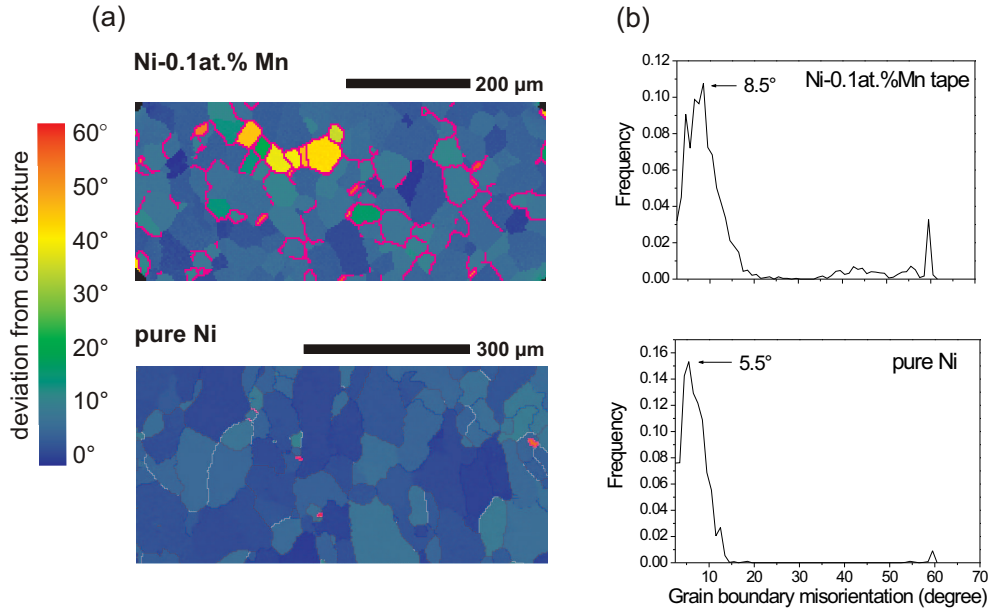
Fig. 6.11: (a) EBSD measurements for different RABiTS tapes: Ni-0.1at.%Mn tape and pure Ni tape. Grain boundaries with misorientation angles larger than $10°$ are represented as pink lines. (b) Distribution of the grain boundary misorientation angles found in the RABiTS tapes.

Fig. 6.12: Enhancement of $J_c(T)$ when the biaxial texture of the RABiTS tape is improved: the YBCO CC grown on a Ni-0.1at.%Mn tape reveals a J_c of 0.3 MA/cm^2 at 77 K that is enhanced to 1.3 MA/cm^2 using a pure Ni tape with a better biaxial texture.

for the same system grown on a single-crystalline Ni film were determined from the $V - J$ curves measured on these samples (see section 6.2.1).
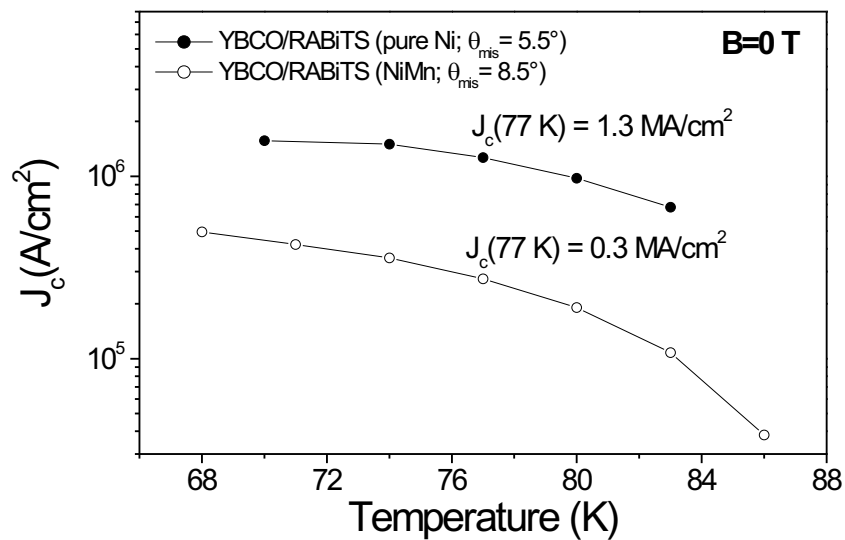
Figure 6.13 demonstrates that the $J_c(B)$ dependence is different in the two systems. YBCO grown on the single-crystalline Ni film presents an exponential $J_c(B)$ decay over the complete range of measured magnetic fields caused by thermally activated flux creep [Sta98, Ste97], showing that this mechanism is the principal limitation of J_c in this sample. Here, the critical current density is termed intragrain J_c, since the current limitation occurs within the YBCO grains. In the case of the YBCO CC, different $J_c(B)$ dependencies are found as a function of the temperature and the applied magnetic field. At 60 K, $J_c(B)$ can be described by a power law behaviour over the complete range of measured magnetic fields. At higher temperatures, such as 77 K, a transition in the $J_c(B)$ dependence from a power law to an exponential decay is observed as the applied magnetic field increases.

For the YBCO CC, the power law behaviour at 77 K is associated with an intergrain limitation of J_c by the GBN, and the exponential decay with an intragrain J_c limitation by flux creep in the YBCO grains. At this temperature, the transition from intergranular to intragranular J_c takes place when the dissipation mechanism due to flux creep within the YBCO grains becomes stronger than the dissipation in the GBs of the GBN, and it occurs at the crossover field B^{cr} that lies at 4 T (Fig. 6.13).
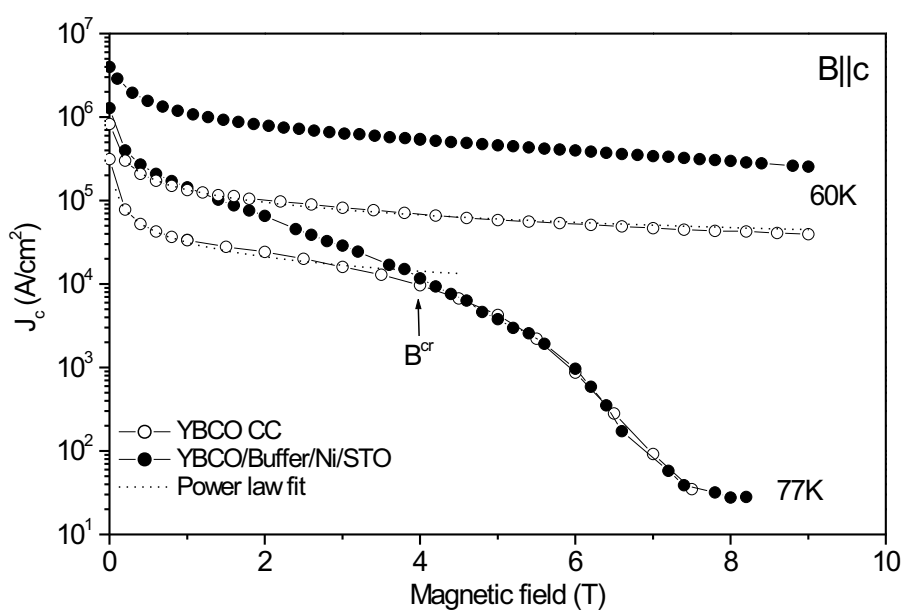

Fig. 6.13: Dependence of J_c on the applied magnetic field for the YBCO CC on RABiTS (open circles) and YBCO on the single-crystalline Ni film (filled circles) at 60 K and 77 K. The dotted line represents a power law fit of the measurements.

B^{cr} can be seen as the point where the GBN becomes "transparent" for the current limitation in the YBCO CC. At 60 K, the situation is probably the same but B^{cr} is shifted to magnetic fields above 9 T (maximum available magnetic field in the experiment). These results are consistent with the $V - J$ characteristics of the YBCO CC explained in section 6.2.1 that indicated a different behaviour when the current is limited either by the GBs or by the YBCO grains.

Figure 6.14 shows the $J_c(B)$ curves of the YBCO CC for a broader temperature range, revealing a pure power law dependence for temperatures below 70 K, while a crossover from power law to exponential decay is observed above 70 K. The power law behaviour of $J_c(B)$ found below B^{cr} follows the relation,

$$J_c(B) = J_c(0) \left(\frac{B_0}{B} \right)^n \tag{6.2}$$

with the exponent $n \approx 0.5$ for all temperatures. As shown in section 3.2.2, this value results from flux pinning at the dislocation cores of the GBs and corroborates the J_c limitation by the GBs in the YBCO CC.

Figure 6.15 demonstrates the determination of B^{cr} from the $J_c(B)$ measurement of the YBCO CC at 85 K. Applying this method for all $J_c(B)$ curves of Fig. 6.14, a $B^{cr}(T)$ dependence is found; B^{cr} decreases with increasing temperature, e.g., from 5.5 T at 75 K to 1 T at 85 K. This means that when the temperature increases, flux creep effects become dominant and limit J_c.
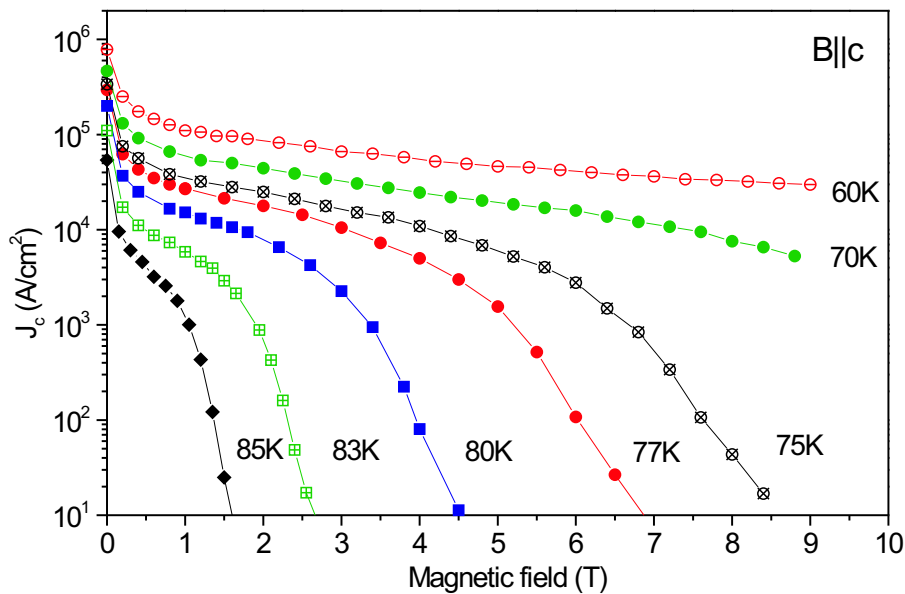

Fig. 6.14: Dependence of J_c on the applied magnetic field for the YBCO CC at different temperatures.
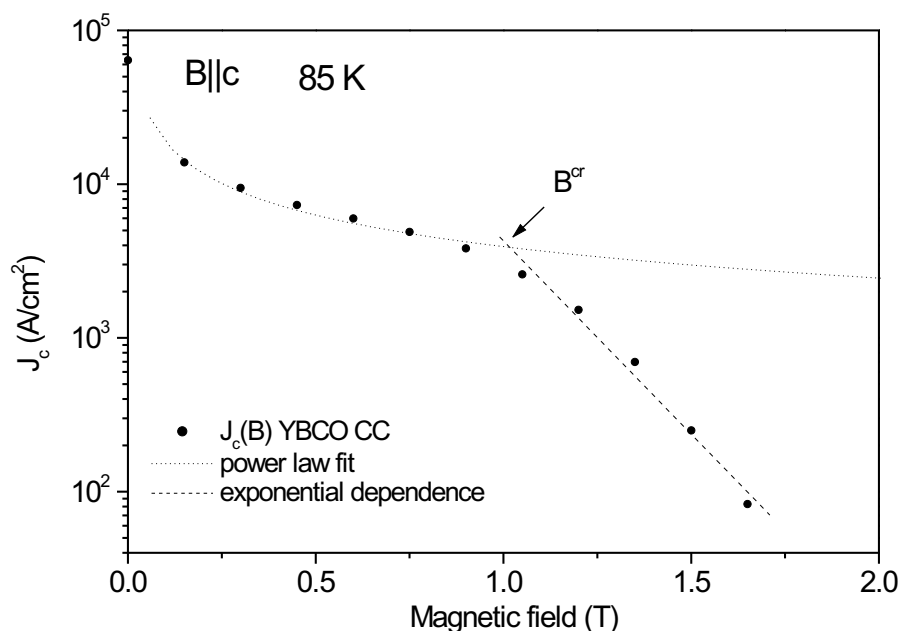
Fig. 6.15: Method for the detection of the crossover field from $J_c(B)$ measurements at 85 K. B^{cr} is the intersection point between the power law behavior of the intergrain J_c and the exponential dependence of the intragrain J_c.

Figure 6.16 shows the obtained crossover fields at different temperatures together with the irreversibility line, allowing the evaluation of the range of temperatures and magnetic fields over which the GBN limits the critical current in the YBCO CC. At temperatures and magnetic fields below the crossover line the measured critical current is intergranular and viscous flux flow along the GBs is expected to occur, limiting J_c in the YBCO CC. The area in the $B - T$ plane bounded by the crossover field and the irreversibility field lines corresponds to a range of temperatures and magnetic fields where the critical current of the YBCO CC is completely intragranular; the critical current density in this range is limited only by flux creep in the YBCO grains and the value of the critical current is the same as in a system without GBs (compare the $J_c(B)$ curve at 77 K in Fig. 6.13). The area above the irreversibility field line is of no importance for applications because, at these temperatures and magnetic fields, the critical current of the superconductor is zero.

In order to study the effect of the GBN in more detail, $J_c(B)$ was measured on YBCO CCs prepared on RABiTS tapes with a better biaxial texture than the YBCO CC prepared on the Ni-0.1at.%Mn tape (YBCO CC previously analysed). In this case, pure Ni and non-magnetic Ni-13at.%Cr tapes were used, which have grain boundary distribution functions that show maxima centred at misorientation angles of 5.5° and 6.6°, respectively. In comparison the Ni-0.1at.%Mn tape had a
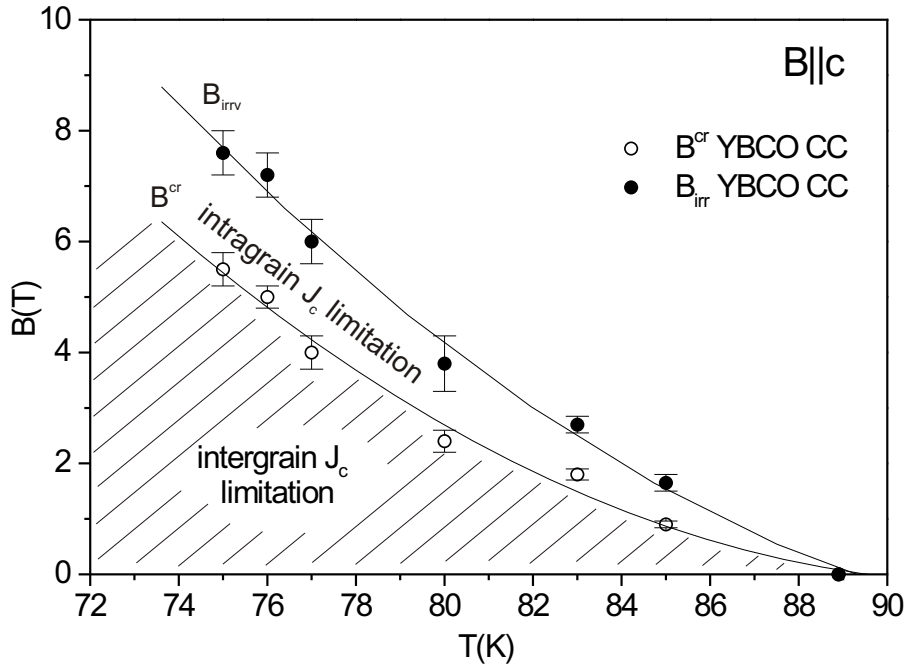
Fig. 6.16: Irreversibility and crossover field line for the YBCO CC [Fer03]. The values were obtained from $V - J$ characteristics at different temperatures and magnetic fields.

maximum centred at 8.5°, as previously discussed in section 6.4.

As can be seen in Fig. 6.17, YBCO CCs prepared using these new RABiTS tapes have higher J_c values around 1 MA/cm^2 (at 77 K and self-field), and moreover, the transition from intergranular to intragranular J_c takes place at $B^{cr} = 1.8$ T, which contrasts to the $B^{cr} = 4$ T at 77 K for the YBCO CC grown on the Ni-0.1at.%Mn tape. The shift of B^{cr} to lower values is directly related to the lower grain boundary misorientation angles of the samples that lead to smaller dissipation in the GBN. Consequently, in such a situation flux creep in the YBCO grains becomes the dominant limitation at lower applied magnetic fields.

Considering the reduction of B^{cr} at 77 K for an YBCO CC on a RABiTS tape with a better biaxial texture, a complete shift of the B^{cr} line to lower values may be expected as indicated in Fig. 6.18, resulting in a much larger area where the critical current of the YBCO CC is completely intragranular without any effect of the YBCO GBN on J_c. Therefore, J_c values like in a single-crystalline YBCO film could be obtained in this area. Future work should verify such a shift of the crossover field line also for other temperatures.
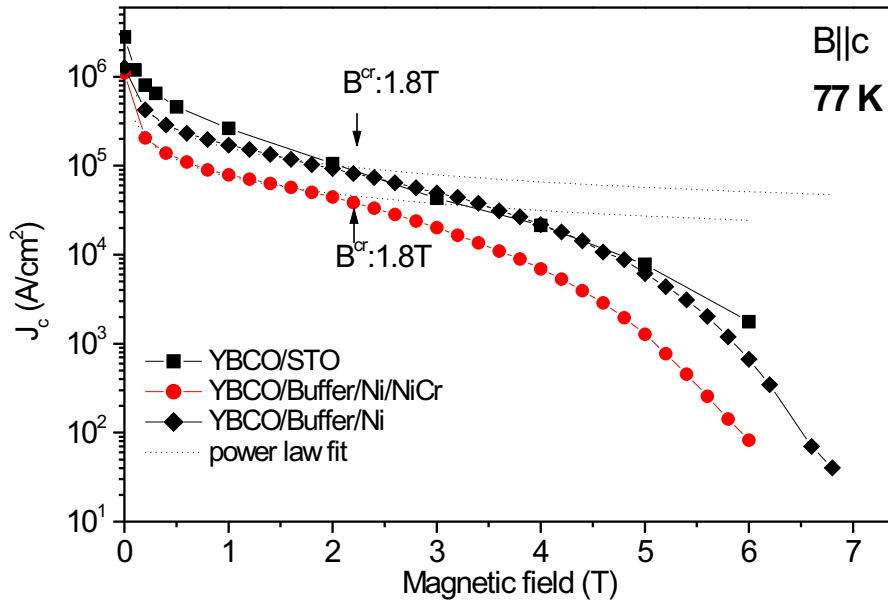
Fig. 6.17: Dependence of J_c on the applied magnetic field at 77 K for YBCO CCs on RABiTS tapes with different biaxial textures. A single crystalline YBCO film (YBCO/STO) with similar J_c was taken as a reference.
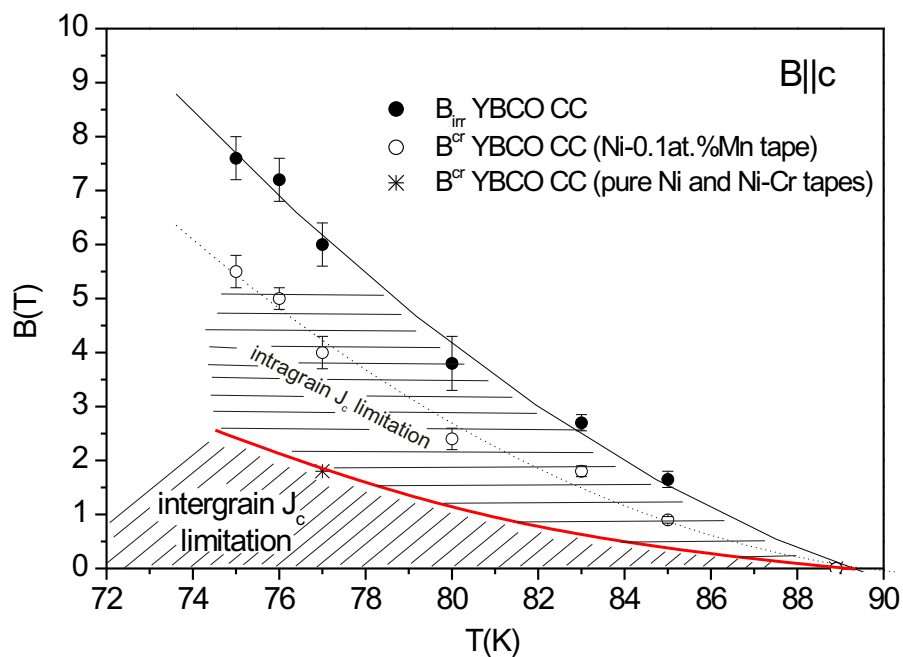

Fig. 6.18: Expected shift of the crossover field line to lower values as result of an improvement in the biaxial texture of the RABiTS tape.

6.6   Pinning force density in coated conductors

From experiments with conventional type II superconductors it is known that the pinning force density defined as $F_p = |\vec{J}_c \times \vec{B}|$ obeys scaling laws of the form $F_p \propto [(B_{c2}(T)]^n f(b)$, where b is the reduced magnetic field $b = B/B_{c2}$ [Kra73], and $f(b)$ can be expressed by $f(b) = b^n (1 - b)^m$ [Cam72]. In the case of high temperature superconductors B_{c2} must be replaced by B_{irr}, since pinning is no longer effective between B_{irr} and B_{c2}. Consequently, the pinning force above B_{irr} is practically zero.

The dependence of the pinning force density on the reduced magnetic field $F_p(b)$ usually shows a maximum that shifts depending on structure, microstructure and pinning mechanism of the material. F_p can be calculated for each temperature from $J_c(B)$ measurements on the YBCO CC (see Fig. 6.14).

The results are shown in Fig. 6.19: for temperatures between 75 K and 85 K the normalised pinning force density F_p/F_p^{max} versus the reduced magnetic field b can be scaled by the following relation $f(p) \propto b^{0.8}(1 - b)^2$. This result suggests a common pinning mechanism for all measured temperatures in the YBCO CC. For reduced magnetic fields above 0.5, deviations of the normalised pinning force density occur as a result of thermally activated flux creep effects that become important close to B_{irr}.
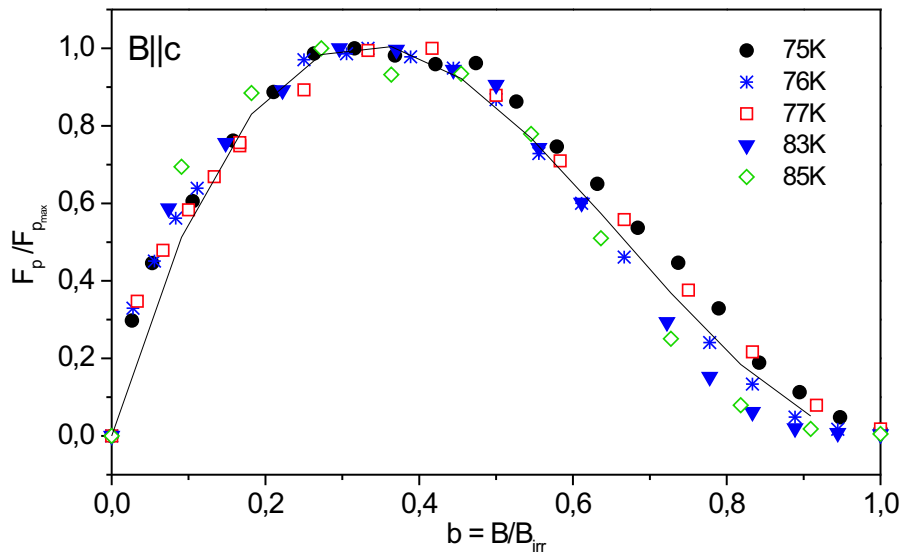

Fig. 6.19: Normalised pinning force density F_p/F_p^{max} for the YBCO CC at different temperatures. A scaling of the pinning force density is found for all measured temperatures (solid curve).

6.7 J_c anisotropy measurements

The J_c anisotropy in the YBCO CC was studied by varying the direction between the applied magnetic field and the c-axis of YBCO, keeping the directions of the magnetic field and the current always perpendicular to each other. Therefore, the magnitude of the Lorentz force $\vec{F}_L = \vec{J}_c \times \vec{B}$ is constant. Figure 6.20 presents results of $J_c(B)$ measurements carried out at different temperatures and magnetic fields applied perpendicular to the c-axis of YBCO. In this geometry, a slight reduction in J_c at 70 K, 77 K and 80 K is revealed as the applied magnetic field is increased. However, at 85 K that is close to T_c, $J_c(B)$ decreases strongly, since the intrinsic pinning is less effective. This is due to the coherence length - temperature dependence that follows the relation $\xi_{GL} \propto [1 - T/T_c]^{1/2}$ for $T \lesssim T_c$, and leads to an increase of the coherence length ξ_{GL} with temperature. Consequently, a reduction in the intrinsic flux line pinning occurs when the core diameter $(2\xi_c)$ of the Josephson vortex exceeds the layer spacing d.

The results obtained for the angular dependence of J_c in the YBCO CC at 77 K and an applied magnetic field of 1 T are shown in Fig. 6.21(a). Two sharp maxima are found at 90° and 270°. In these directions, the applied magnetic field lies parallel to the CuO$_2$ planes and the intrinsic pinning against the Lorentz force in the c-direction is very effective. $J_c(90°)$ appears to be slightly higher than $J_c(270°)$, which is most probably caused by a slightly different pinning mechanism at the film surface than at the film-substrate interface. Such an effect is a consequence of
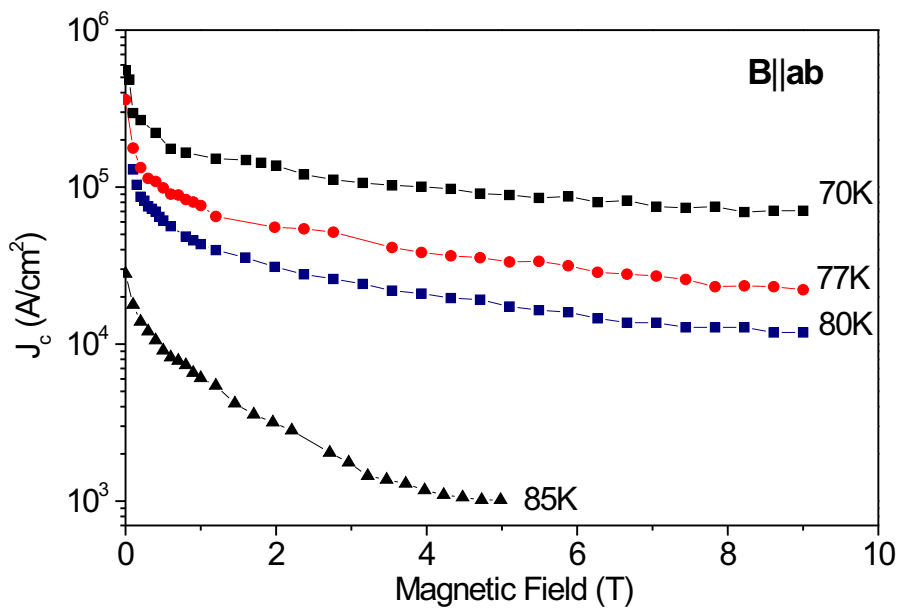

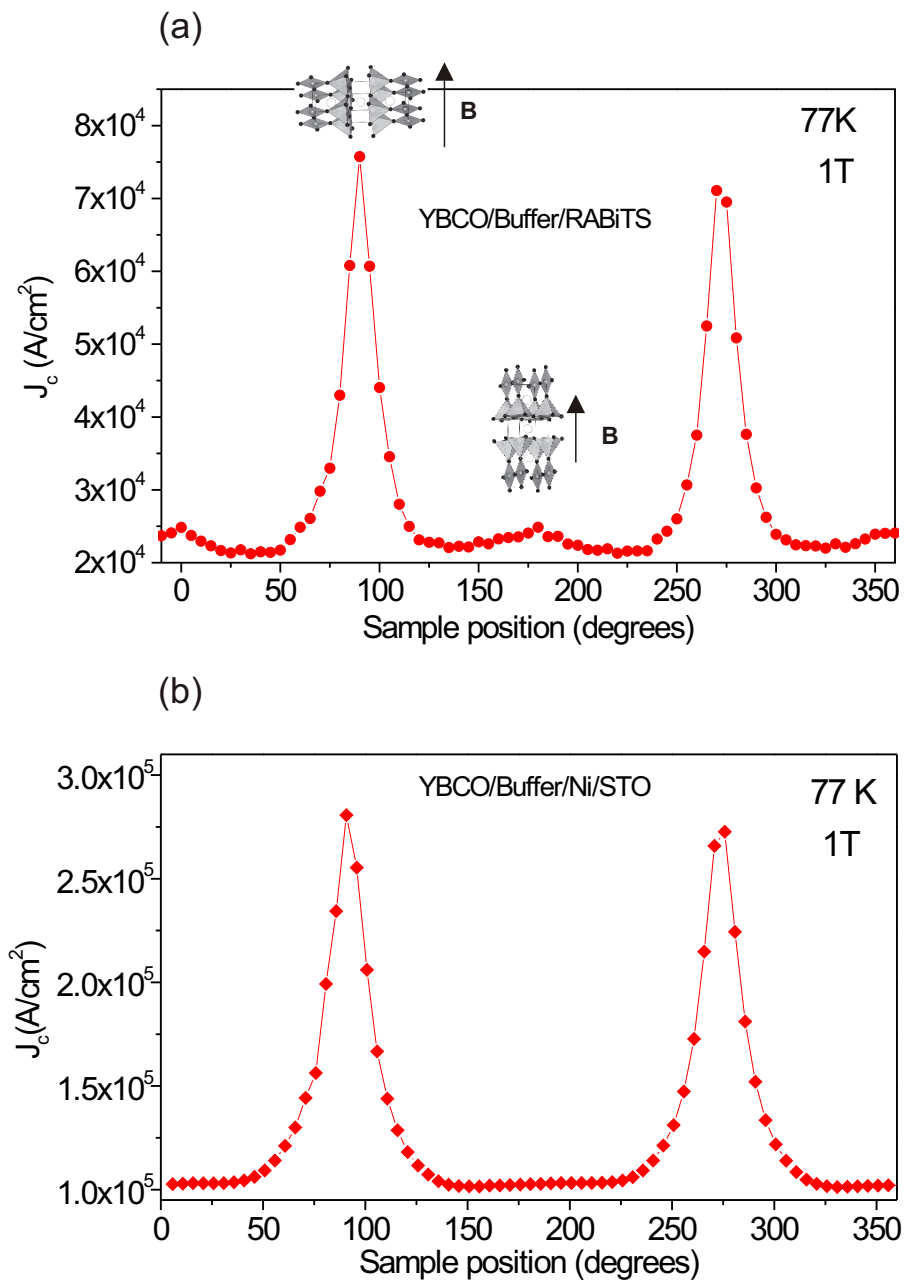Fig. 6.20: $J_c(B)$ measurements for the YBCO CC with $B||ab$.

(a)

(b)

Fig. 6.21: $J_c(\theta)$ measured at 77 K and 1 T for (a) YBCO CC, and (b) the YBCO film grown on the single-crystalline Ni film.

the roughness of the YBCO film surface, typical for on-axis laser deposition, which leads to a lower pinning capability at the surface than at the interface [Roa90a, Roa90b]. The assumption that the pinning mechanism is different for the film surface and interface is further supported by anisotropic J_c measurements carried out on YBCO films grown by off-axis laser deposition, which have smoother surfaces, obtaining $J_c(90°)=J_c(270°)$ for these films [Hol93, Hol95]. When the applied magnetic field is not perpendicular to the c-axis, J_c decreases drastically. In this geometry, the flux lines develop kinks composed of Josephson strings between the CuO_2 planes and Abrikosov vortices that cross the CuO_2 planes (see section 2.3). Another interesting feature of the $J_c(\theta)$ results shown in Fig. 6.21 (a) are the small J_c maxima that are found at 0° and 180°. They are an indication of flux line pinning in the YBCO CC when the applied magnetic field is parallel to the c-axis. Considering the pinning by GBs detected in $J_c(\theta)$ measurements carried out on YBCO bicrystals [Día98b], it can be expected that in the case of the YBCO CCs the GBN produces similar vortex pinning by dislocations in the GBs. Figure 6.21 (b) shows measurements carried out on the YBCO film grown on a single-crystalline Ni film (without grain boundaries), showing no peaks at 0° and at 180°, and hence, no signs of pinning centres aligned along the c-axis.

The $J_c(\theta)$ measurements on the YBCO CC were carried out at 77 K and 70 K for different magnetic fields. Figure 6.22 shows the $J_c(\theta)$ results normalised to the maximum J_c. At 77 K and high magnetic fields, the J_c anisotropy in the YBCO CC becomes more important and the ratio between $J_c(90°)$ and $J_c(0°)$ is higher than at lower fields. This can be explained considering that at high magnetic fields (5T) strong flux creep effects are expected for applied magnetic fields that are not aligned with the CuO_2 planes, particularly at 0°. In contrast, at 70 K the difference between $J_c(90°)$ and $J_c(0°)$ at 5 T is not so pronounced due to the weaker flux creep effects at this temperature. The small J_c maxima at $\theta = 0°$ and 180° are observed only for B = 0.5 T and 1 T [Fig. 6.22 (a)]. For 3 T these maxima are not well defined, and for 5 T they do not exist any more at 77 K. This behaviour is probably connected to the proximity to the irreversibility field when the magnetic field increases, and may be related to the crossover behaviour commented in section 6.5. Below B^{cr} there is an effective pinning at the GBN (small local maxima at $\theta= 0°$ and 180°), and above B^{cr} the flux line pinning at the GBN is no longer effective, leading to the disappearance of the small local maxima.
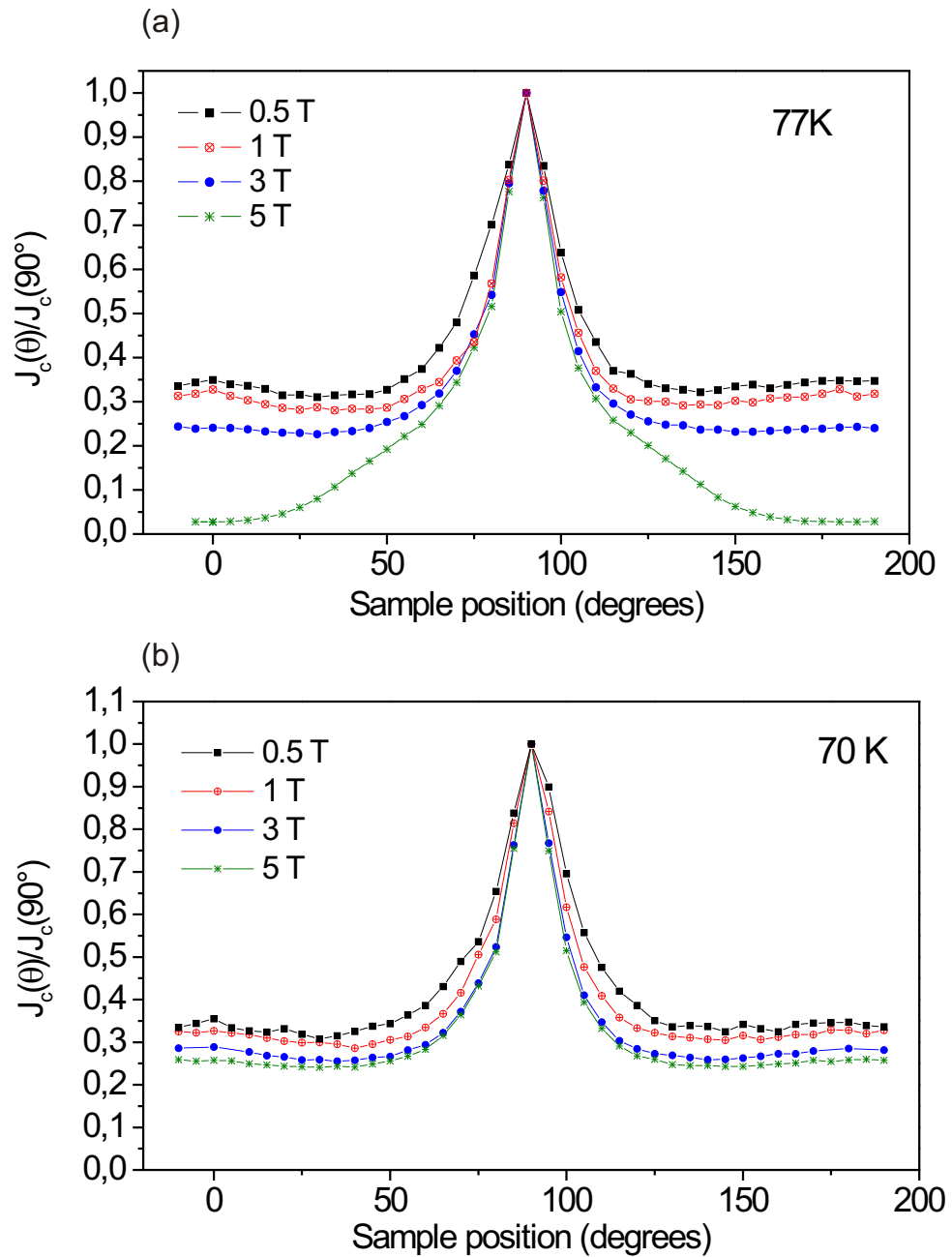
(a)

(b)

Fig. 6.22: $J_c(\theta)$ for the YBCO CC on a Ni-0.1at.%Mn RABiTS tape at (a) 77 K, and (b) 70K, measured at 0.5 T, 1 T, 3 T and 5 T.

Chapter 7

Conclusions and Outlook

YBCO CCs have been prepared by pulsed laser deposition using the RABiTS approach. Different biaxially textured metallic substrates, with different compositions (pure Ni (99.98%), Ni-0.1 at.% Mn, Ni-13 at.% Cr, and Ni-5 at.% W) and different biaxial texture quality were used. A critical point for the preparation of samples with high critical current densities (above 1 MA/cm^2 at 77 K and self-field) is the growth of an effective buffer layer system that prevents chemical reactions between the metal substrate and the YBCO film, and allows the YBCO film to grow biaxially textured. With this aim in mind, a buffer layer system composed of a thin CeO$_2$ film (50 nm) and a thick YSZ film (600 nm) was used. The prepared YBCO CCs have critical temperatures between 88 K and 90 K with a transition width less than 1 K. This shows the efficiency of the buffer layer system in preventing Ni diffusion into the YBCO film. However, a thin NiO layer grows (111) oriented at the interface between the RABiTS substrate and the CeO$_2$ film during YBCO film deposition. This is caused by oxygen diffusion through the buffer layer system due to the high substrate temperature (770°C) and oxygen partial pressure (0.3 mbar) required for the optimised formation of the superconducting YBCO phase. Nevertheless, x-ray and TEM analyses show that the thin NiO film does not adversely affect the biaxial texture of the YBCO CC.

Texture analysis reveals an improvement in the biaxial texture (both in-plane and out-of-plane) of the CeO$_2$ film with respect to the RABiTS tape (approximately of 1° in-plane, and 0.5° out-of-plane), and of the YBCO film with respect to the YSZ film (more than 1° in-plane and approximately 0.5° out-of-plane). The reason for improvement in the in-plane texture during the epitaxial growth is still unclear. However, the enhancement in the out-of-plane texture can be explained by the growth mechanism of both materials on their respective substrates: the CeO$_2$ film tilts its c-axis towards surface normal on out-of-plane misoriented RABITS grains, while the YBCO film has a preferred lateral growth with the $a - b$ planes paral-

lel to the substrate surface, which results in an improvement of the out-of-plane orientation of the films.

Electron back scatter diffraction measurements reveal the granular structure of the YBCO CC with grain sizes between 20 and 40 μm. These large grains are propagated from the RABiTS tape to the YBCO film due to the epitaxial growth, forming a grain boundary network (GBN) in the YBCO film, where the misorientation angles are typically less than 12°. These grain boundaries are responsible for the reduced critical current density of the YBCO CC. Moreover, higher grain boundary angles are found isolated in the YBCO CC, but they do not affect the critical current density due to the percolative nature of the current flow in these samples. A direct relation between the texture of the RABiTS tape and the critical current density of the YBCO CC is found. The experiments revealed an improvement from 0.3 MA/cm^2 to 1.3 MA/cm^2 (at 77 K and self-field) when the maximum of the grain boundary distribution function (measured by EBSD) in the RABiTS tape drops from 8.5° to 5.5°.

For the study of the J_c limitation by the GBN of the YBCO CCs, $J_c(B)$ measurements have been performed. Different mechanisms of J_c limitation were observed in the YBCO CC, depending on the temperature and applied magnetic fields. At low magnetic fields the critical current is limited by the GBN (intergrain critical current). This is reflected in a power-law dependence of $J_c(B)$ and non-Ohmic linear differential-like signature of the $V - J$ curves. At higher magnetic fields, $J_c(B)$ is found to be limited by pinning within the YBCO grains (intragrain critical current) with a typical exponential decay dependence. The transition from intergrain to intragrain critical current limitation occurs at the so-called crossover magnetic field B^{cr}, that is found to shift to lower magnetic fields as the temperature is increased. This crossover behaviour between intergrain and intragrain current limitation can have important implications for CC applications. For applications that require the presence of high magnetic fields, the GBN of the YBCO CC does not limit the critical current and hence, J_c is completely intragrain limited. The irreversibility field represents in this case the upper limit for applications in high magnetic fields with the GBN having no influence. The use of RABiTS tapes with a better texture, i.e. smaller GB angles, does not avoid this problem since the crossover field is shifted to lower values, leaving the exponential J_c decrease at high fields unchanged. Only in the case of applications that require magnetic fields lower than the crossover field can an improvement of the GBN angles in the sample be useful. Consequently, it is concluded that the GBN strongly limits the critical current in the YBCO CC but only in the range of magnetic fields below B^{cr}. The GBN does not represent an obstacle for applications that require fields above this crossover point.

Additionally, anisotropic critical current density measurements have shown flux line pinning in the grain boundaries of the YBCO CC. Further work based on measurements of the anisotropic critical current densities of YBCO bicrystals with well defined grain boundary misorientation angles and different geometries (twist and tilt grain boundaries) is required. These measurements can lead to determine which grain boundaries are the principal pinning centres in the YBCO CC, and in which ranges of magnetic fields they pin the flux lines effectively.

Recent measurements on thin films of a mixed $(RE)Ba_2Cu_3O_{7-\delta}$ [Y in YBCO is substituted by a mixture of rare earth metals (Gd, Nd, Eu)] have revealed enhanced critical current densities and irreversibility fields due to an improvement in the pinning properties [Cai03]. Therefore, future work should include optimisation of $(Gd, Nd, Eu)Ba_2Cu_3O_{7-\delta}$ CCs to improve the superconducting properties.

Finally, coming back to the preparation of YBCO CCs, it has been seen that in some cases the prepared samples show defects that are thought to be related to natural impurities (C and S) found in the tapes . Therefore a systematic study of the composition of the materials used to produce the RABiTS tapes is proposed, in order to determine the kind and the amount of impurity that allows the preparation of YBCO CCs without defects. This is a critical point for the preparation of YBCO CCs with full control of their structural and transport properties.

Bibliography

[Abr98]   A. A. ABRIKOSOV: *Fundamentals of the theory of metals* (Elsevier Science Publishers B. V., 1998).

[Amr95]   T. AMREIN, L. SCHULTZ and K. URBAN: *Low-noise dc superconducting quantum interference devices in $Bi_2Sr_2CaCu_2O_{8+x}$ thin films*. J. Appl. Phys. **77** (1995) 6703.

[And62]   P. W. ANDERSON: *Theory of flux creep in hard superconductors*. Phys. Rev. Lett. **9** (1962) 309.

[And64]   P. W. ANDERSON and Y. B. KIM: *Hard superconductivity: Theory of the motion of Abrikosov flux lines*. Reviews of modern physics **36** (1964) 39.

[And97]   J. W. ANDERSON, J. A. PARELL, M. POLAK and D. C. LARBALESTIER: *Determination of irreversibility field variations in monofilamentary $(Bi,Pb)_2Sr_2Ca_2Cu_3O_x$ tapes by transport current methods*. Appl. Phys. Lett. **71** (1997) 3893.

[Att02]   A. ATTENBERGER, J. HÄNISCH, B. HOLZAPFEL and L. SCHULTZ: *Electrical transport properties of Bi-2223 [001] tilt grain boundary junctions*. Physica C **372-376** (2002) 649.

[Auc88]   O. AUCIELLO, S. ATHAVALLE, O. E. ANKINS, M. SITO, A. F. SCHREINER and N. BIUNNO: *Spectroscopy analysis of electrically excited species in XeCl excimer laser-induced plasmas from the ablated high temperature superconductor $YBa_2Cu_3O_{7-x}$*. Appl. Phys. Lett. **53** (1988) 72.

[Bar65]   J. BARDEEN and M. J. STEPHEN: *Theory of the motion of vortices in superconductors*. Phys. Rev. **140** (1965) 1197.

[Bau99]   M. BAUER, R. SEMERAD and H. KINDER: *YBCO films on metal substrates with biaxially aligned MgO buffer layers*. IEEE Trans. Appl. Superconductivity **9** (1999) 1502.

[Bea69] M. R. BEASLEY, R. LABUSCH and W. W. WEBB: *Flux creep in type II superconductor*. Phys. Rev. **181** (1969) 682.

[Bet97a] V. BETZ, B. HOLZAPFEL, D. RAONSER and L. SCHULTZ: *In-plane aligned Pr_6O_{11} buffer layers by ion-beam-assisted pulsed-laser deposition on metal substrates*. Appl. Phys. Lett. **71** (1997) 2952.

[Bet97b] V. BETZ, B. HOLZAPFEL and L. SCHULTZ: *Growth of biaxially aligned buffer layers for YBCO tapes by ion-beam-assisted laser deposition and in-situ RHEED texture analysis*. IEEE Trans. Appl. Superconductivity **7** (1997) 1436.

[Bet97c] V. BETZ, B. HOLZAPFEL and L. SCHULTZ: *In situ reflection high energy electron bombardment analysis of biaxially oriented yttria-stabilized zirconia thin film growth on amorphous substrates*. Thin Solid Films **301** (1997) 28.

[Bet98] V. BETZ: *Biaxial orientiertes Schichtwachstum unter Ionenbeschuß*. Ph.D. thesis, Technische Universität Dresden (1998).

[Bla94] G. BLATTER, M. V. FEIGELMAN, V. B. GESHKENBEIN, A. I. LARKIN and V. M. VINOKUR: *Vortices in high-temperature superconductors*. Rev. Mod. Phys. **66** (1994) 1125.

[Bre95] V. BREIT, P. SCHWEISS, R. HAUFF, H. WÜHL, H. CLAUS, H. RIETSCHEL, A. ERB and G. MÜLLER-VOGT: *Evidence for chain superconductivity in near-stoichiometry $YBa_2Cu_3O_x$ single crystals*. Phys. Rev. B **52** (1995) 15727.

[Bro98] N. D. BROWNING, J. P. BUBAN, P. D. NELLIST, D. P. NORTON, M. F. CHISHOLM and S. J. PENNYCOOK: *The atomic origins of reduced critical currents at (001)-tilt grain boundaries in $YBa_2Cu_3O_7$ thin films*. Physica C **294** (1998) 183.

[Buc91] W. BUCKEL: *Superconductivity*. 1 edn. (VCH Verlagsgesellschaft mbH Weinheim, 1991).

[Bud03] J. D. BUDAI, W. YANG, N. TAMURA, J. CHUNG, J. Z. TISCHLER, B. C. LARSON, G. E. ICE, C. PARK and D. P. NORTON: *X-ray microdiffraction study of growth modes and crystallographics tilts in oxide films on metal substrates*. Nature materials **2** (2003) 487.

[Cai98] X. Y. CAI, A. GUREVICH, I. F. TSU, D. L. KEISER, S. E. BABCOCK and D. C. LARBALESTIER: *Large enhancement of critical-current density due to*

vortex matching at the periodic facet structure in $YBa_2Cu_3O_{7-\delta}$ bicrystals. Phys. Rev. B **57** (1998) 10951.

[Cai03] C. CAI, B. HOLZAPFEL, J. HÄNISCH, L. FERNÁNDEZ and L. SCHULTZ: *High critical current density and its field dependence in mixed rare earth (Gd, Eu, Nd)Ba$_2$Cu$_3$O$_{7-\delta}$ thin films* (2003). Accepted for publication in Appl. Phys. Lett.

[Cam72] A. M. CAMPBELL and J. E. EVETTS: *Flux vortices and transport currents in type II superconductors.* Advances in Physics **21** (1972) 199.

[Can01a] C. CANTONI, T. AYTUG, D. T. VEREBELYI, M. PARANTHAMAN, E. D. SPECHT, D. P. NORTON and D. K. CHRISTEN: *Conductive buffer layers and overlayers for thermal stability of coated conductors.* IEEE Trans. Appl. Superconductivity **11** (2001) 3309.

[Can01b] C. CANTONI, D. K. CHRISTEN, R., FEENSTRA, A. GOYAL, G. W. OWNBY, D. M. ZEHNER and D. NORTON: *Reflexion high-energy electron diffraction studies of epitaxial oxide seed-layer growth on rolling-assisted biax-ially textured substrate Ni(001): The role of surface structure and chemistry.* Appl. Phys. Lett. **79** (2001) 3077.

[Cas02] A. CASTAÑO, A. PALAU, J. C. GONZÁLEZ, S. PIÑOL, T. PUIG, N. MESTRES, F. SANDIUMENGE and X. OBRADORS: *Epitaxial nucleation and growth of buffer layers and Y123 coated conductors deposited by metal-organic decomposition.* Physica C **372-376** (2002) 806.

[Cas03] A. CASTAÑO, A. CAVALLARO, A. PALAU, J. GONZÁLEZ, M. ROSSELL, T. PUIG, F. SANDIUMENGE, N. MESTRES, S. PIÑOL, A. POMAR and X. OBRADORS: *High-quality YBa$_2$Cu$_3$O$_7$ thin films by trifluoroacetates met-alorganic deposition.* Superc. Sci. Technol. **16** (2003) 45.

[Cha94] R. CHATTERJEE, M. FUKUTOMI, S. AOKI, K. TOGANO and H. MAEDA: *Study of YBa$_2$Cu$_3$O$_{7-x}$ film growth on (200) oriented yttria stabilized zirconia buffer layer on metallic substrates.* Appl. Phys. Lett. **65** (1994) 109.

[Chi89] M. F. CHISHOLM and D. A. SMITH: *Giant torque magnetization anisotropy in Tl$_2$Ba$_2$CaCu$_2$O$_x$.* Philos. Mag. A **59** (1989) 181.

[Chi91] M. F. CHISHOLM and S. J. PENNYCOOK: *Structural origin of reduced critical currents at YBa$_2$Cu$_3$O$_{7-\delta}$ grain boundaries.* Nature **351** (1991) 47.

[Cle91]   J. R. CLEM: *Two-dimensional vortices in a stack of thin superconducting films: A model for high-temperature superconducting multilayers*. Phys. Rev. B **43** (1991) 7837.

[Cle98]   J. R. CLEM: *Anisotropy and two-dimensional behaviour in the high-temperature superconductors*. Supercond. Sci. Technol. **11** (1998) 909.

[Dan00]   G. A. DANIELS, A. GUREVICH and D. C. LARBALESTIER: *Improved strong magnetic-field performance of low-angle grain-boundaries of calcium and oxygen overdoped $YBa_2Cu_3O_{7-x}$*. Appl. Phys. Lett. **77** (2000) 3251.

[dB01a]   B. DE BOER, J. EICKEMEYER, N. REGER, L. FERNÁNDEZ, J. RICHTER, B. HOLZAPFEL, L. SCHULTZ, W. PRUSSEIT and P. BERBERICH: *Cube textured nickel alloy tapes as substrates for $YBa_2Cu_3O_{7-x}$-coated conductors*. Acta mater. **49** (2001) 1421.

[dB01b]   B. DE BOER, N. REGER, L. FERNÁNDEZ, J. EICKEMEYER, B. HOLZAPFEL, L. SCHULTZ, W. PRUSSEIT and P. BERBERICH: *Biaxially textured Ni-alloy tapes as substrate for buffer and YBCO film growth*. Physica C **351** (2001) 48.

[Dem03]   K. DEMMLER, M. FALTER, B. SCHLOBACH, W. HÄSSLER, L. SCHULTZ and B. HOLZAPFEL: *Nd_2CuO_4 and $La_2Zr_2O_7$ buffer layers for $YBa_2Cu_3O_{7-x}$ coated conductors by chemical solution deposition* (International workshop on coated conductors for applications CCA, 2003).

[Día98a]   A. DÍAZ, L. MECHIN, P. BERGHUIS and J. E. EVETTS: *Evidence for vortex pinning by dislocations in $YBa_2Cu_3O_{7-x}$ low-angle grain boundaries*. Phys. Rev. Lett. **80** (1998) 3855.

[Día98b]   A. DÍAZ, L. MECHIN, P. BERGHUIS and J. E. EVETTS: *Observations of viscous flux flow in $YBa_2Cu_3O_{7-x}$ low-angle grain boundaries*. Phys. Rev. B **58** (1998) 2960.

[Dim88]   D. DIMOS, P. CHAUDHARI, J. MANNHART and F. K. LEGOUES: *Orientation dependence of grain-boundary critical currents in $YBa_2Cu_3O_{7-x}$ bicrystals*. Phys. Rev. Lett. **61** (1988) 1653.

[Dim90]   D. DIMOS, P. CHAUDHARI and J. MANNHART: *Superconducting transport properties of grain boundaries in $YBa_2Cu_3O_7$ bicrystals*. Phys. Rev. B **41** (1990) 4038.

[Don02]   S. DONET, F. WEISS, J. SENATEUR, P. CHANDONET, A. ABRATIS, A. TEISERSKIS, Z. SALTYTE, D. SELBMANN, J. EICKEMEYER, O. STADEL, G. WAHL, C. JIMENEZ and U. MILLER: *YBCO film on buffered Ni RABiTS substrates by pulsed injection MOCVD*. Physica C **372** (2002) 652.

[Eic01]   J. EICKEMEYER, D. SELBMANN, R. OPITZ, B. DE BOER, B. HOLZAPFEL, L. SCHULTZ and U. MILLER: *Nickel-refractory metal substrate tapes with high cube texture stability*. Supercond. Sci. Technol. **14** (2001) 152.

[Ess67]   U. ESSMANN and H. TRÄUBLE: *The direct observation of individual flux lines in Typ II superconductors*. Phys. Lett. A **24** (1967) 526.

[Eve99]   J. E. EVETTS, M. J. HOGG, B. A. GLOWACKI, N. A. RUTTER and V. N. TSANEVA: *Current percolation and V-I transition in $YBa_2Cu_3O_{7-x}$ bicrystals and granular coated conductors*. Supercond. Sci. Technol. **12** (1999) 1050.

[Eve03]   J. E. EVETTS, A. KURSUMOVIC, R. I. TOMOV, N. R. RUTTER, J. L. DRISCOLL, B. A. GLOWACKI, F. SANDIUMENGE, A. CAVALLARO, A. POMAR, T. PUIG, X. OBRADORS, R. HÜHNE, B. HOLZAPFEL, X. QI and Z. LOCKMAN: *Development of "robust" bufer layer architecture for non-vacuum coated conductor processing* (International workshop on coated conductors for applications CCA, 2003).

[Fal02]   M. FALTER, W. HÄSSLER, B. SCHLOBACH and B. HOLZAPFEL: *Chemical solution deposition of $YBa_2Cu_3O_x$ films by dip coating*. Physica C **372-376** (2002) 46.

[Far90]   D. E. FARRELL, J. P. RICE, D. M. GINSBERG and J. Z. LIU: *Experimental evidence of a dimensional crossover in $YBa_2Cu_3O_{7-\delta}$*. Phys. Rev. Lett. **64** (1990) 1573.

[Fel00]   D. M. FELDMANN, J. L. REEVES, A. A. POLYANSKII, G. KOZLOWSKI, R. R. BIGGERS, R. M. NEKKANTI, I. MAARTENSE, M. TOMSIC, P. BARNES, C. E. OBERLY, T. L. PETERSON, S. E. BABCOCK and D. C. LARBALESTIER: *Influence of nickel substrate grain structure on $YBa_2Cu_3O_{7-x}$ supercurrent connectivity in deformation-textured coated conductors*. Appl. Phys. Lett. **77** (2000) 2906.

[Fer02]   L. FERNÁNDEZ, B. HOLZAPFEL, F. SCHINDLER, B. DE BOER and L. SCHULTZ: *Grain boundary network transport properties of $YBa_2Cu_3O_{7-\delta}$ films on biaxially textured metal substrates*. Physica C **372** (2002) 656.

[Fer03]   L. FERNÁNDEZ, B. HOLZAPFEL, F. SCHINDLER, B. DE BOER, A. AT-TENBERGER, J. HÄNISCH and L. SCHULTZ: *Influence of the grain boundary network on the critical current of YBa$_2$Cu$_3$O$_7$ films grown on biaxially textured metallic substrates.* Phy. Rev. B **67** (2003) 52503.

[Fis89]   M. P. A. FISHER: *Vortex-Glass superconductivity: A possible new phase in bulk high-T$_c$ oxides.* Phys. Rev. Lett. **62** (1989) 1415.

[Fis98]   K. FISCHER, T. FAHR, U. SCHLÄFER, M. SCHUBERT, C. RODIG and H. P. TRINKS: *Technology of Bi,Pb-2223 tape fabrication with Ag alloy sheaths for electric power systems.* Superc. Sci. Technol. **11** (1998) 995.

[Fol99]   S. R. FOLTYN, Q. X. JIA, P. N. ARENDT, L. KINDER, Y. FAN and J. F. SMITH: *Relationship between film thickness and the critical current of YBa$_2$Cu$_3$O$_{7-x}$-coated conductors.* Appl. Phys. Lett. **75** (1999) 3692.

[Fuj03]   K. FUJINO, M. KONISHI, K. MURANAKA, S. HAHAKURA, K. OHMATSU, K. HAYASHI, N. HOBARA, S. HONJO and Y. TAKAHASHI: *Development of RE123 coated conductors by ISD method.* Physica C **392** (2003) 815.

[Gra90]   K. E. GRAY, R. T. KAMPWIRTH and D. E. FARRELL: *Giant torque magnetization anisotropy in Tl$_2$Ba$_2$CaCu$_2$O$_x$.* Phys. Rev. B **41** (1990) 819.

[Gri91]   R. GRIESSEN: *Thermally activated flux motion near the absolute zero.* Physica C **172** (1991) 441.

[Gur93]   A. GUREVICH, A. E. PASHITSKI, H. S. EDELMAN and D. C. LARBALESTIER: *Modelling the current-voltage characteristics of silver-sheathed Bi-Sr-Ca-Cu-O tapes.* Appl. Phys. Lett. **62** (1993) 1688.

[Gur94]   A. GUREVICH and L. D. COOLEY: *Anisotropic flux pinning in a network of planar defects.* Phys. Rev. B **50** (1994) 13563.

[Gur98]   A. GUREVICH and E. A. PASHITSKII: *Current transport through low-angle grain boundaries in high-temperature superconductors.* Phys. Rev. B **57** (1998) 13878.

[Gur02]   A. GUREVICH, M. S. RZCHOWSKI, G. DANIELS, S. PATNAIK, B. M. HINAUS, F. CARILLO, F. TAFURI and D. C. LARBALESTIER: *Flux flow of Abrikosov-Josephson vortices along grain boundaries in high-temperature superconductors.* Phys. Rev. Lett. **88** (2002) 97001.

[Gut01] K. GUTH, H. U. KREBS, H. C. FREYHARDT and C. JOOS: *Modification of transport properties in low-angle grain-boundaries via calcium doping of $YBa_2Cu_3O_{7-x}$ thin films*. Phys. Rev. B **64** (2001) 140508.

[Ham00] G. HAMMERL, A. SCHMEHL, R. R. SCHULZ, B. GOETZ, H. BIELEFELDT, C. W. SCHNEIDER, H. HILGENKAMP and J. MANNHART: *Enhanced supercurrent density in polycristalline $YBa_2Cu_3O_{7-x}$ at 77 K from calcium doping of grain-boundaries*. Nature **407** (2000) 162.

[Hän02] J. HÄNISCH, A. ATTENBERGER, B. HOLZAPFEL and L. SCHULTZ: *Electrical transport properties of $Bi_2Sr_2Ca_2Cu_3O_{10+x}$ thin films (001) tilt grain boundaries*. Phys. Rev. B **65** (2002) 2507.

[Haw91] M. HAWLEY, I. D. RAISTRICK, J. G. BERRY and R. J. HOULTON: *Growth mechanism of sputtered films of $YBa_2Cu_3O_{7-x}$ studied by scanning tunneling microscopy*. Science **251** (1991) 1587.

[Hei89] K. HEINE, J. TENBRINK and M. THÖNER: *High field critical current densities in $Bi_2Sr_2Ca_1Cu_2O_{8+x}/Ag$ wires*. Appl. Phys. Lett. **55** (1989) 2441.

[Hei99] N. F. HEINIG, R. D. REDWING, J. E. NORDMAN and D. C. LABALESTIER: *Strong to weak coupling transition in low misorientation angle thin film $YBa_2Cu_3O_{7-\delta}$ bicrystals*. Phys. Rev. B **60** (1999) 1409.

[Hil96] H. HILGENKAMP, J. MANNHART and B. MAYER: *Implications of $d_{x^2-y^2}$ symmetry and faceting for the transport properties of grain boundaries in high-T_c superconductors*. Phys. Rev. B **53** (1996) 14586.

[Hil99a] H. HILGENKAMP, C. SCHNEIDER, B. GOETZ, R. SCHULZ, A. SCHMEHL, H. BIELEFELDT and J. MANNHART: *Grain boundary critical currents-a new perspective*. Supercond. Sci. Technol. **12** (1999) 1043.

[Hil99b] H. HILGENKAMP, C. SCHNEIDER, R. SCHULZ, B. GOETZ, A. SCHMEHL, H. BIELEFELDT and J. MANNHART: *Modifying electronic properties of interfaces in high-T_c superconductors by doping*. Physica C **326** (1999) 7.

[Hir82] J. P. HIRTH and J. LOTHE: *Theory of dislocations* (Wiley, New York, 1982).

[Hog01] M. J. HOGG, F. KAHLMANN, E. J. TARTE, Z. H. BARBER and J. E. EVETTS: *Vortex channeling and the voltage-characteristics of $YBa_2Cu_3O_7$ low-angle grain-boundaries*. Appl. Phys. Lett. **78** (2001) 1433.

[Hol93]   B. HOLZAPFEL, G. KREISELMEYER, M. KRAUS, S. BOUFFARD, S. KLAUMÜNZER, L. SCHULTZ and G. SAEMANN-ISCHENKO: *Angle-resolved critical transport current density of $YBa_2Cu_3O_{7-\delta}$ thin films and $YBa_2Cu_3O_{7-\delta}$ / $PrBa_2Cu_3O_{7-\delta}$ superlattices containing columnar defects of various orientations*. Phys. Rev. B **48** (1993) 600.

[Hol95]   B. HOLZAPFEL: *Konventionelle und off-axis Laserdeposition von $YBa_2Cu_3O_{7-x}$ Dünnschichten und heteroepitaktischen Multilagen- Präparation und Pinningeigenschaften*. Ph.D. thesis, Friedrich-Alexander Universität Erlangen-Nürnberg (1995).

[Hol00]   B. HOLZAPFEL, D. VEREBELYI, C. CANTONI, M. PARANTHAMAN, B. SALES, R. FEENSTRA, D. CHRISTEN and D. P. NORTON: *Low angle grain boundary transport properties of undoped and doped Y123 thin film bicrystals*. Physica C **341** (2000) 1431.

[Hol01a] T. G. HOLESINGER, S. R. FOLTYN, P. N. ARENDT, Q. JIA, P. C. DOWDEN, R. C. DE PAULA and J. R. GROVES: *A Comparison of buffer layer architectures on continuously processed $YBa_2Cu_3O_{7-x}$ coated conductors based on the IBAD YSZ process*. IEEE Trans. Appl. Superconductivity **11** (2001) 3359.

[Hol01b] B. HOLZAPFEL, L. FERNÁNDEZ, F. SCHINDLER, B. DE BOER, N. REGER, J. EICKEMEYER, P. BERBERICH and W. PRUSSEIT: *Grain boundary network in Y123 coated conductors: formation, properties and simulation*. IEEE Trans. Appl. Superconductivity **11** (2001) 3872.

[Hos03]   S. HOSTE and I. V. DRIESSCHE: *Sol gel deposition of CeO_2 buffer layers and $REBa_2Cu_3O_y$* (International workshop on coated conductors for applications CCA, 2003).

[How89]   R. S. HOWLAND, T. H. GEBALLE, S. S. LADERMAN, A. FISCHER-COLBRIE, M. SCOTT, J. M. TARASCON and P. BARBOUX.: *Determination of dopant site occupancies in Cu-substituted $YBa_2Cu_3O_{7-x}$ by differential anomalous x-ray scattering*. Phys. Rev. B **39** (1989) 9017.

[Hüh01]   R. HÜHNE, C. BEYER, B. HOLZAPFEL, C. G. OERTEL, L. SCHULTZ and W. SKROTZKI: *Formation and destruction of cube texture in MgO films using ion-beam assisted pulsed laser deposition*. J. Appl. Phys. **90** (2001) 1035.

[Ich99]   A. ICHINOSE, C. Y. YANG, D. C. LARBALESTIER, S. E. BABCOCK, A. KIKUCHI, K. TACHIKAWA, and S. AKITA: *Growth conditions and mi-*

crostructure of Y_2O_3 buffer layers on cube-textured Ni. Physica C **324** (1999) 113.

[Iij03]   Y. IIJIMA, K. KAKIMOTO, Y. SUTOH, S. AJIMURA and T. SAITOH: *Preparation of 100 m class Y-123 coated conductors by IBAD and PLD process* (International workshop on coated conductors for applications CCA, 2003).

[Iva91]   Z. G. IVANOV, P. A. NILSSON, D. WINKLER, J. A. ALARCO and T. CLAESON: *Weak links and dc SQUIDS on artificial nonsymmetric grain boundaries in $YBa_2Cu_3O_7$.* Appl. Phys. Lett. **59** (1991) 3030.

[Jia01]   Q. X. JIA, S. R. FOLTYN, P. N. ARENDT and J. F. SMITH: *High-temperature superconducting thick films with enhanced supercurrent carrying capability.* Appl. Phys. Lett. **80** (2001) 1601.

[Jor87]   J. D. JORGENSEN, M. A. BENO, D. G. HINKS, L. SODERHOLM, K. J. VOLIN, R. L. HITTERMAN, J. D. GRACE, I. K. SCHULLER, C. D. SEGRE, K. ZHANG and M. S. KLEEFISCH: *Oxygen ordering and the orthorhombic-to-tetragonal phase transition in $YBa_2Cu_3O_{7-x}$.* Phys. Rev. B **36** (1987) 3608.

[Jos62]   B. D. JOSEPHSON: *Possible new effects in superconductive tunnelling.* Physics Letters **1** (1962) 251.

[Kes90]   P. H. KES, J. AARTS, V. M. VINOKUR and C. J. VAN DER BEEK: *Vortices in high-temperature superconductors.* Phys. Rev. Lett. **64** (1990) 1063.

[Koc89]   R. H. KOCH, V. FOGLIETTI, W. J. GALLAGHER, G. KOREN, A. GUPTA and M. P. A. FISHER: *Experimental evidence for Vortex-Glass superconductivity in Y-Ba-Cu-O.* Appl. Phys. Lett. **63** (1989) 1511.

[Kou97]   K. A. KOUZNETSOV, A. G. SUN, B. CHEN, A. S. KATZ, S. R. BAHCALL, J. CLARKE, R. C. DYNES, D. A. GAJEWSKI, S. H. HAN, M. B. MAPLE, J. GIAPINTZAKIS, J. T. KIM and D. M. GINSBERG: *c-axis Josephson tunneling between $YBa_2Cu_3O_7$ and Pb: direct evidence for mixed order parameter symmetry in a high-T_c superconductor.* Phys. Rev. Lett. **79** (1997) 3050.

[Kra73]   E. KRAMER: *Scaling laws for flux pinning in hard superconductors.* J. Appl. Phys. **44** (1973) 1360.

[Kur03]   A. KURSUMOVIC, R. HÜHNE, R. TOMOV, B. HOLZAPFEL, B. A. GLOWACKI and J. E. EVETTS: *Investigation of the growth and stability of (1 0 0)[0 0 1] NiO films grown by thermal oxidation of textured (1 0 0)[0 0 1]*

Ni tapes for coated conductor applications during oxygen exposure from 700 to 1400 °. Acta Mat. **51** (2003) 3759.

[Lai90]   B. M. LAIRSON, S. K. STREIFFER and J. C. BRAVMAN: *Vortex pinning and twin boundaries in YBa$_2$Cu$_3$O$_{7-\delta}$*. Phys. Rev. B **42** (1990) 10067.

[Leo03]   K. J. LEONARD, A. GOYAL, D. M. KROEGER, J. W. JONES, S. KANG, N. RUTTER, M. PARANTHAMAN, D. F. LEE and B. W. KANG: *Thickness dependence of microstructure and critical current density of YBa$_2$Cu$_3$O$_{7-\delta}$ on rolling assisted biaxially textured substrates*. J. Matter. Res. **18** (2003) 1109.

[Low97]   B. L. LOW, S. Y. XU, C. K. ONG, X. B. WANG and Z. X. SHEN: *Substrate temperature dependence of the texture quality in YBa$_2$Cu$_3$O$_{7-x}$ thin films fabricated by on-axis pulsed-laser ablation*. Supercond. Sci. Technol. **10** (1997) 41.

[Mal90]   M. P. MALEY, J. O. WILLIS, H. LESSURE and M. E. MCHENRY: *Dependence of flux-creep activation energy upon current density in grain-aligned YBa$_2$Cu$_3$O$_{7-x}$*. Phys. Rev. B **42** (1990) 2639.

[Man92]   J. MANNHART, D. ANSELMETTI, J. G. BEDNORZ, A. CATANA, C. GERBER, K. A. MÜLLER and D. G. SCHLOM: *Correlation between J$_c$ and screw dislocation density in sputtered YBa$_2$Cu$_3$O$_{7-\delta}$ films*. Z. Phys. B - Condensed Matter **86** (1992) 177.

[Man99]   J. MANNHART and H. HILGENKAMP: *Interfaces involving complex superconductors*. Physica C **317** (1999) 383.

[Man00a]   J. MANNHART, H. BIELEFELDT, B. GOETZ, H. HILGENKAMP, A. SCHMEHL, C. W. SCHNEIDER and R. R. SCHULZ: *Doping induced enhancement of the critical currents of grain boundaries in high-T$_c$ superconductors*. Physica C **341** (2000) 1393.

[Man00b]   J. MANNHART, H. BIELEFELDT, B. GOETZ, H. HILGENKAMP, A. SCHMEHL, C. W. SCHNEIDER and R. R. SCHULZ: *Grain boundaries in high-T$_c$ superconductors: insights and improvements*. Phil. Mag. B **80** (2000) 827.

[Man01]   J. MANNHART, G. HAMMERL, H. BIELEFELDT, H. HILGENKAMP, S. LEITENMEIER, A. SCHMEHL, C. W. SCHNEIDER, R. SCHULZ, A. GOYAL, B. W. KANG, F. A. LIST, D. K. CHRISTEN and D. M. KROEGER: *Grain boundaries in high-Tc superconductors- data, ideas and*

prospects. Proceedings 10th International Workshop on Critical Currents IWCC 2001 (2001) 27.

[Mar92] J. C. MARTINEZ, S. H. BRONGERSMA, A. KOSHELEV, B. IVLEV, P. H. KES, R. P. GRIESSEN, D. G. DE GROOT, Z. TARNAVSKI and A. A. MENOVSKY: *Magnetic anisotropy of $Bi_2Sr_2CaCu_2O_x$ single crystal*. Phys. Rev. Lett. **69** (1992) 2276.

[Mas03] L. J. MASUR, D. BUDZEK, E. HARLEY, T. KODENKANDATH, X. LI, J. LYNCH, N. NGUYEN, M. RUPICH, U. SCHOOP, J. SCUDIERE, E. SIEGAL, C. THIEME, D. VEREBELYI, W. ZHANG and J. KELLERS: *The status of commercial and developmental HTS wires*. Physica C **392** (2003) 989.

[Mat98] J. E. MATHIS, A. GOYAL, D. F. LEE, F. A. LIST, M. PARANTHAMAN, D. K. CHRISTEN, E. D. SPECHT, D. M. KROEGER and P. M. MARTIN: *Biaxially textured $YBa_2Cu_3O_{7-x}$ conductors on rolling assisted biaxially textured substrates with critical current densities of 2-3 MA/cm^2*. Jpn. J. Appl. Phys. **37** (1998) 1379.

[Mat99] K. MATSUMOTO, S. B. KIM, J. G. WEN, I. HIRABAYESHI, T. WATANABE, N. UNO and M. IKEDA: *Fabrication of in-plane aligned YBCO films on polycrystalline Ni tapes buffered with surface oxidized NiO layers*. IEEE Trans. Appl. Superconductivity **9** (1999) 1539.

[Met01] R. METZGER, M. BAUER, K. NUMSSEN, R. SEMERAD, P. BERBERICH and H. KINDER: *Superconducting tapes using ISD buffer layers produced by evaporation of MgO or reactive evaporation of magnesium*. IEEE Trans. Appl. Superconductivity **11** (2001) 2826.

[Moe93] B. H. MOECKLEY, D. K. LATHROP and R. A. BUHRMAN: *Electromigration study of oxygen disorder and grain-boundary effects in $YBa_2Cu_3O_7$ thin films*. Phys. Rev. B **47** (1993) 400.

[Nab94] T. NABATAME, S. KOIKE, O. HYUN, I. HIRABAYASHI, H. SUHARA and K. NAKAMURA: *Transport superconducting properties of grain boundaries in $TlBa_2Ca_2Cu_3O_x$ thin films*. Appl. Phys. Lett. **65** (1994) 776.

[Nis00] T. NISHIZAKI and N. KOBAYASHI: *Vortex-matter phase diagram in $YBa_2Cu_3O_x$*. Supercond. Sci. Technol. **13** (2000) 1.

[Nor96] D. P. NORTON, A. GOYAL, J. D. BUDAI, D. K. CHRISTEN, D. M. KROEGER, E. D. SPECHT, Q. HE, B. SAFFIAN, M. PARANTHAMAN, C. E. KLABUNDE, D. F. LEE, B. C. SALES and F. A. LIST: *Epitaxial*

YBa$_2$Cu$_3$O$_{7-x}$ on biaxially textured nickel(001): an approach to superconductivity tapes with high critical current density. Science **274** (1996) 755.

[Nor98]   D. P. NORTON, C. PARK, C. PROUTEAU, D. K. CHRISTEN, M. CHISHOLM, J. D. DUBAI, S. J. PENNYCOOK, A. GOYAL, E. Y. SUN, D. F. LEE, D. M. KROEGER, E. SPECHT, M. PARANTHAMAN and N. D. BROWNING: *Epitaxial YBa$_2$Cu$_3$O$_{7-x}$ films on rolled metals for high-temperature superconducting applications.* Material Science and Engineering B **56** (1998) 86.

[Oku01]   H. OKUYUKU, E. CELIK, M. K. RAMAZANOGLU, Y. AKIN, I. H. MUTLU, W. SIGMUND, J. E. CROW and Y. S. HASCICEK: *Textured buffer layers for YBa$_2$Cu$_3$O$_{7-x}$ coated conductors by continuous sol-gel processing.* IEEE Trans. Appl. Superconductivity **11** (2001) 2889.

[Ovc91]   Y. N. OVCHINNIKOV and B. I. IVLEV: *Pinning in layered inhomogeneous superconductors.* Phys. Rev. B **43** (1991) 8024.

[Pal91]   T. T. PALSTRA, B. BATLOGG, L. F. SCHNEEMEYER and J. V. WASZCZAK: *Role of anisotropy in the dissipative behavior of high-temperature superconductors.* Phys. Rev. B **43** (1991) 3756.

[Par96]   J. A. PARELL, D. C. LARBALESTIER, G. N. RILEY, Q. LI, R. D. PARRELLA and M. TEPLITSKY: *Enhancement of the 77 K irreversibility field and critical current density of (Bi,Pb)$_2$Sr$_2$Ca$_2$Cu$_3$O$_x$ tapes by manipulation of the final cooling rate.* Appl. Phys. Lett. **69** (1996) 2915.

[Par99a]   M. PARANTHAMAN, D. F. LEE, R. FEENSTRA, A. GOYAL, D. T. VEREBELYI, D. K. CHRISTEN, E. D. SPECHT, F. A. LIST, P. M. MARTIN and D. M. KROEGER: *Optimization of buffer layers on rolled-Ni subtrates for high current YBa$_2$Cu$_3$O$_{7-x}$ and Tl,Bi-1223 coated conductors using ex-situ precursor approches.* IEEE Trans. Appl. superconductivity **9** (1999) 2268.

[Par99b]   M. PARANTHAMAN, D. F. LEE, E. D. SPECHT, P. M. MARTIN, X. CUI, J. E. MATHIS, R. FEENSTRA, D. K. CHRISTEN and D. M. KROEGER: *Growth of biaxially textured RE$_2$O$_3$ buffer layers on rolled-Ni substrates using reactive evaporation for HTS-coated conductors.* Supercond. Sci. Tecnol. **12** (1999) 319.

[RM91]   J. ROSSAT-MIGNOD, L. P. REGNAULT, C. VETTIER, P. BURLET, J. Y. HENRY and G. LAPERTOT: *Investigation of the spin dynamics in YBa$_2$Cu$_3$O$_{7-\delta}$ by inelastic neutron scattering.* Physica B **169** (1991) 58.

[Roa90a] B. ROAS: *Herstellung und Eigenschaften Laser-aufgedampfter YBa$_2$Cu$_3$O$_{7-x}$ Filme.* Ph.D. thesis, Friedrich-Alexander Universität Erlangen-Nürnberg (1990).

[Roa90b] B. ROAS, L. SCHULTZ and G. SAEMANN-ISCHENKO: *Anisotropy of the critical current density in epitaxial YBa$_2$Cu$_3$O$_x$ films.* Phys. Rev. Lett. **64** (1990) 479.

[Rom01] E. J. ROMANS, A. EULENBURG, C. CARR, A. J. MILLAR, G. B. DON-ALDSON and C. M. PEGRUM: *NdBa$_2$Cu$_3$O$_7$ bicrystal josephson junctions and SQUIDs operating at 77 K.* IEEE Trans. Appl. Superconductivity **11** (2001) 1347.

[Sar94] E. SARNELLI, P. CHAUDHARI, W. Y. LEE and E. ESPOSITO: *Transport properties in Tl-Ba-Ca-Cu-O grain boundaries.* Appl. Phys. Lett. **65** (1994) 362.

[Sar02] V. SARMA, B. DE BOER, N. REGER, J. EICKEMEYER, R. OPITZ and B. HOLZAPFEL: *Ni and Ni-alloy with a very strong cube texture as substrates for high temperature superconducting tapes.* Materials Science Forum **408-412** (2002) 1561.

[Sar03a] V. SARMA, B. DE BOER, J. EICKEMEYER and B. HOLZAPFEL: *On the development of high strength and bi-axially textured Ni-3%W-Ni-10%Cr-1.5%Al composite substrate for coated conductor application.* Scripta Mater. **48** (2003) 1167.

[Sar03b] V. S. SARMA, J. EICKEMEYER, A. SINGH, L. SCHULTZ and B. HOLZAPFEL: *Development of high strength and strongly cube textured Ni-4.5%W / Ni-15for coated conductor application.* Acta Mater. **51** (2003) 4919.

[Sch91] P. SCHMITT, P. KUMMETH, L. SCHULTZ and G. SAEMANN-ISCHENKO: *Two-dimensional behavior and critical current anisotropy in epitaxial Bi$_2$Sr$_2$CaCu$_2$O$_{8+x}$ thin films.* Phys. Rev. Lett. **67** (1991) 267.

[Sch99] A. SCHMEHL, B. GOETZ, R. SCHULZ, C. SCHNEIDER, H. BIELEFELDT, H. HILGENKAMP and J. MANNHART: *Doping-induced enhancement of the critical currents of grain boundaries in YBa$_2$Cu$_3$O$_{7-\delta}$.* Europhys. Lett. **47** (1999) 110.

[Sch00] F. SCHINDLER: *Simulation und Messung kritischer Ströme in Korngrenzennetzwerken biaxial texturierter YBa$_2$Cu$_3$O$_{7-x}$.* Technische Universität Dresden (2000). Diploma thesis.

[Sie02]   M. P. SIEGAL, P. G. CLEM, J. T. DAWLEY, R. J. ONG, M. A. RODRIGUEZ
          and D. L. OVERMYER: *All solution-chemistry approach for $YBa_2Cu_3O_{7-x}$-
          coated conductors*. Appl. Phys. Lett. **80** (2002) 2710.

[Sta98]   T. STAIGER: *Stromtransport in supraleitenden $(Bi,Pb)_2Sr_2Ca_2Cu_3O_x$/Ag-
          Bändern*. Ph.D. thesis, Technische Universität Dresden (1998).

[Ste97]   T. STEIGER, G. FUCHS, P. VERGES, K. FISHER, L. SCHULTZ and
          A. GLADUN: *Critical current in silver-sheathed Bi-2223 tapes*. IEEE Trans.
          Appl. Superconductivity **7** (1997) 1347.

[Tal95]   J. L. TALLON, C. BERNHARD, H. SHAKED, R. L. HITTERMAN and J. D.
          JORGENSEN: *Generic superconducting phase behaviour in high-T_c cuprates:
          T_c variation with the hole concentration in $YBa_2Cu_3O_x$*. Phys. Rev. B **51**
          (1995) 12911.

[Tar88]   J. M. TARASCON, P. BARBOUX, P. F. MICELI, L. H. GREENE, G. W.
          HULL, M. EIBSCHUTZ and S. A. SUNSHINE: *Structural and physical prop-
          erties of the metal (M) substituted $YBa_2Cu_{3-x}M_xO_{7-y}$ perovskite*. Phys. Rev.
          B **37** (1988) 7458.

[Tho02]   J. R. THOMPSON, A. GOYAL, D. K. CHRISTEN and D. M. KROEGER:
          *Ni-Cr textured substrates with reduced ferromagnetism for coated conductor
          applications*. Physica C **370** (2002) 169.

[Tin96]   M. TINKHAM: *Introduction to Superconductivity*. 2 edn. (McGraw-Hill,
          Inc., 1996).

[Tsu94]   C. C. TSUEI, J. R. KIRTLEY, C. C. CHI, L. S. YU-JAHNES, A. GUPTA,
          T. SHAW, J. Z. SUN and M. B. KETCHEN: *Pairing symmetry and flux
          quantization in a tricrystal superconducting ring of $YBa_2Cu_3O_7$*. Phys. Rev.
          Lett. **73** (1994) 593.

[Tsu98]   A. TSUKAMOTO, K. TAKAGI, Y. MORIWAKI, T. SUGANO, S. ADACHI
          and K. TANABE: *High performance $(Hg,Re)Ba_2CaCu_2O_y$ grain boundary
          josephson-junctions and dc superconducting quantum interference devices*.
          Appl. Phys. Lett. **73** (1998) 990.

[USD98]   *At the Frontier of Science*. Tech. rep., U.S. Department of Energy (1998).

[Ver00]   D. T. VEREBELYI, D. K. CHRISTEN, R. FEENSTRA, C. CANTONI,
          A. GOYAL, D. F. LEE, P. N. ARENDT, R. F. DEPAULA, J. R. GROVES
          and C. PROTEAU: *Low angle grain boundary transport in $YBa_2Cu_3O_{7-x}$
          coated conductors*. Appl. Phys. Lett. **76** (2000) 1755.

[Wal96] J. R. WALDRAM: *Superconductivity of metals and cuprates* (Institute of Physics Publishing, Techno House, Redcliffe Way, Bristol, 1996).

[Web03] A. WEBER, G. HAMMERL, A. SCHMEHL, C. SCHNEIDER and J. MANNHART: *Ca-doping-induced enhancement of the critical currents of coated conductors grown by ion-beam-assisted deposition.* Appl. Phys. Lett. **82** (2003) 772.

[Wol93] D. A. WOLLMAN, D. J. V. HARLINGEN, W. C. LEE, D. M. GINSBERG and A. J. LEGGET: *Experimental determination of the superconducting pairing state in YBCO from the phase coherence of YBCO-Pb dc SQUIDs.* Phys. Rev. Lett. **71** (1993) 2134.

[Woo99] S. I. WOODS, A. S. KATZ, T. L. KIRK, M. C. DEANDRADE, M. B. MAPLE and R. C. DYNES: *Investigation of Nd-Ce-Cu-O planar tunnel-Junctions and bicrystals grain boundary junctions.* IEEE Trans. Appl. Superconductivity **9** (1999) 3917.

[Yam93] H. YAMASAKI, K. ENDO, S. KOSAKA, M. UMEDA, S. YOSHIDA and K. KAJIMURA: *Scaling of the flux pinning force in epitaxial $Bi_2Sr_2Ca_2Cu_3O_x$ thin films.* Phys. Rev. Lett. **70** (1993) 3331.

[Zel89] E. ZELDOV, N. M. AMER, G. KOREN, A. GUPTA, R. J. GAMBINO and M. W. MCELFRESH: *Optical and electrical enhancement of flux creep in $YBa_2Cu_3O_{7-\delta}$ epitaxial films.* Phys. Rev. Lett. **62** (1989) 3093.

[Zel90] E. ZELDOV, N. M. AMER, G. KOREN, A. GUPTA and M. W. MCELFRESH: *Flux creep characteristics in high-temperature superconductors.* Appl. Phys. Lett. **56** (1990) 680.

Acknowledgements

Publications

1. B. HOLZAPFEL, L. FERNÁNDEZ, M.A. ARRANZ, N. REGER , B. DE BOER, J. EICKEMEYER, L. SCHULTZ: *Heteroepitaxial growth of oxide buffer layers by pulsed laser deposition on biaxially oriented Ni and Ni alloy tapes*, Proceedings of 4th EUCAS 1999. Institute of Physics Conference Series, 167/1, 419-422 (2000).

2. B. DE BOER, J. EICKEMEYER, N. REGER, L. FERNÁNDEZ, J. RICHTER, B. HOLZAPFEL, L. SCHULTZ, W. PRUSSEIT, P. BERBERICH: *Cube textured nickel alloy tapes as substrates for buffer and $YBa_2Cu_3O_{7-\delta}$ coated conductors*, Acta Mater. **49** (2001), 1421.

3. B. DE BOER, N. REGER, L. FERNÁNDEZ, J. EICKEMEYER, P. BERBERICH, W. PRUSSEIT, B. HOLZAPFEL, L. SCHULTZ: *Biaxially textured Ni-alloy tapes as substrate for buffer and YBCO film growth*, IEEE Trans. Appl. Superconductivity **11** (2001), 3477.

4. B. HOLZAPFEL, L. FERNÁNDEZ, F. SCHINDLER, B. DE BOER, N. REGER , J. EICKEMEYER, P. BERBERICH, W. PRUSSEIT: *Grain boundary networks in Y123 coated conductors: formation, properties and simulation*, IEEE Trans. Appl. Superconductivity **11** (2001), 3872.

5. B. DE BOER, N. REGER, L. FERNÁNDEZ, J. EICKEMEYER, B. HOLZAPFEL, L. SCHULTZ, W. PRUSSEIT, P. BERBERICH: *Biaxially textured Ni-alloy tapes as substrate for buffer and YBCO film growth*, Physica C **351** (2001), 38.

6. L. FERNÁNDEZ, B. HOLZAPFEL, F. SCHINDLER, B. DE BOER, L. SCHULTZ: *Grain boundary network transport properties of biaxially textured metallic substrates*, Physica C **372** (2002), 656.

7. L. FERNÁNDEZ, B. HOLZAPFEL, F. SCHINDLER, B. DE BOER, A. ATTENBERGER, J. HÄNISCH, L. SCHULTZ: *Influence of the grain boundary network on*

the critical current of YBa$_2$Cu$_3$O$_{7-\delta}$ films on RABiTS substrates, Phys. Rev. B **67** (2003), 52503.

8. A. PALAU, T. PUIG, X. OBRADORS, A. USOSKIN, H.C. FREYHARDT, L. FERNÁNDEZ, B. HOLZAPFEL: *Inductive analysis on magnetic granularity effects in YBCO-IBAD and RABiTS coated conductors*, IEEE Trans. Appl. Superconductivity **13** (2003), 2599.

9. C. CAI, B. HOLZAPFEL, J. HÄNISCH, L. FERNÁNDEZ, L. SCHULTZ: *High critical current density and its field dependence in mixed rare earth (Gd, Eu, Nd)Ba$_2$Cu$_3$O$_{7-\delta}$ thin films*, accepted for publication in Appl. Phys. Lett.

10. A. PALAU, T. PUIG, X. OBRADORS, E. PARDO, C. NAVAU, A. SÁNCHEZ, A. USOSKIN, H.C. FREYHARDT, L. FERNÁNDEZ, B. HOLZAPFEL, R. FEENSTRA: *Simultaneous inductive determination of grain and inter-grain critical current densities of YBa$_2$Cu$_3$O$_{7-\delta}$ coated conductors*, accepted for publication in Appl. Phys. Lett.

Erklärung

Hiermit versichere ich, daß ich die vorliegende Arbeit ohne unzulässige Hilfe Dritter und ohne Benutzung anderer als der angegebenen Hilfsmittel angefertigt habe; die aus fremden Quellen direkt oder indirekt übernommenen Gedanken sind als solche kenntlich gemacht. Die Arbeit wurde bisher weder im Inland noch im Ausland in gleicher oder ähnlicher Form einer anderen Prüfungsbehörde vorgelegt.

Die Dissertation wurde am IFW Dresden unter der wissenschaftlichen Betreuung von Herrn Prof. Dr. L. Schultz angefertigt.

Dresden, 4. Dezember 2003   Laura Isabel Fernández Gómez-Recuero